COOLING OF ELECTRONIC SYSTEM:

FROM ELECTRONIC CHIPS TO DATA CENTERS

by

JINGRU ZHANG

A Dissertation submitted to the

Graduate School-New Brunswick

Rutgers, The State University of New Jersey

in partial fulfillment of the requirements

for the degree of

Doctor of Philosophy

Graduate Program in Mechanical and Aerospace Engineering

written under the direction of

Professor Yogesh Jaluria

and approved by

_____

_____

_____

_____

New Brunswick, New Jersey

January, 2012

ABSTRACT OF THE DISSERTATION

Cooling of Electronic System: From Electronic Chips to Data Centers

By JINGRU ZHANG

Dissertation Director:
Professor Yogesh Jaluria

In this work, the physical problems associated with heat removal of electronic systems at different scales were studied. Various electronic cooling system designs and specific cooling techniques to improve performance were discussed. Optimization procedures and suggestion for better design was proposed.

This study consisted of two main parts. The first part was from the microscale aspect, where single phase liquid cooling in different multi-microchannel heat sink configurations was studied experimentally and numerically. The effects of flow separation and flow redirection on the microchannel heat sink cooling performance were investigated. A multi-objective optimization problem was formulated based on both experimental and numerical results and was solved numerically with and without

physical constraint. The Pareto frontiers were presented to provide quantitative guidance for the process of design and optimization.

The second part of the study involved cooling of larger dimension electronic systems, which focused on the cooling of data centers. The temperature and flow distribution in a data center for both steady state and transient state were studied. The energy consumption of the cooling system with different running conditions was analyzed. Based on the investigation of the thermal response of the data center cooling system to sudden power increase caused by dynamic load migration, pre-cooling concept with dynamic load migration was investigated to generate a robust, reliable, more efficient and energy-conservative design.

ACKNOWLEDGEMENT

I would like to express my gratitude to my advisor, Dr. Jaluria, for his constant guidance and encouragement throughout my doctorate study. Dr. Jaluria has a profound impact on my path to seek the professional career and I am deeply grateful for his invaluable advice, insightful vision and great patience.

I wish to express my gratitude to Professor Shan, Professor Guo and Professor Bianchini for their constructive suggestions and their time and efforts in reviewing the proposal and dissertation.

My sincere gratitude goes to John Petrowski, who provided generous support as a design specialist during my experimental set up. Thanks to Dr. Shaurya Prakash for his help and guidance with the fabrication process. I wish to thank the people at Rutgers Micro Electronic Fabrication Lab for their assistance on this project. Especially, Jun Tan and Lei Lin provided invaluable help in the fabrication process. Chieh-Jen Ku and Ziqing Duan shared their experience and skills in using the equipment. I would also like to thank my lab mates for their company and help. Thanks to Po Ting Lin, Jiandong Meng and Kien Le for their help and ideas.

Mere words can express my gratitude to my family. My parents, Wenjun Kang and Liansheng Zhang, have given me wonderful support and I appreciate all that they've done

for me. My brother Jinglei always cheers me up and encourages me. I want to thank my dear boyfriend, Zheng Wang, for walking through the journey together with me.

TABLE OF CONTENTS

LIST OF FIGURES

LIST OF TABLES

NOMENCLATURE

A	$Area,\ m^2$
C_p	Specific heat capacity, $\mathrm{J/K}g \cdot ℃$
$\boldsymbol{C}$	Covariance tensor
COP	coefficient of performance
D_H	Hydraulic Diameter, m
e_i	i^{th} Normal basis
F	Parametric model using Kriging
F^s	Vector of responses
f	Fanning friction factor
f_{app}	Apparent fanning friction factor
F_p	Fractional open area of the perforated tile
g	Body force, m/s^2
g_i	i^{th} Inequality constraint
G	Turbulence kinetic energy
h	Heat transfer coefficient
H	Height, m
k	Thermal conductivity, $W/(m \cdot K)$
k_p	Coverage factor
K	Flow resistance factor
M	Number of sampling points

N	Microchannel numbers
Nu	Nusselt number
P	Wetted perimeter of the cross section, m
ΔP	Pressure drop, Pa
Pr	Prantl number
q	Heat flux, w/m^2
Q	Flow rate, (m^3/s)
r_h	Hydraulic radius, m
Ra	Surface roughness parameter
Ra_x	Rayleigh number
$\boldsymbol{V}$	Velocity vector
w	Weighting coefficient in multi-objective functions
$\boldsymbol{w}$	Vector of coefficients in Kriging model
Re	Reynolds number
T	Temperature
u	Velocity, m/s
U_p	Uncertainty
W	Width, m
x^+	Dimensionless axial distance

Greek Symbols

α	Aspect ratio

β	Thermal expansion coefficient
Δ	Difference
ε	Turbulence dissipation rate
κ	Turbulence kinetic energy
ν	Kinematic viscosity, m^2/s
θ	Thermal resistance
τ_s	Shear stress, Pa
τ	Time constant
ρ	Density, kg/m^3
Superscript	
$\sim$	Average
Subscript	
cal	Caloric
i	Interface
in	Inlet
out	Outlet
m	Mean value
s	Spreading
tot	Total
vh	Viscous heating

Chapter 1 Introduction

1.1 Motivation

Electronic devices, reaching into every aspect of modern living, are becoming more and more sophisticated and highly compact. This trend leads to increasingly high heat density generated by electric current. The heat flux from the surface of an electronic chip increased from approximately 10^2 to 10^7 watts per unit meter square. For large scale electronic systems, high heat flux is also becoming a concern due to the rising power density. In order to avoid the malfunctions of electronics and to ensure the reliability of the electronic systems, substantial research work has been done to explore more effective cooling techniques to keep up with the development pace of new electronic equipment and large electronic systems.

The main purpose of the current study is to investigate thermal performance of electronic cooling system at different scales. Micro-scale electronic cooling was studied through experiments and numerical simulation. Different configurations of microchannel heat sinks were investigated. Optimized solutions for single-phase liquid flow in microchannel heat sinks were found. Large-scale electronic cooling was investigated to address the thermal challenges in data centers with varying heat load at both steady and transient states.

1.2 Literature review on microchannel heat sink

A heat sink consisting of multiple microchannels with liquid flow is believed to be a promising cooling method for high heat dissipation electronic chips due to the relatively high heat capacity and heat removal efficiency offered by liquids in contrast to air (Tuckermann and Pease 1981). Previous research works on microchannel fluid flow and heat transfer have involved both computational and experimental methods (Kandlikar 2003, Wei and Joshi 2004, Zhang et al 2005, Steinke et al 2006). It is noticed that, due to the fabrication process, the silicon base of microchannels usually has non-circular and mostly rectangular cross sections.

The majority of the references cited in literature use the Navier-Stokes equation to analyze the microscale fluid system numerically. Since convective heat transfer in rectangular channels is critical in macro-scale design, early studies on micro-scale rectangular channels also focused on convective heat transfer (Tso and Mahulikar 1998, Harms et al 1999). However, unlike the macro-scale channels, the ratio of fin and channel width as well as the ratio of the silicon substrate thickness and the channel depth is not negligible in micro-scale systems. Therefore, researchers started to realize that conduction plays an importance role in the overall heat transfer (Marabzan 2004, Sharath 2006). Combined conduction and convection, or conjugate heat transfer, needs to be considered for numerical analysis for micro-scale cases. Fedorov and Viskanta (2000) used classical theory to analyze conjugate heat transfer in a three dimensional

microchannel heat sink. Husian and Kim (2007) solved the Navier-stokes and the energy equations to study the conjugate heat transfer and fluid flow in microchannels, and also used the multiobjective method to optimize the ratio of channel width to depth. Li and Peterson (2004) provided a detailed temperature and heat flux distribution using a simplified three dimensional conjugate heat transfer model (2D fluid flow and 3D heat transfer). The effect of temperature dependence has also been studied (Li et al 2007). Model with varying thermal properties generated results closer to experiments than model with constant thermal properties.

The fabrication process of microchannels introduces local variations in channel properties due to the surface roughness or differences in surface chemical composition. Modeling these changes continues to be a challenge (Papautsky et al 1999, Mala et al 1997). Hence, experimental investigation is important in understanding the heat transfer and fluid dynamics in microchannels. Tuckerman and Pease (1981) were the first to set up experiments on a microchannel heat sink, which provided the precedent for many experimental studies. Steinke and Kandlikar et al (2006) presented details of an experimental facility that was capable of accurately investigating the performance of a microchannel heat sink with different geometries by including the experimental uncertainty. Wei and Joshi (2004) designed a double-layered microchannel heat sink, which reduced half of the pressure drop under constant flow rate. They also studied sidewall velocity profiles in microchannels using micro-PIV. It was a significant improvement in term of reducing the pumping power, but the thermal resistance was not very sensitive to the number of layers. Therefore, the thermal performance was not

improved significantly. Zhang et al. (2005) applied actual electronic packages (flip chip ball grid array packages) as heat source on the bottom of the heat sink instead of simulated heaters in their study. The junction temperature was measured and the experimental results matched the analytical prediction quite well.

Other than single-phase liquid flow, there were also substantial studies focusing on boiling flow in mirochannels. It is more complex experimentally and numerically to capture the phase change. Haritchian and Garimella (2008) performed an experiment on two-phase heat transfer in microchannel heat sinks for high heat fluxes. Zhang et al (2002) recorded the pressure and wall temperature distribution during the phase change. Even though it is important to report and visualize the boiling flow in microchannel, applying two phase flow for electronic cooling may not be necessary if liquid cooling is effective.

All experiments till date have mostly explored ways to improve the thermal performance of the straight rectangular microchannel heat sink by optimizing the aspect ratio of the straight rectangular microchannels and its fins, in order to increase the convective heat transfer by the coolant. However, to the best of our knowledge, little work was done on the single-phase liquid multi-microchannel heat sinks with bends and branches. Xiong (2007) and Wang (2009) studied the flow behavior in the U-shaped and serpentine microchannels, but the heat transfer characteristics were not included.

The design optimization of microchannels is another important aspect in the study of micro-cooling systems. Husain and Kim (2009) solved the Navier-Stokes and the energy equations to study the conjugate heat transfer and fluid flow in microchannels. They used the multi-objective method to optimize the ratio of channel width to depth. Even though there were substantial studies on the design optimization of the thermal system (Lin 2010), most of the optimization studies for microchannel electronic cooling were based on the experimental results, and therefore were limited by the number of samples and the experimental data range.

In the current study, different configurations were tested through experiments: straight channels, U-shaped channels, Y-shaped channels and serpentine channels. The objective of this study is to investigate the heat transfer characteristics of multi-microchannel heat sinks. The simulation results from the conjugate heat transfer model that considered both conduction and convection appeared to match the experimental data fairly well. The numerical models were then used to conduct a parametric study, based on which an optimization problem was formulated and investigated.

1.3 Literature review on data center thermal management systems

1.3.1 Introduction

Data centers are the foundation of many IT related operations for companies of different industries all over the world. A data center holds computer servers, telecommunications

equipment, data storage systems and many other devices. It is common for a large data center to house more than thousands of server racks with 20~40 servers per each rack. The server chips, which may contain several millions of transistors, will generate a significant amount of heat. The increase of the surface heat flux of electronic chips consequently leads to a high heat density in data centers. Overheating can cause malfunction of servers, which may cost thousands or millions of dollars per minute downtime.

The energy consumed in a data center includes cooling, uninterrupted power supply losses, computer loads and lighting. It was reported that the HVAC system (including chiller and pump) of a typical data center takes up to 54% of the total energy consumption (Tschudi et al 2003). At the same time, the amount of cooling air used in most data centers is 2.5 times more than the required amount (Karki et al 2003). Google has invested substantial resources in reducing their data center power use, and reports a Power Usage Effectiveness (PUE) in the 1.1~1.35 range (Abtes et al 2011). Most data centers use the under-floor plenum below a raised floor to supply cold air to the room. The cold air is delivered from the computer room air conditioner (CRAC) units into the plenum, from where it is introduced into the data center via perforated tiles. By placing the perforated tiles in front of each server rack, it is possible to supply high speed cold air to each rack. The cold air is then distributed to each server by the fan. The advantage of this design is that the solid floor tiles are removable and can be replaced by the perforated tiles. Hence, if the server racks (heat source) layout changed, the perforated tile location can be changed accordingly. This design can meet the needs for most of the data centers.

If the power load is increased, the extra heat dissipated can be removed with an increasing flow rate or with a lower inflow temperature.

Even though the existing design of the under floor plenum with the perforated tiles has the cooling capacity of the current heat load, the cooling system has to meet the needs of the next generation's electronics due to the rapid development of semiconductor industry. Ten percent of the equipment in a data center is replaced each month (International Technology Roadmap for Semiconductors 2008). Energy consumption becomes a bigger concern with the existing cooling system design and the increasing cooling demands. A large potential of cost and energy saving has been realized and the concept of "green data center" has been proposed.

1.3.2 CFD/HT modeling of air cooled data centers

Computation Fluid Dynamics/Heat Transfer modeling is the most practical scientific approach to predict the airflow and temperature distribution in the data center, since it provides comprehensive information to the study of HVAC system efficiency. The thermal management of data centers has only been carefully investigated for the past decade, due to the lack of powerful computing solutions to a large turbulence model. More CFD tools are accessible now to the study of the fluid dynamics and heat transfer inside of a data center.

Throughout the data center industry, the study of energy efficiency has become one of the research priorities (Patterson 2008, Greenberg et al 2006). Based on the assumption of uniform pressure distribution above the raised floor, Karki, Radmehr and Patankar (2003) applied a CFD model to simulate the velocity and flow rate of a real-life data center. The calculated results showed a good agreement with their measured data. Schmidt (2004) presented measured data of airflow rates for a number of different floor layouts for raised-floor data center, where some of the experimental cases were picked out and simulated by a CFD model which showed a good agreement. Schmidt et al (2008) pointed out that the numerical simulation was over estimating the hot and cold spot of the real data center, which may be caused by the simplification to the model especially the simplified representation of the server racks.

1.3.3 Study of transient state

Electronic cooling problems have always been considered as steady-state conditions. However, the maximum heat load usually appears at the start or the shutdown instance of a single electronic chip. For data centers, the transient state is also important since the maximum heat load may rise for certain time period. For instance, the internet takes more traffic after 5pm when people get off work, and it causes the servers to suddenly run from idle state to full load state. The heat dissipated from a server may increase from 150W to 300W correspondingly. The temperature of the equipment and server room starts to increase dramatically. The response time of the HVAC system becomes critical in this case. The transient-state study of electronic cooling process is lacking due to the

complexity of simulating combined convection, radiation and interface conditions. The current study addresses the transient state to better represent the real-world data center conditions and obtain the response time of the HVAC system.

1.4 Dissertation Outline

Chapter 1 explains the importance of cooling for electronics in both micro-scale and large scale systems. For electronic chip cooling, the single-phase liquid-flow microchannel heat sinks are introduced. Conventional scale turbulence model is introduced for data center cooling system. Some previous works are reviewed briefly and the objectives of the study are stated.

Chapter 2 describes the experimental configuration. The microchannel heat sink device design and fabrication process are introduced. The experimental setup, the equipment calibration and the uncertainty analysis are presented.

Chapter 3 presents the experimental results. Both steady state and transient time response results are included. The thermal performance and fluidic performance of heat sinks with different configurations are compared and discussed.

Chapter 4 presents the numerical model setup and validation. The assumptions of the numerical studies are reviewed. The numerical predictions, including different parameters and their influence on the heat sink performance are investigated in detail.

Chapter 5 formulates an optimization problem based on the parametric modeling results with the numerical models developed in chapter 4. A multi-objective optimization problem is solved with the Pareto frontier presented and discussed.

Chapter 6 deals with the thermal management for data centers. The management strategy of the thermal system to respond effectively to a sudden load increase and avoid performance degradation is discussed. Meanwhile, the energy consumption and cost reduction is investigated with the state of the art data center cooling systems.

Chapter 7 presents the conclusions of this study. Different design systems are summarized with suggestions. Possible future interests and suggestions are listed for the study of multi-scale electronic cooling.

Chapter 2 Microchannel Heat Sink Fabrication and Experimental Setup

2.1 Microchannel heat sink fabrication

Fabrication and packaging process is the first and also a very important step for the experimental setup. There are several materials that can be used as for the microchannel heat sink fabrication including diamond, iron, silicon, steel, stainless steel, and aluminum. Single crystal silicon is being employed in modern fabrication because of its well-established electronic properties and its excellent mechanical properties. Many microfabrication technologies have been developed using single-crystal silicon for its high precision, high strength and high reliability. Table 2.1 presents a list of silicon's mechanical characteristics (Peterson 1982).

Table 2.1. Silicon mechanical characteristics.

Yield Strength (10^{10} yne/cm^2)	Knoop Hardness (kg/mm^2)	Young's Modulus (10^{12} yne/cm^2)	Density (gr/cm^3)	Thermal Conductivity (W/cm ^{o}C)	Thermal Expansion (10^{-6}/^{o}C)
7.0	850	1.9	2.3	1.57	2.33

For this study, 4" standard silicon wafer was chosen for the fabrication process. The thickness of a 4" wafer is 550μm, and it is usually determined by the silicon mechanical strength.

Two different methods were used to create the microchannels: wet etching and dry etching. The advantages and disadvantages of both methods are well-known. The most important ones for micromachining are as follows: Wet etching is usually isotropic, which can have a selectivity that depends on crystallographic direction, and can be very selective over masking and underlying layers. Plasma etching (dry etching) can be vertically anisotropic, allowing the patterning of narrow lines. Hence many high aspect ratio MEMs devices are made by dry etching. Both methods were used in the experiment. Hence both dry etching and wet etching will be introduced in this chapter.

2.1.1 Wet etching

Wet etching is relatively economical and the chemical mixtures are easier to prepare. In this work, 30% potassium hydroxide solution (KOH) was used as an etchant to etch 0.085~0.115 Ω-cm p-type (110) oriented silicon wafers from University Wafer. The fabrication and packaging process is illustrated in Figure 2.1 as a process flow diagram.

As shown in Figure 2.1, bare silicon in (a) was cleaned by RCA-1 solution (Water: 27% ammonium hydroxide: 30% hydrogen peroxide=4:1:1) to remove the organic contamination, followed by a HF dip immediately to remove native oxide on the silicon in order to reduce undercutting of the nitride mask (b). The 790 Unaxis PECVD (Plasma Enhanced Chemical Vapor Deposition) system reacted gases in a RF (Radio Frequency) induced plasma to deposit a 2000 Å silicon dioxide (SiO_2) and a 2500 Å silicon nitride (Si_3N_4). The system uses SiH_4 (200 m^3/min), NH_3 (47m^3/min) and N^2 (900 m^3/min)

For the SiO_2 deposition. The corresponding operating temperature, pressure and RF are 300°C, 900 mTorr, and 19W, respectively. The deposition rate is 1000 Å every three minutes. For the Si_3N_4 deposition, the available gases are SiH_4 ($160 m^3/min$) and N_2O ($720\, m^3/min$). The operating temperature, pressure and RF are 250°C, 900 mTorr, and 25W, respectively. The Si_3N_4 deposition rate is 100 Å/min. Buffered oxide etch 7:1 was used to open window of silicon nitride (d) after conventional Ultraviolet (UV) photolithography defines the microchannel pattern on the photo resist (c). The silicon wafer was then dipped into AZ400T solution (e) for half an hour to remove the rest of the photo resist before it dissolved in KOH solution (f). A magnetic stirrer was used to agitate the KOH solution to prevent the etch rate variation from the top to the bottom. 10%~15% isopropanol was added to KOH solution to improve the etch uniformity. A PDMS layer is bonded on top the silicon microchannels after treating with oxygen plasma at 200 W for 15 sec at room temperature (h). Openings were punched in the PDMS for fluid connections. Figure 2.2 shows the SEM of the fabricated microchannel. KOH etching is orientation dependent and this anisotropic etching scheme allows tailoring of sidewall profiles. However, Microchannel fabricated on (110) oriented silicon wafer cannot be scribed by diamond pens as the second crystal cleavage plane is not perpendicular to the primary cut, but has a 70.5º angle.

There are two ways to separate these samples. First, the samples on a silicon wafer can be separated along its self-cleavage direction. The disadvantage of this method is that the surface area of the heat sink will be changed. The other is to create pre-etched grid lines and etch in KOH solution to ensure the device can be separated out safely along those

grid lines [Dwivedi et al 2000]. The overall heat sink dimensions are better controlled this way. The latter method is adopted in this study.

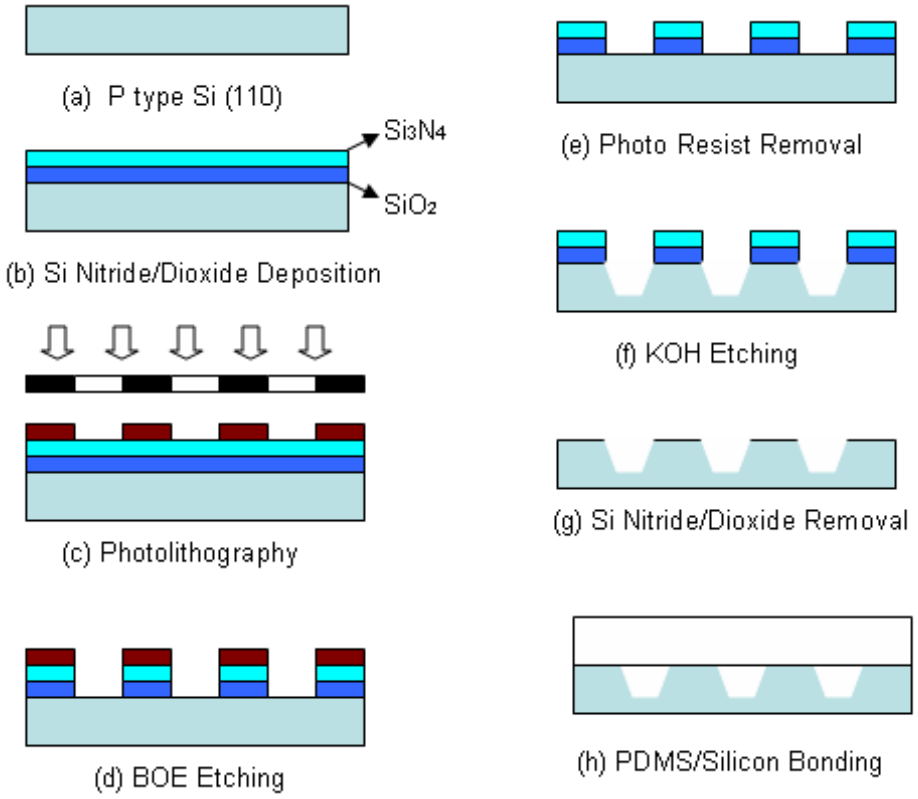

Figure 2.1. Fabrication and packaging process of microchannel heat sinks (Wet Etching).

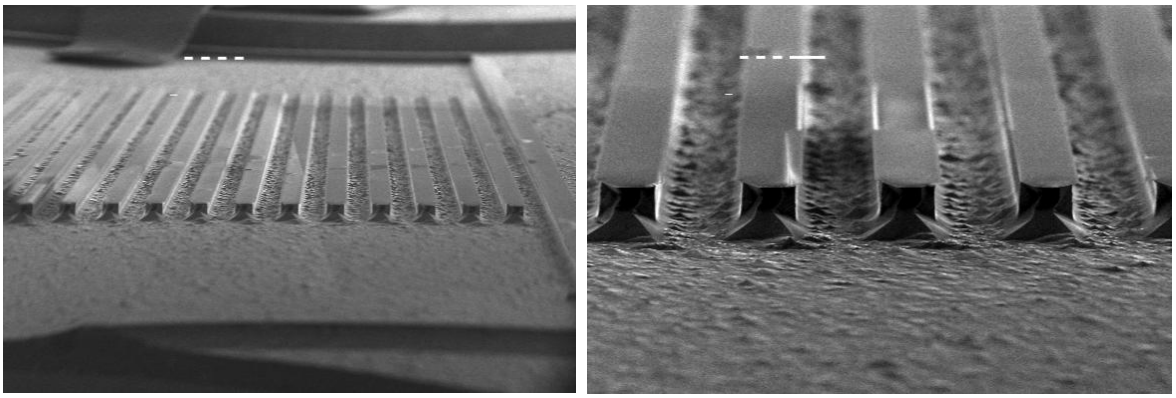

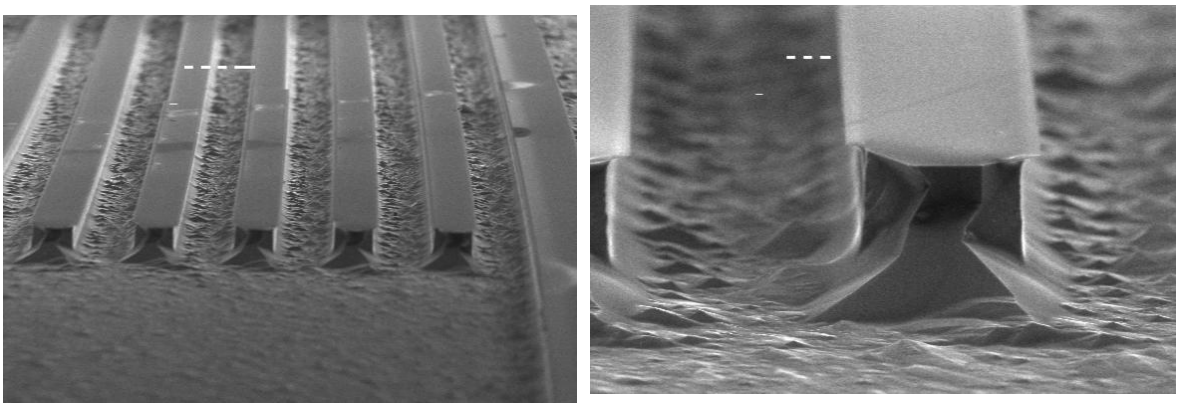

Figure 2.2. SEM micrograph of microchannel after KOH etching.

Wet etching provides a relatively economical method to fabricate microchannel heat sinks when plasma etching equipment is not available. The down side of the wet etching process is the challenge in controlling the undercutting (figure 2.2) and sidewall profile, which tends to be more controllable with dry etching. Moreover, Plasma etching is also more efficient.

2.1.2 Plasma etching

Plasma etching was also used in the experiment to fabricate complicated structures. The wafer preparation for dry etching is easier since it includes less steps compare with wet etching. The cleaning process is the same, then followed by photolithography process (Figure 2.3). AZ1518 were used as mask to protect fins from etching. The SAMCO International RIE800iPB is used for dry etching process. It is a state of the art inductively coupled plasma etcher. The entire 4” silicon wafer were etched in the etcher and got a depth of 175 microns.

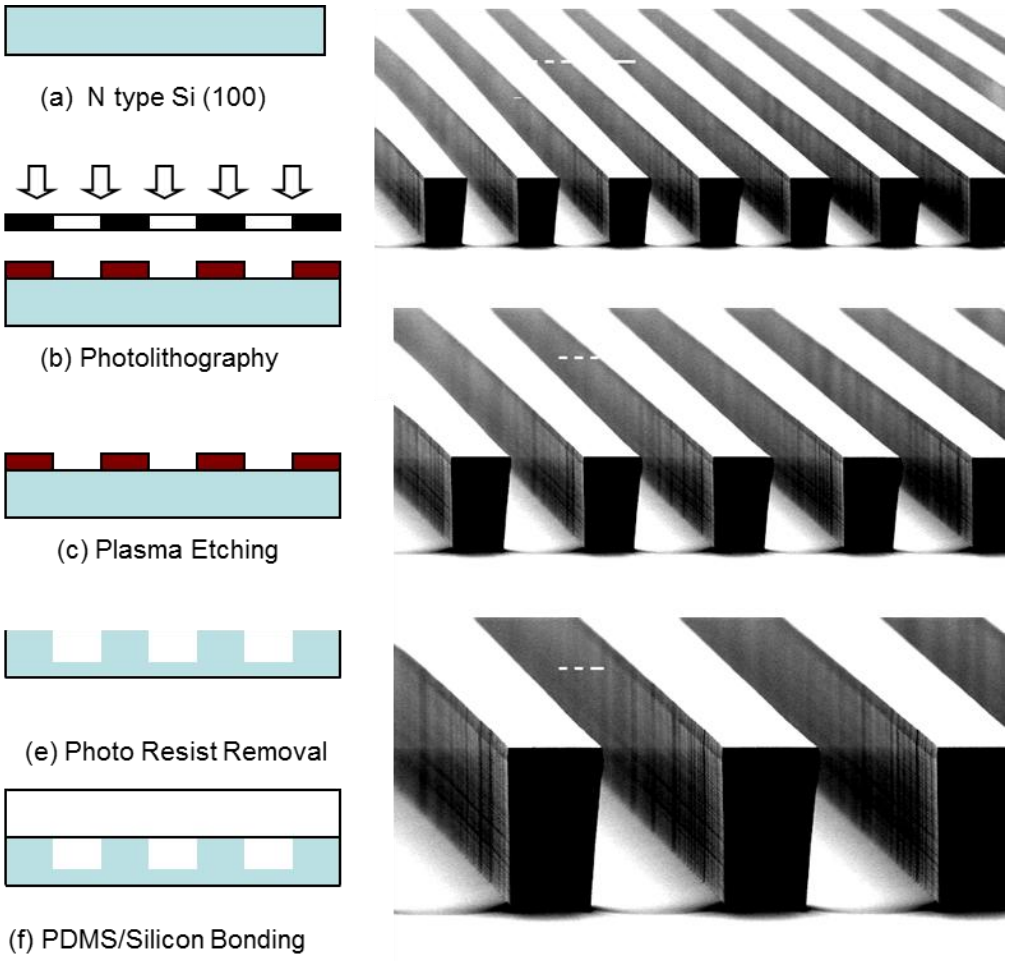

Figure 2.3. Fabrication and packaging process of microchannel heat sinks (Plasma Etching).

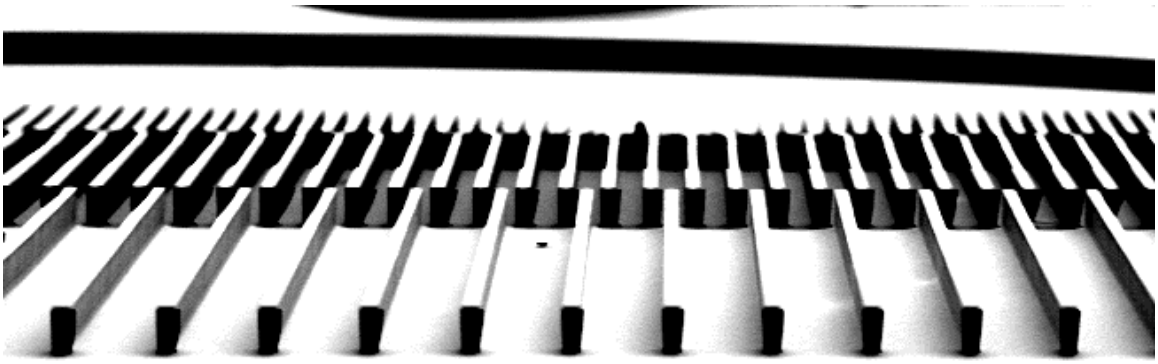

Multichannel heat sink with bifurcation

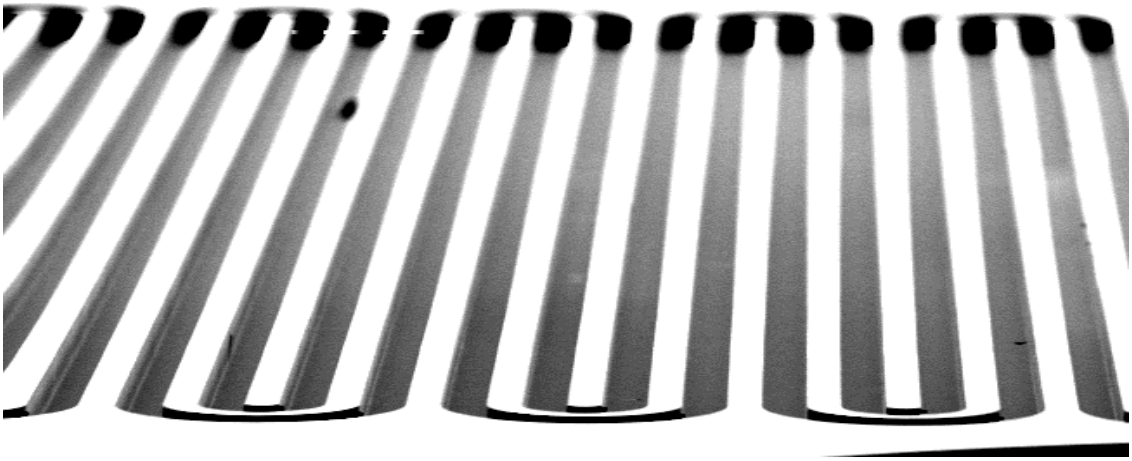

Multichannel heat sink with counter flow

Figure 2.4. SEM micrograph of microchannel heat sink with plasma etching.

2.2 Experimental setup

2.2.1 Experimental facility

For experiments, a commercial miniature Kapton heater from Minco was attached using a high conductive epoxy underneath the microchannel heat sink to simulate the heat released by an electronic chip. The heat flux provided by the heater was controlled via regulating electrical current and voltage of a DC power supply. 4 T-type thermocouples from Omega (Model number: 5TC-TT-T-36-36) were attached on the heater to measure

the temperature variation. 2 T-type fine tip transition joint thermocouples from Omega (model number: TJFT72) were used to measure the temperature at the inlet and outlet of the heat sink.

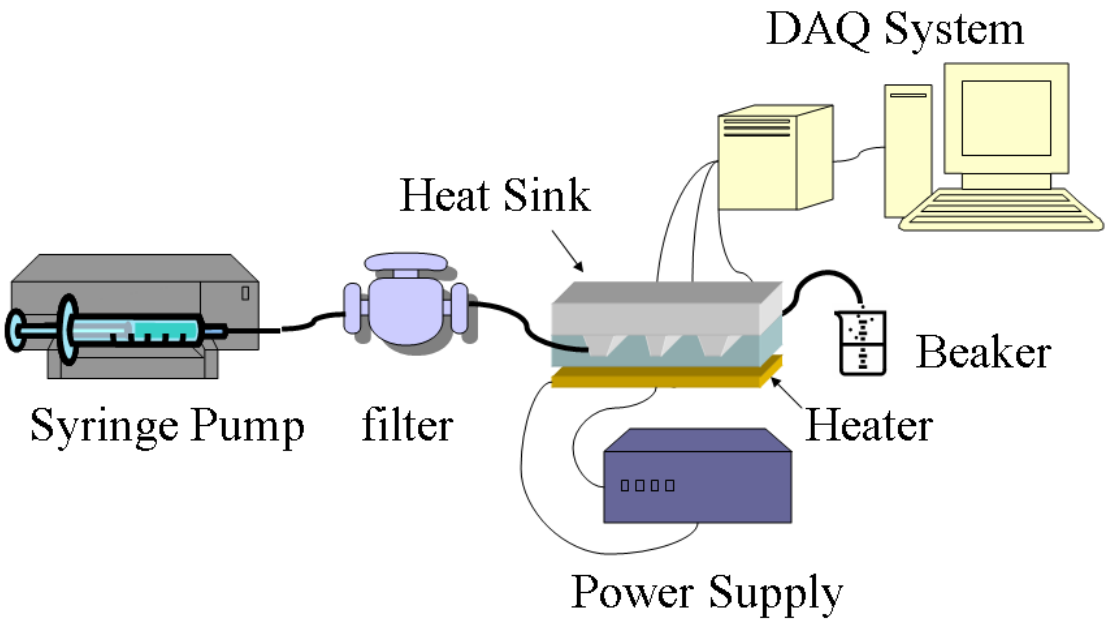

(a) Flow loop

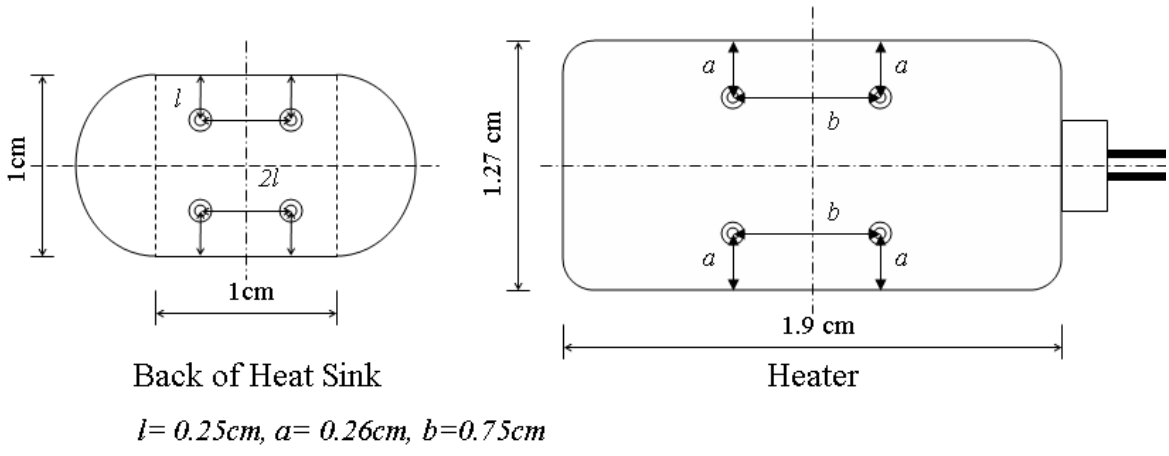

(b) Sketch of thermocouple locations

Figure 2.5. Schematic drawing of the experimental setup.

All the temperature data were collected by the data acquisition system including SCXI system, which consists of SCXI-1000 chassis, SCXI-1100 multiplexer module and the SCXI 1300 terminal block. The SCXI system is used to connect the measurement devices to PCI-6040E DAQ card from National Instrument. A pressure transducer from ASHCROFT (model number: KITMO215F2100) was installed at the inlet of the heat sink to measure the pressure drop. The pressure transducer is then connected to BNC2120 to send data to the computer. The DAQ software is LabVIEW.

Distilled water was used as the coolant due to its large heat capacity (4186 J/kg·K, one of the best among liquid). As showed in figure 2.5, the PHD 2000 Infuse/Withdraw syringe pump from Harvard Apparatus was used to drive the flow. The programmable aspects of the syringe pump also allow the usage of the pump as a flow meter and a valve since specific flow rates can be dialed in for continuous measurements. A filter with 1 micrometer mesh element was used after the syringe to remove any residual impurities suspended in the cooling water.

2.2.2 Calibration and data collection

All the thermocouples were carefully calibrated in a water bath by using a 6-points calibration method. Since the coolant liquid is water, the operating range for the experiments was expected from 0˚C to 100˚C. All the calibration data were recorded and a piecewise linear curve fit was formed. The thermocouples show ±0.5˚C of each other

when measuring a known temperature after calibration was performed, which means that the thermocouples may have an accuracy of ±0.5˚C.

All of the multi-microchannel heat sinks have the same $1cm^2$ surface area (inlet and outflow reservoirs are not included). The syringe pump was turned on before the DC power supply and we waited to let the system run for a while to ensure open bubble-free channels with no leakage in the test system. Then we turned on the power supply, and started recording data.

Several different heat sink configurations were designed and fabricated. The photo masks with different channel configuration patterns can be found in the appendix A. The experimental results with the facility introduced above will be presented and discussed in chapter 3.

Chapter 3 Experimental Results for Microchannel Heat Sinks

This chapter will present the experimental results obtained with the experimental set up introduced in the previous chapter. The dimensionless terms used in this study will be introduced first. Then the experimental measurements uncertainties will be evaluated. The experimental results with different geometry configurations will be presented and discussed.

3.1 Dimensionless parameter

3.1.1 Hydraulic parameters

There are several commonly used dimensionless parameters in fluid dynamics and heat transfer to describe the pressure drop and heat transfer characteristics, which allowed researchers study and compare the results from different literatures more efficient and easier. Definitions of dimensionless parameters used in this paper are as follows (Shah and London, 1978):

a) Reynolds number Re

$$\mathrm{Re} = \frac{uD_h}{\nu} \tag{3.1}$$

where the hydraulic diameter is defined as: $D_h = 4A/P$.

b) Fanning friction factor *f*:

Fanning friction factor is defined as the ratio of wall shear stress τ to the flow kinetic energy per unit volume $\rho u_m^2/2$:

$$f_x = \frac{\tau_x}{\rho u_m^2 / 2} \tag{3.2}$$

The equation above represents the local fanning friction factor. The mean (flow length average) fanning friction factor in the hydrodynamic entrance region is defined as:

$$f_m = \frac{1}{x}\int_0^x f_x dx = \frac{\tau_m}{\rho u_m^2 / 2} \tag{3.3}$$

For the purpose of engineering application, for constant density and constant velocity profile, the pressure drop for the singly connected channel with constant cross section area can be presented by the apparent fanning friction factor:

$$\Delta P^* = \frac{\Delta P}{\rho u_m^2 / 2} = f_{app}\frac{x}{r_h} \tag{3.4}$$

f_{app} is calculated based on the total pressure drop from x=0 to x. Both the skin friction and the momentum rate change are taken into account in the hydrodynamic entrance region. ΔP^* is also used in this study to represent the pressure drop in chapter 4. For a fully developed flow in a channel with channel length L, the equation becomes:

$$\frac{\Delta P}{\rho u_m^2 / 2} = f\frac{L}{r_h} \tag{3.5}$$

For fully developed laminar flow in rectangular channel, the fRe number is a function of the aspect ratio:

$$f\,\mathrm{Re} = 24*(1-1.3553\alpha+1.9467\alpha^2-1.7012\alpha^3+0.9564\alpha^4-0.2537\alpha^5) \qquad (3.6)$$

c) Dimensionless axial distance x^+

The dimensionless axial distance in the flow direction is defined as:

$$x^+ = x / D_h \,\mathrm{Re} \qquad (3.7)$$

The dimensionless axial distance corresponding to hydrodynamic developed region is smaller than 0.1 for rectangular channels. The hydrodynamic entrance length becomes longer as the channel aspect ratio increases (Wiginton and Dalton, 1970).

3.1.2 Heat transfer dimensionless terms

a) The fluid bulk mean temperature T_m is defined as:

$$T_m = \frac{1}{A_c u_m} \oint_A utdA_c \qquad (3.8)$$

b) The heat transfer coefficient h

The most operationally convenient parameter to describe the heat transfer rate is heat transfer coefficient *h*.

The average heat transfer coefficient is defined as:

$$h = \frac{1}{x}\int_0^x \frac{q_x^{"}}{(t_w - t_m)} dx \qquad (3.9)$$

For linear problems, h is independent of the temperature difference.

c) The Nusselt number

Nusselt number is defined as the ratio of convective conductance to the pure molecular thermal conductance:

$$Nu_m = \frac{h_m}{k / D_h} \qquad (3.10)$$

Shah and London (1978) derived the Nusselt number for specified axial wall heat flux boundary condition:

$$Nu = 8.235(1 - 2.0421\alpha + 3.0853\alpha^2 - 2.4765\alpha^3 + 1.0578\alpha^4 - 0.1861\alpha^5) \qquad (3.11)$$

This approximation shows $\pm 0.03\%$ accuracy compare with the experiment results.

3.2 Experimental Uncertainty

The experimental data are incomplete unless we report its uncertainty in the results, which should include all components of standard uncertainty. In this study, we applied guidelines for evaluating and expressing the uncertainty from NIST Technical Note 1297 (1994 Edition). The combined standard uncertainty of the measurement result y,

designated by $u_c(y)$ and taken to represent the estimated standard deviation of the results, is the positive square root of the estimated variance $u^2_c(y)$ obtained from:

$$u_c^2(y) = \sum_{i=1}^{N} \left(\frac{\partial f}{\partial x_i}\right)^2 u^2(x_i) + 2\sum_{i=1}^{N-1} \sum_{j=i+1}^{N} \frac{\partial f}{\partial x_i} \frac{\partial f}{\partial x_j} u(x_i, x_j) \tag{3.12}$$

This propagation of uncertainty is used to evaluate uncertainty of a result which depends on several variables, each with its own uncertainty.

An expanded uncertainty is defined as

$$U_p = k_p u_c(y) \tag{3.13}$$

Where k_p is a coverage factor. Here, k_p=2 defines an interval having a level of confidence of approximately 95 percent. The measurement Y estimated by y is commonly written as:

$$Y = y \pm U_p \tag{3.14}$$

For example, the hydraulic diameter is defined as:

$$D_h = \frac{4W_c H_c}{2(W_c + H_c)} \tag{3.15}$$

The uncertainty of D_h is defined as:

$$\frac{U_{D_h}}{D_h} = \sqrt{\left(\frac{U_a}{a}\right)^2 + \left(\frac{U_a}{a+d}\right)^2 + \left(\frac{U_d}{d}\right)^2 + \left(\frac{U_d}{a+d}\right)^2} \tag{3.16}$$

3.3 Experimental Results:

3.3.1Thermal performance

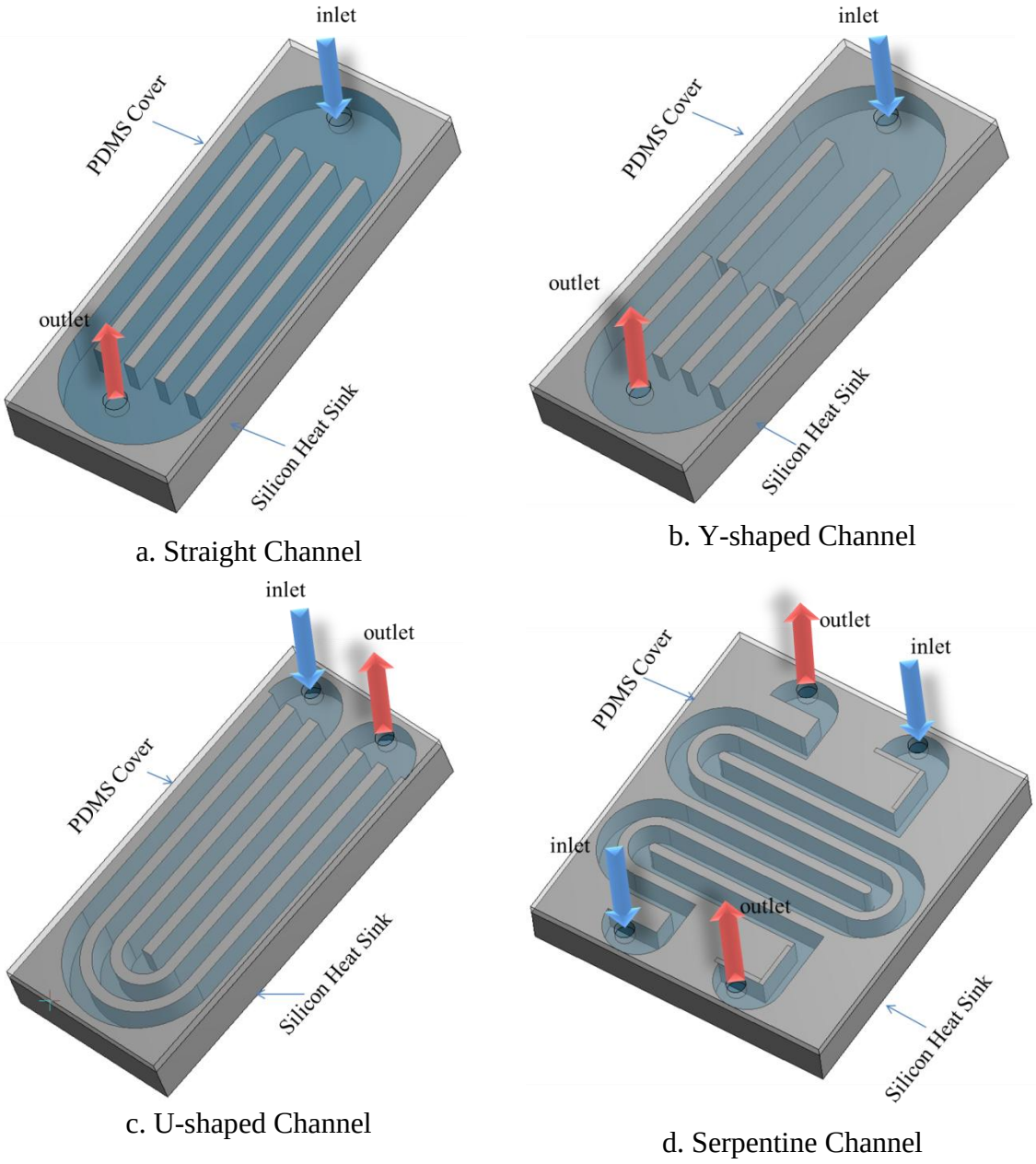

Figure 3.1. Schematic of different microchannel heat sink configurations.

As mentioned in the previous chapter, there are several different heat sinks fabricated with various configurations. Four major ones are shown in figure 3.1. In the experiment, the heater was attached on the bottom of the heat sink. The distilled water at room temperature will be pumped into the microchannel heat sink, takes away the heat, and exit from the outlet to a beaker.

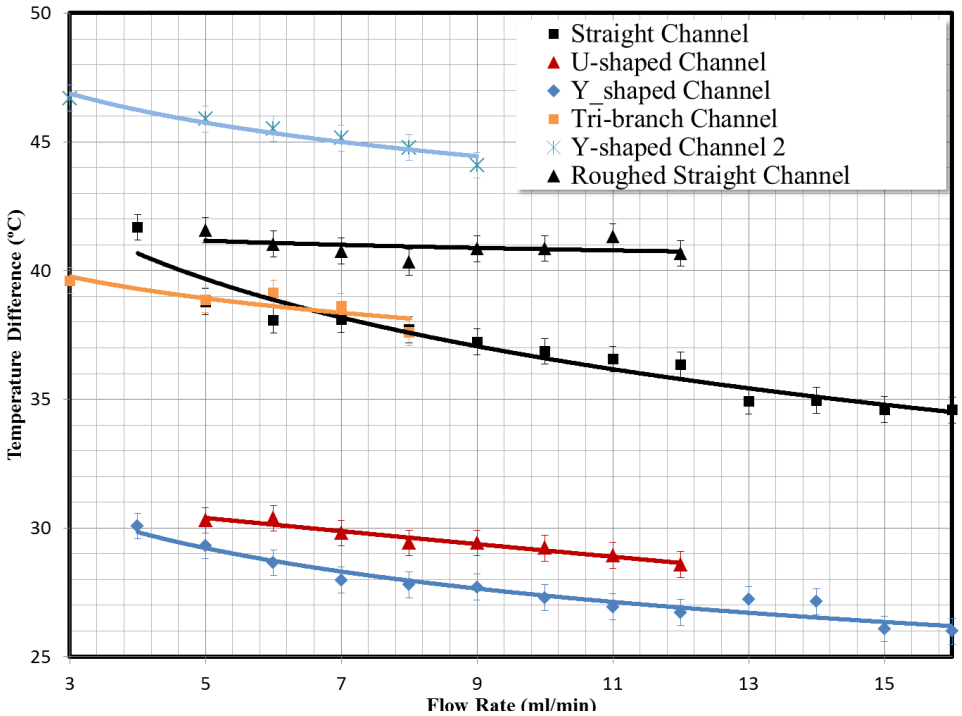

Figure 3.2. Temperature difference vs. flow rate for difference heat sinks.

Four thermocouples were attached on top of the heater to record the temperature data. The heater temperature was calculated based on the average readings from the four thermocouples. The temperature difference between the inlet coolant and heater are shown in figure 3.2. All the heat sinks devices presented in this figure were fabricated on the same silicon wafer (except the straight channel with high Ra number) using plasma etching. Hence, the channel heights are the same for all the cases. In general, the

temperature difference is decreaseing as the flow rate increases for difference heat sinks as expected.

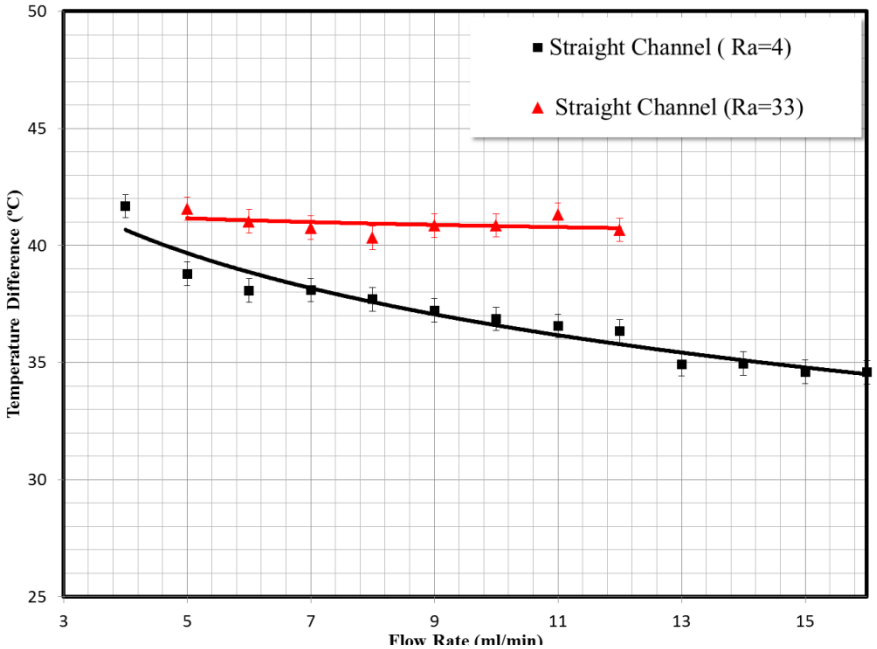

Figure 3.3. Temperature difference vs. flow rate for straight channel.

Figure 3.3 shows the temperature difference for the straight channel with different surface roughness. The surface roughness parameter Ra is the arithmetical mean roughtness obtained with a surface profilometer with randomly sampled channel area along the flow direction. The straight channel heat sink pictures with different Ra numbers taken by SEM are shown in figure 3.4. Compare with a smooth-wall flow(Ra=4), the channle with high Ra number (Ra=33) has negative effect on removing heat. The red curve shown in figure 3.3 is flat, showing that increasing the flow rate can not change the thermal performance when the Ra number is high. This results suggest that it is important to control the channel surface finishing during the fabrication process, and reduce the

bottom and side walls rougthness will help improve the thermal performance of the deivce.

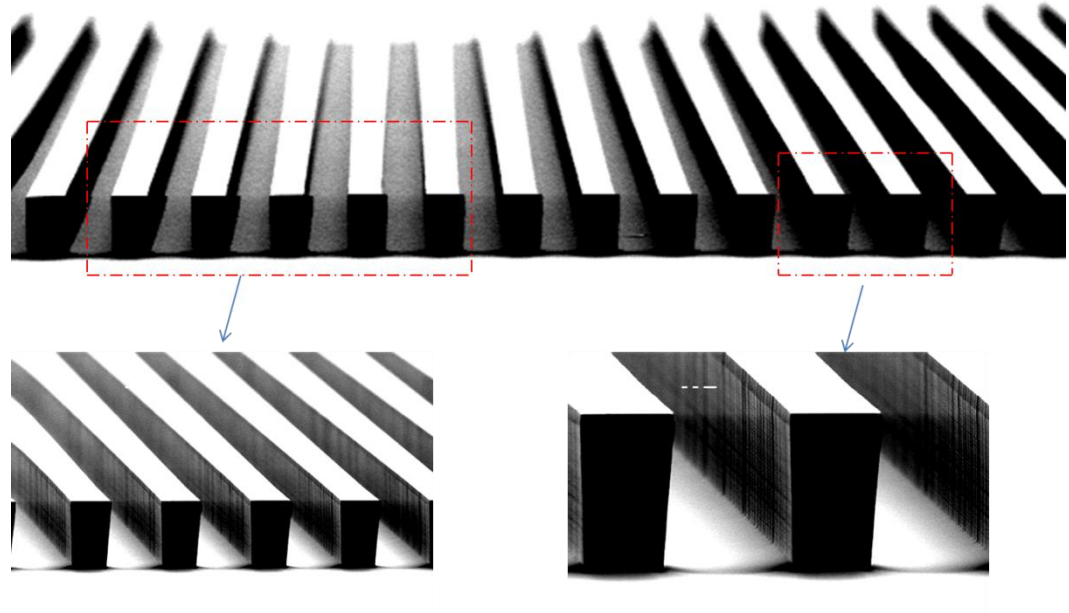

(a) Ra=4

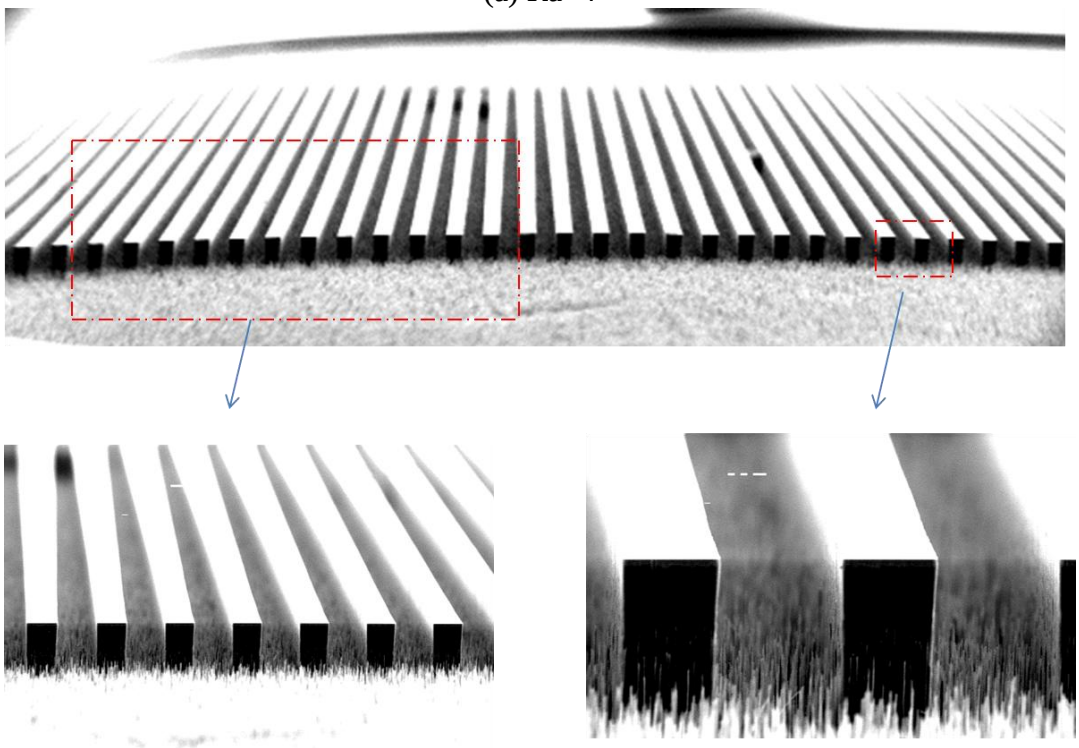

(b) Ra=33

Figure 3.4. SEM micrograph of straight channels with different surface roughness.

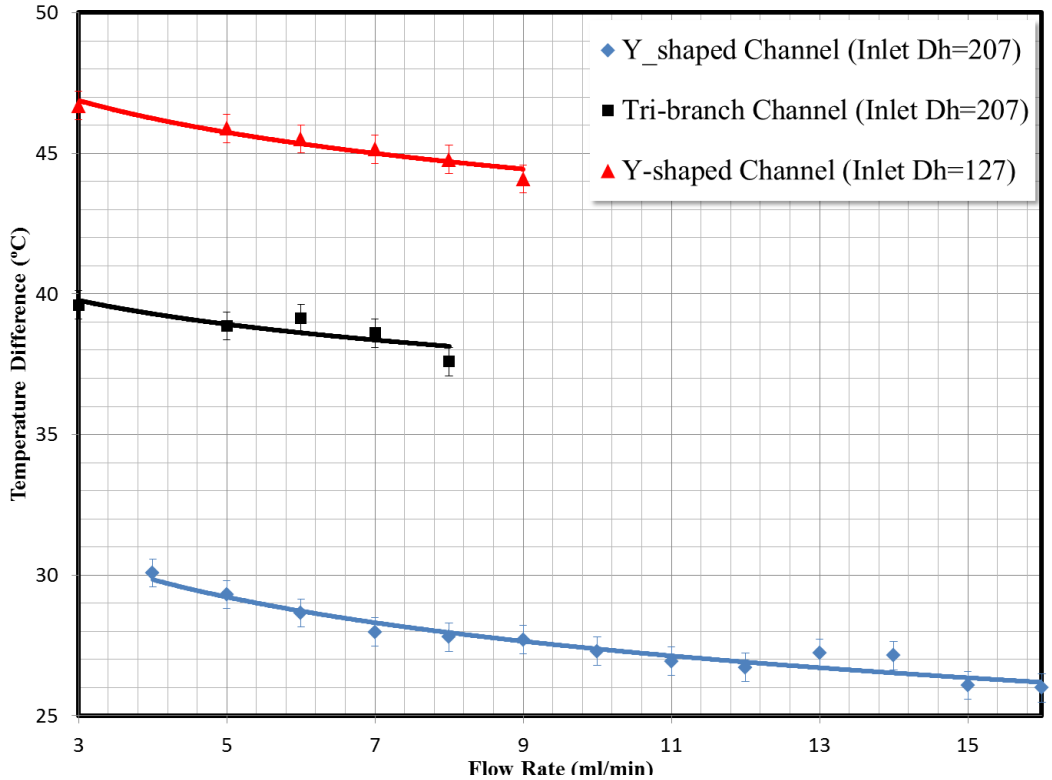

Figure 3.5. Temperature difference vs. flow rate for Y-shaped channel.

Figure 3.5 shows the temperature difference for different channels with branches. The blue diamond marker and the red triangle marker represent heat sink with two branches (the Y-shaped channel shown in figure3.1 (b)). The first one (blue curve) has an inlet channel width of 250 μm, then one channel splits into two channels of width 100 μm. The second one (red curve) has an inlet channel width of 100 μm, and then it reduces to 40 μm. Another heat sink shown as black rectangle markers in the figure has three branches. The channel width is first reduced from 250 μm to 100 μm, and then becomes 40 μm as it goes to the exit. Y-shaped channel with a larger hydraulic diameter shows the best cooling effect among the three. The temperature difference becomes larger as the channel size shrinks. This might be caused by the poor convection happened

at the corners, as the flow is trapped at the corners when separating to narrow channels branches.

The temperature difference for the U-shaped channel is shown in figure 3.6. The temperaeture difference for straight channel is also plotted as a reference. The U-shaped channel shows a significant better cooling effect compare with the straight channel within current experimental range. The 180º bend of the U-shaped channel will result a better flow mixing as well as axial heat conduction enhancement, which contribute to low heater tempreature.

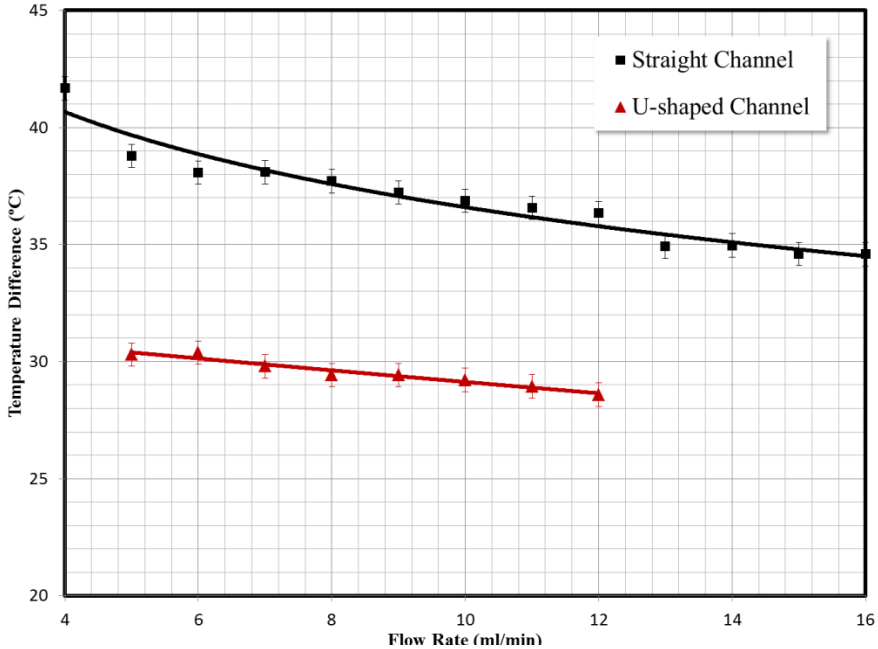

Figure 3.6. Temperature difference vs. flow rate for U-shaped channel.

The total thermal resistance will be used to evaluate the thermal performance of the liquid cooled microchannel heat sinks. The modified total thermal resistance is defined as:

$$\theta_{tot} = \frac{\Delta T A_{ht}}{q} \tag{3.17}$$

The total thermal resistances Vs Reynolds number for different configurations is shown in figure 3.7 and figure 3.8.The thermal resistance becomes smaller as the Reynolds number increases. But the decreasing rate of the thermal resistance gets slower as the Re increases. At the laminar flow region, the thermal performance of the heat sink will reach certain value with a fixed geometry, and it cannot be further improved by simply increasing the flow rate. The configurations that have lower thermal resistance among all the tested devices are the U-shaped channel, Y-shaped channel (with larger hydraulic diameter) and the straight channel.

The total thermal resistance of the system is composed of five components (Tuckerman, 1984),

$$\theta_{tot} = \theta_s + \theta_b + \theta_{cal} + \theta_i + \theta_c \tag{3.18}$$

Each term will be explained in the following section.

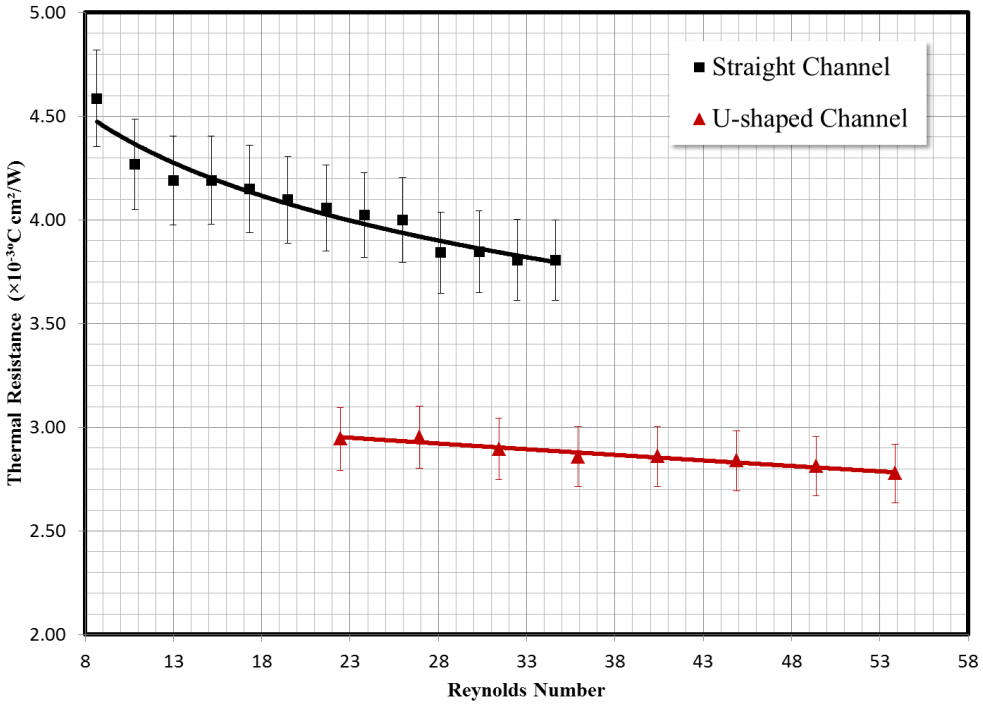

Figure 3.7 Total thermal resitance vs. Reynold number for U-shaped channel

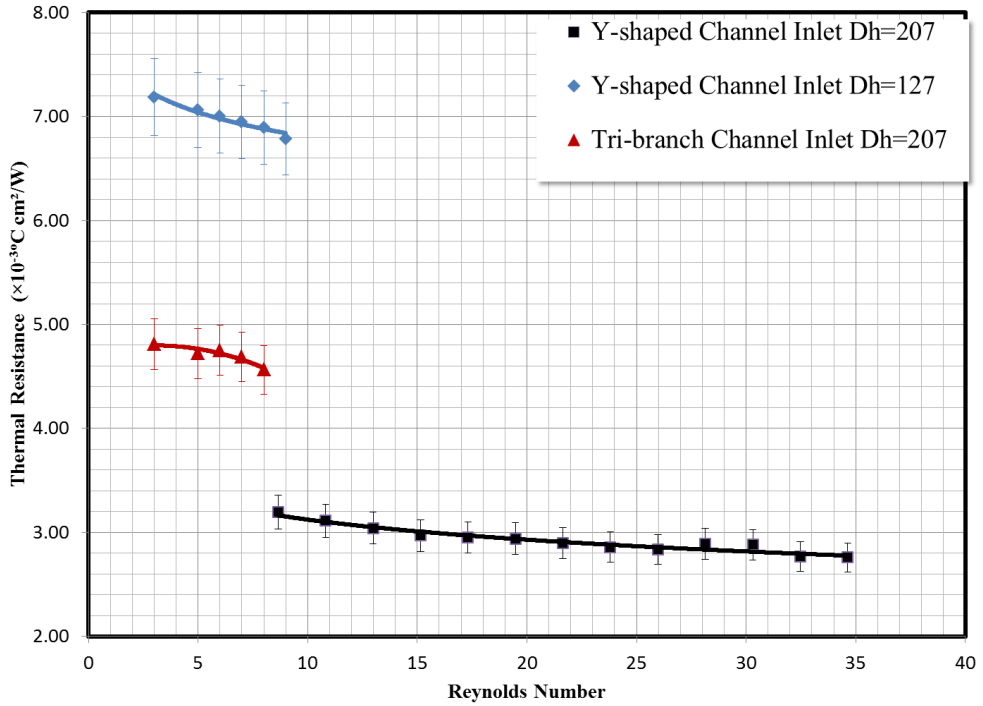

Figure 3.8. Total thermal resitance vs. Reynold number for Y-shaped channel.

The thermal spreading resistance θ_s is the thermal resistance from the individual heat generating devices. In the real electronic cooling application, it is due to thermal spreading of the discrete heat source such as the integrated circuit feature or gate. In our application, it is heating stripe in the miniature heater. For a square heat source, the thermal spreading resistance is calculated as(Tuckerman, 1984):

$$\theta_s = 0.56 A_{ht} / k_h L_j \tag{3.19}$$

For straight channel in our study, the total heat transfer area is $2.52\ cm^2$, and the lead wire length is 77.42cm, with a thermal conductivity of 35.3 W/mK. This leads to θ_s value of $0.052\ ℃cm^2/W$. The temperature rise due to the thermal spreading should decrease as the level of the circuit integration increases. Therefore, this value will be even smaller as the heat flux increases.

The second component θ_b is due to heat conduction through the semiconductor substrate, which is calculated as:

$$\theta_b = \frac{t_s A_{ht}}{k_s A} \tag{3.20}$$

where t_s is the semiconductor substrate thickness, and A is the substrate area. For our experiment, the thickness of the heater is $120\mu m$. θ_b according to equation (3.20) is $0.0002\ ℃cm^2/W$. It is a fairly small number. Furthermore, the substrate thickness for the electronic chip is getting thinner and thinner, which will lead to an even smaller θ_b.

The third component θ_{cal} is the caloric thermal resistance due to the heating of the fluid as it absorbs energy passing through the heat sink. It is calculated as:

$$\theta_b = \frac{1}{\rho C_p Q} \tag{3.21}$$

The higher flow rate, the lower θ_{cal} will be. For example, for 10 ml/min of water, the caloric thermal resistance will be 0.004ºC/Wm, which is very small.

The fourth component is the thermal resistance associated with the IC/heat sink interface θ_i, which is calculated as:

$$\theta_i = \frac{t_i}{k_i A} \tag{3.22}$$

where t_i is the thickness of the interface material, and k_i is the thermal conductivity of the interface material. This term is also called contact resistance in this study. If the microchannel heat sink and the heater are in full contact, this term is zero. In this experiment, the microchannel heat sink is not in full contact with the heater because of the attached thermocouples. It also depends on the flatness of heater surface. The diameter of the thermocouple is 0.13mm, which means that the gap between the heater and the heat sink is at least 0.13mm. Other than the contact region thickness, the interface material will also have a great influence on θ_i. For example, the straight channel heat sink with high conductivity paste will lead to contact resistance as high as 0.002℃cm^2/W, which is 45% of the total thermal resistance. Hence, it is very important to reduce the

contact resistance for high heat flux applications. Note that this term can be eliminated entirely by integrating the heat sink on the heat generating circuits.

The last component is the convective thermal resistance θ_c between the heat sink and coolant. It also includes the thermal resistance of heat conduction in the fin. This is the primary thermal resistance in electronic cooling application and the most difficult one to minimize.

3.3.2 Fluid performance

Some of the microchannel heat sinks show a better thermal performance compare with others. One of the trade-offs is the added pressure drop. Hence, it is important to know the pressure drop for the cooling system. Figure 3.9 and 3.10 show the pressure drop for different microchannel heat sinks in the experiment.

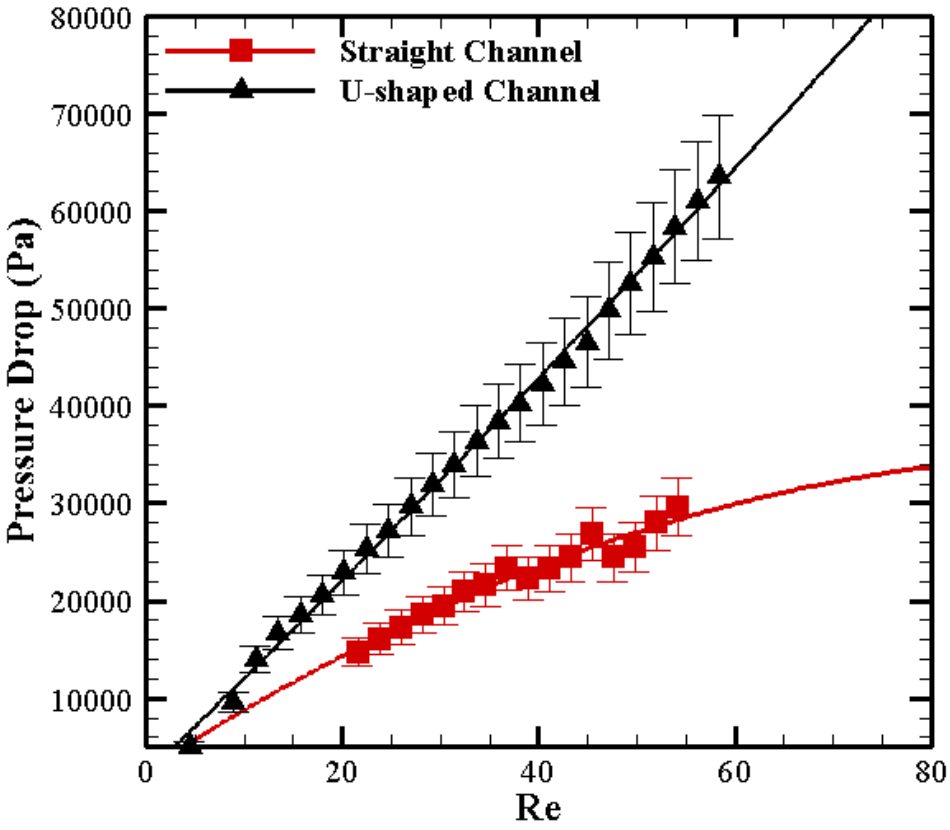

Figure 3.9. Pressure drop vs. Reynolds number for U-shaped channel.

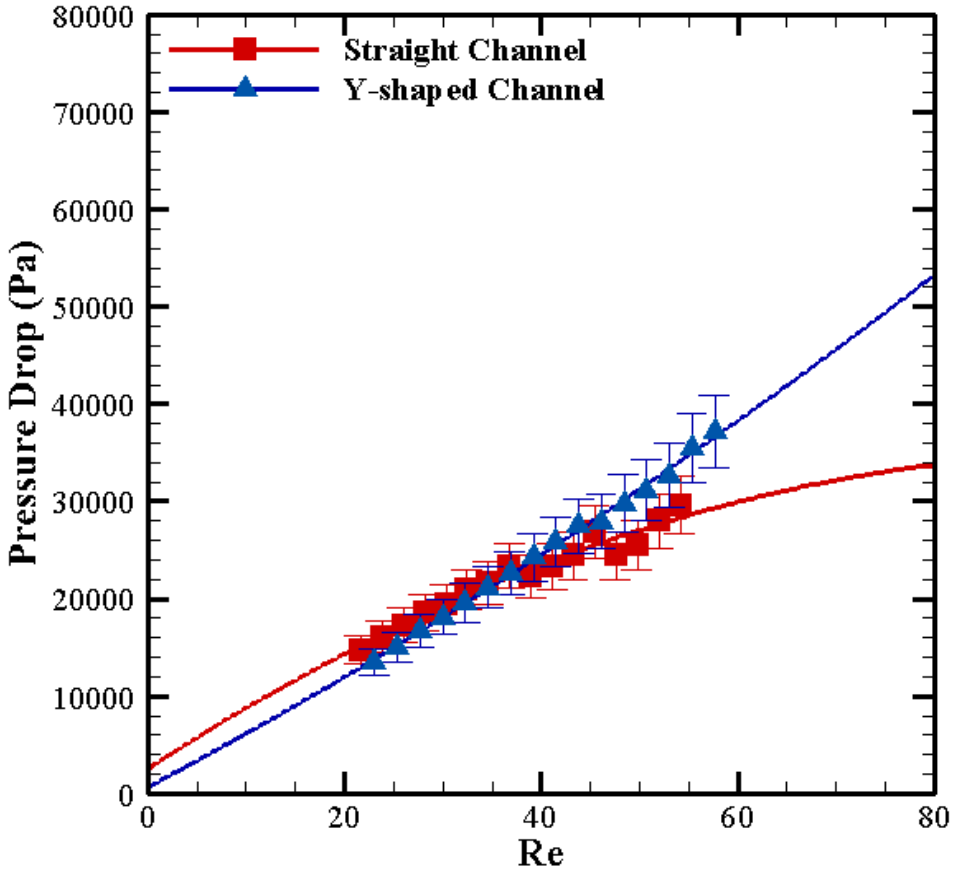

Figure 3.10. Pressure drop vs. Reynolds number for Y-shaped channel.

For the straight microchannel heat sink, the overall pressure drop has six components. The flow from the inlet tube will turn 90 degrees and go to the reservoir. As it flows to each microchannel, it experiences a sudden contraction which causes the flow to separate and undergo an irreversible free expansion. In the core, the liquid flow will have skin friction and a density change due to heating. As it approaches the outlet, there is another irreversible free expansion. The flow finally turns 90 degrees and enters the outlet tube. Therefore, the overall pressure drop can be express as:

$$\Delta P_{tot} = \frac{\rho_1 v_i^2}{2} K_{90} + \frac{\rho_1 v_c^2}{2}[1-\sigma^2 + Kc) + 2(\frac{\rho_1}{\rho_4} - 1) + 4f \frac{x}{D_h}\frac{\rho_1}{\rho_m} - (1-\sigma^2 + Ke)] + \frac{\rho_4 v_o^2}{2} K_{90}$$

(3.23)

where v_i and v_o are the velocity of inlet and outlet tube, and v_c is the coolant velocity in the microchannel. K_{90} is the 90 bend loss coefficient, Kc and Ke are the entrance and exit loss coefficients. σ is the ratio of the core free flow to the frontal cross sectional areas, and ρ_m is the average density, which is given by:

$$\frac{1}{\rho_m} = \frac{1}{L}\int_0^L \frac{1}{\rho} dx = \frac{2}{\rho_1 + \rho_4} \tag{3.24}$$

The cross section area at the inlet and outlet are the same, and the coolant density variation is negligible given the temperature range in this study. Hence the total pressure drop can be simplified to:

$$\Delta P_{tot} = \rho v_i^2 K_{90} + \frac{\rho v_c^2}{2}[(Kc + Ke) + 4f \frac{x}{D_h}] \tag{3.25}$$

For the U-shaped channel, the flow experienced another 180 bends. The total pressure drop becomes:

$$\Delta P_{tot\_u} = \rho v_i^2 K_{90} + \frac{\rho v_c^2}{2}[(Kc + Ke + K_{180}) + 4f \frac{x}{D_h}] \tag{3.26}$$

where x is the length of the non-curved part of the channel.

For the Y-shaped channel, the flow experienced the second sudden contraction as it splits into two smaller channels. Hence the total pressure drop becomes:

$$\Delta P_{tot\_Y} = \rho v_i^2 K_{90} + \frac{\rho v_c^2}{2}[(Kc + Kc_2 + Ke) + 4f\frac{x}{D_h}] \tag{3.27}$$

All the equations above assume the flow is fully developed flow. With the aspect ratio of the microchannel 1.75, the 90 bend loss coefficient is estimated to be 1.2. The entrance and exit loss coefficients Kc and Ke for flow between parallel plates evaluated by Kays and London are applied in this study. Developing velocity profile will lead to a smaller Kc and a larger Ke than the fully developed situation. This effect has already been considered in their study for laminar flow. The apparent friction factor, therefore, is reported in figure 3.11 and 3.12.

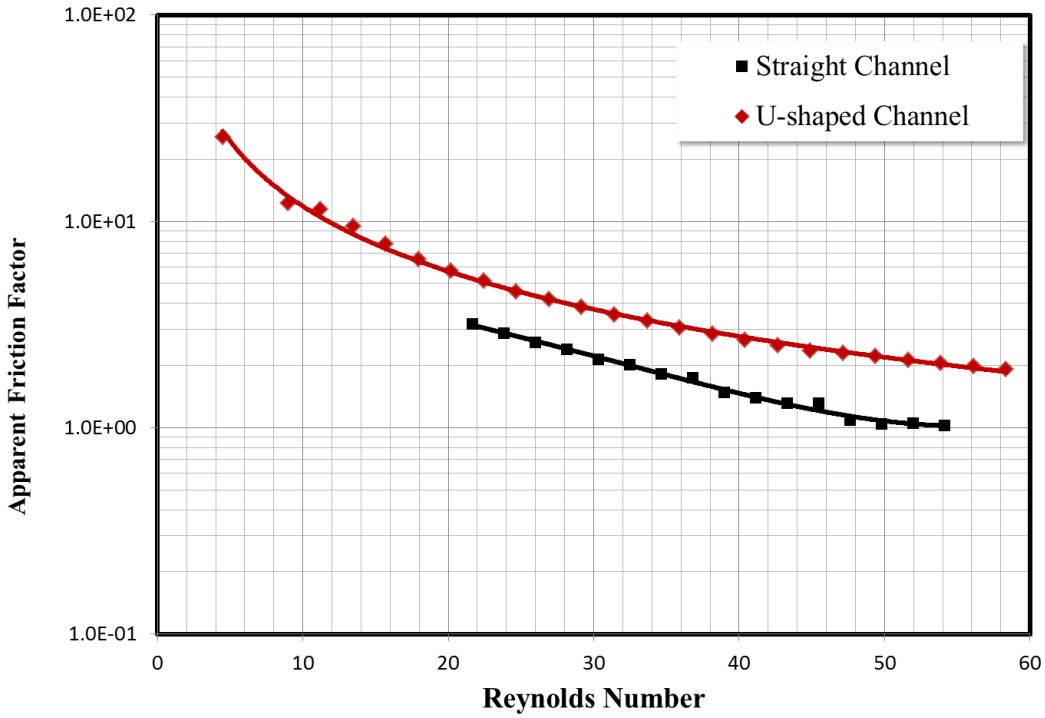

Figure 3.11. Apparent friction factor Vs. Reynolds number for U-shaped channel.

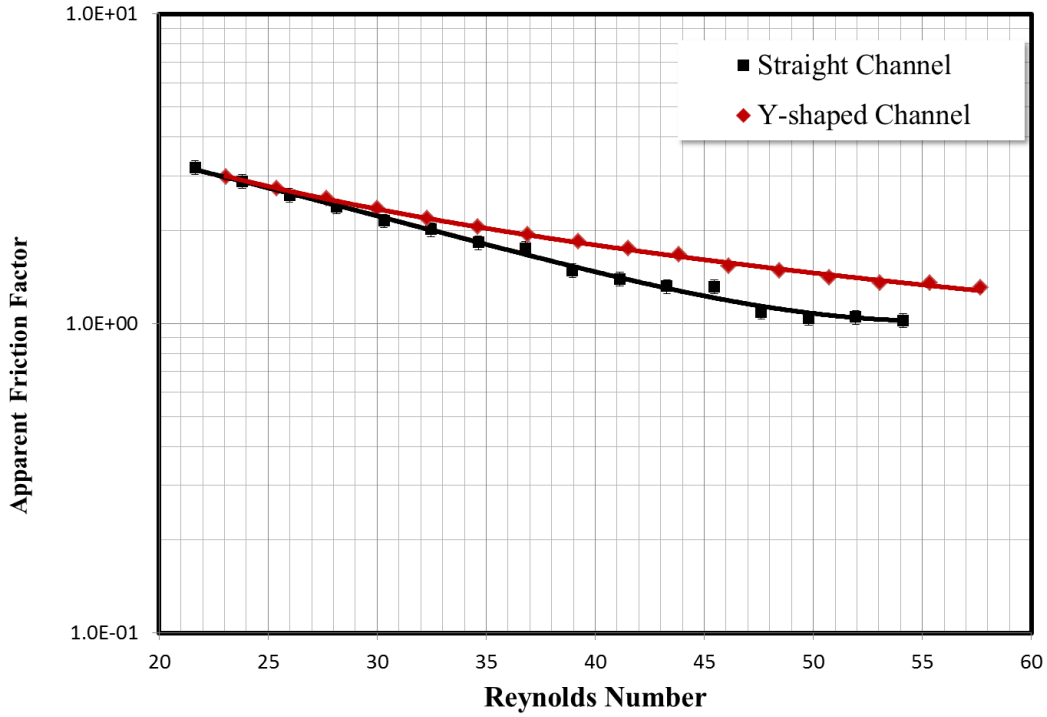

Figure 3.12. Apparent friction factor vs. Reynolds number for Y-shaped channel.

Note that the pressure drop associated with the distribution of the coolant to the inlet reservoir and outlet reservoir was subtracted out since they might vary considerably based on fluid connections and manifolding technique.

3.4 Transient response

All the previous data is considered for steady-state conditions. Assuming the power to the electronic chip is constant, and after the electronic system is turned on and kept running for a long period of time, the temperatures of the electronic chips and cooling devices are

expected to reach steady state. When the thermal equilibrium condition is met, the rates of heat being transferred by conduction, convection, and radiation all remain constant.

The operation time needed for an electronic system varies with its size. For a large electronic system, it may take a very long operation time before the system becomes steady. On the other hand, it may only need several minutes for a cooling system of a small electronic chip to become thermally developed. The maximum heat load, which usually appears at the start or the shutdown for a single electronic chip, makes the transient heat transfer behavior of the cooling an important issue to prevent overheating. Hence, the transient effect of the microchannel heat sink will be studied.

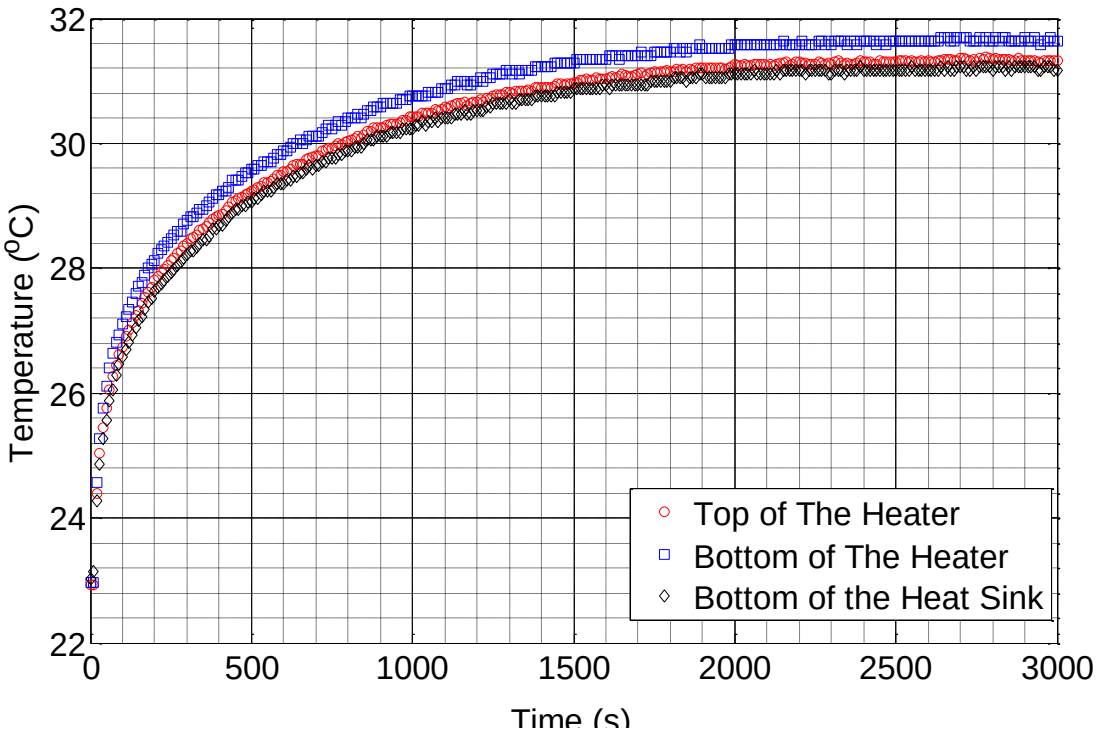

Figure 3.13. Temperature vs. time for straight channel.

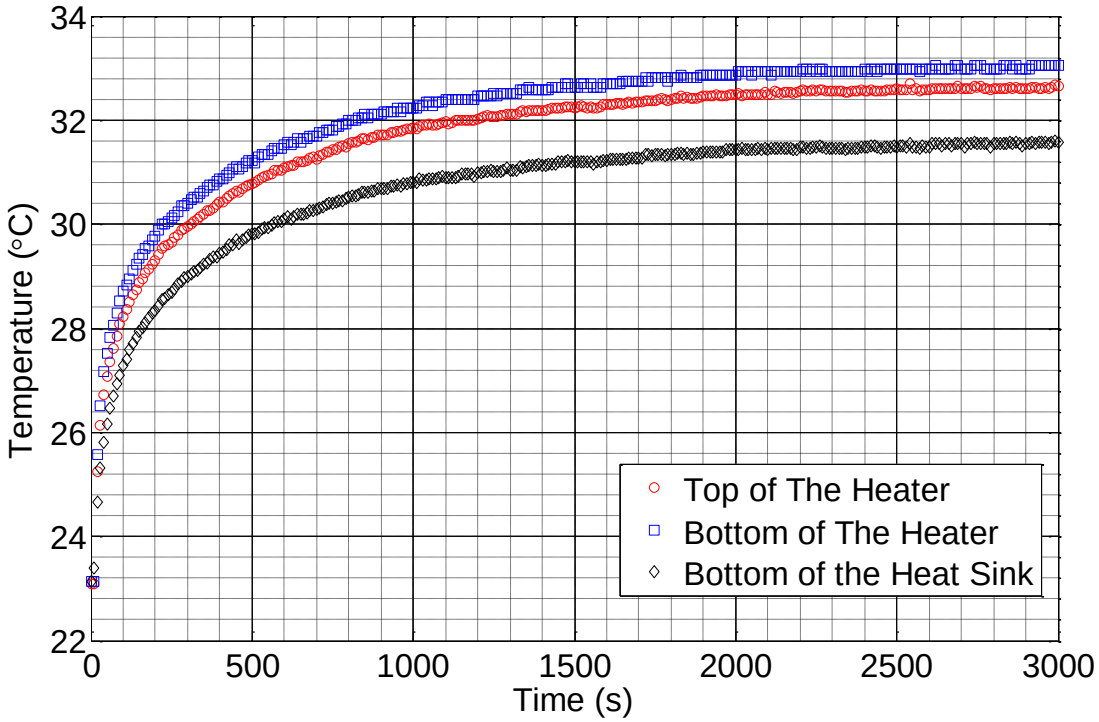

Figure 3.14. Temperature vs. time for U-shaped channel.

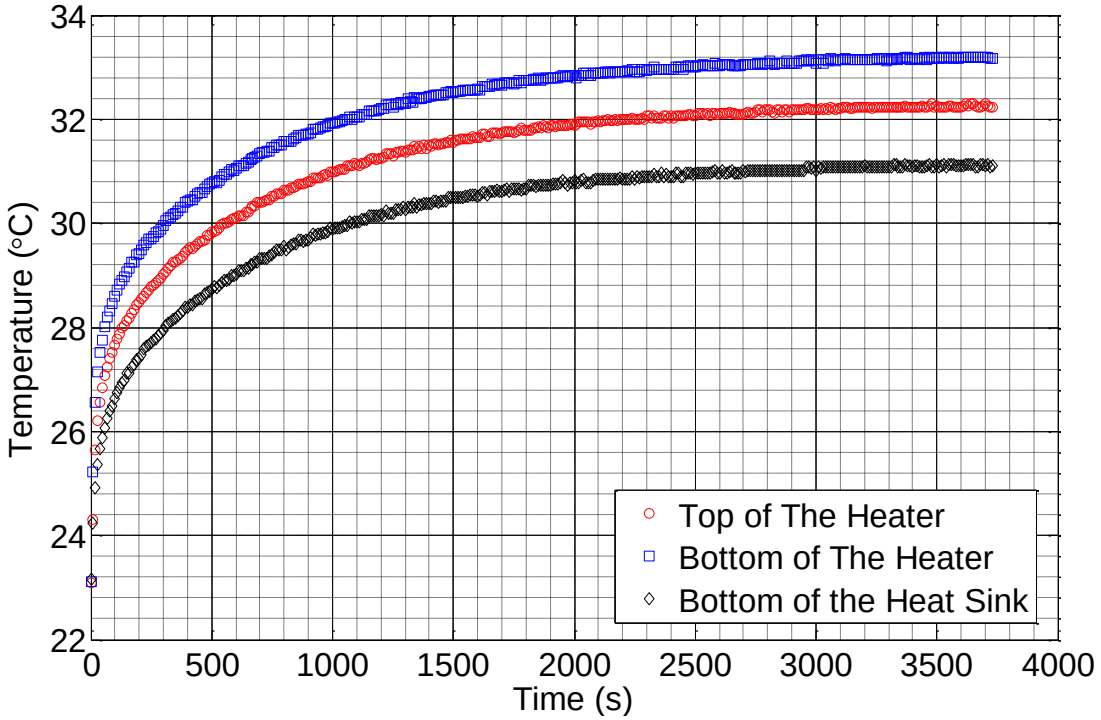

Figure 3.15. Temperature vs. time for serpentine channel.

Three different microchannel heat sinks presented below in figure3.1 a, c and d including straight channel, U-shaped channel, and serpentine channel. The channel width is 50 μm, height 60 μm, and the fin thickness are 200 μm. The total channel numbers for straight, u-shaped and serpentine channel are 41, 19 and 38 respectively. They were all fabricated with wet etching technologies. Three sets of temperature data versus time corresponding to each configuration are shown in figure 3.13, 3.14, and 3.15. The heat flux was 1286 W/m^2, and the flow rate was 0.1 ml/min for all the three cases.

The heating time needed for the temperature rise can be determined when the temperature rise during the heating cycle and the steady state temperature rise are known. The equation is as follows:

$$\frac{\Delta T_H}{\Delta T_{ss}} = \frac{T_r - T_i}{T_s - T_i} = e^{-t/\tau} \tag{3.28}$$

where ΔT_H is the temperature rise that occurs during the heating cycle. ΔT_{ss} is the temperature rise required to ready steady state condition. T_r is temperature at the characteristic thermal response time T_i is initial steady state temperature. T_s is the temperature of final steady state. τ is the time constant, and t is the characteristic thermal response time.

It is convenient to evaluate a thermal design in terms of the time constant τ. When the time constant is known, it is possible to obtain the thermal response of the system. A

convenient reference point is one time constant. When t is equal to the time constant, the equation 3.28 becomes:

$$\frac{T_r - T_i}{T_s - T_i} = \frac{1}{e} \tag{3.29}$$

where e = 2.718. This shows that one time constant represents a temperature increase that is 63.2% of the steady state temperature rise. The response time can be obtained from the temperature data recorded during the experiment, shown in figure 3.16, 3.17, and 3.18. The accuracy of the response time is ± 5 second. It was found that the response time of the heat sink is shorter than the heater. For example, when the flow rate is 0.3ml/min, the response time for the U-shaped microchannel heat sink is 107 second, and 81 second for the heater on the bottom of the heat sink. This was mainly caused by the larger thermal resistance at the heater and heat sink interface. The conduction at the interface and silicon substrate causes the response delay of the heat sink as well.

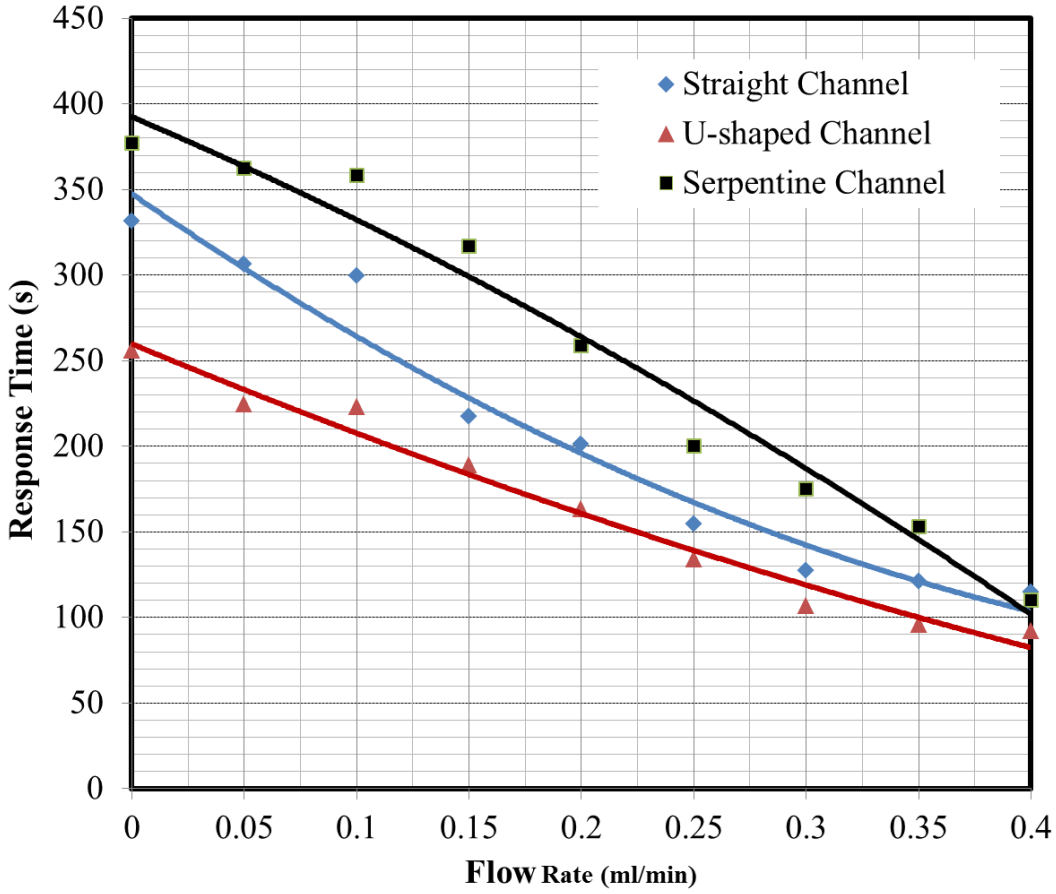

Figure 3.16. Response time vs. flow rate for low heat flux.

The response time has a decreasing trend with an increasing flow rate. The response time t was 92 seconds for U-shaped channel when flow rate was 0.4 ml/min, and heat flux was 1286 W/m^2 as shown in Figure 3.16, while it was 121 second and 110 second for straight channel and serpentine channel, respectively. The U-shaped channel heat sink took a shorter time to reach steady state, and it responded faster and removed heat faster than the other two configurations. This is caused by the flow structure and the ratio of the surface area between solid (silicon) and liquid (distilled water). The edge outside the arc area of the U-shaped channel has large solid area compare with other configurations. The serpentine channels had the lowest heat removal rate within the experimental range. The

difference in the response time between the straight channel heat sink and the serpentine channel heat sink becomes shorter with increasing flow rate at the top surface of the heat sink, even though they still took longer time to reach steady state condition compared to the U-shaped channel.

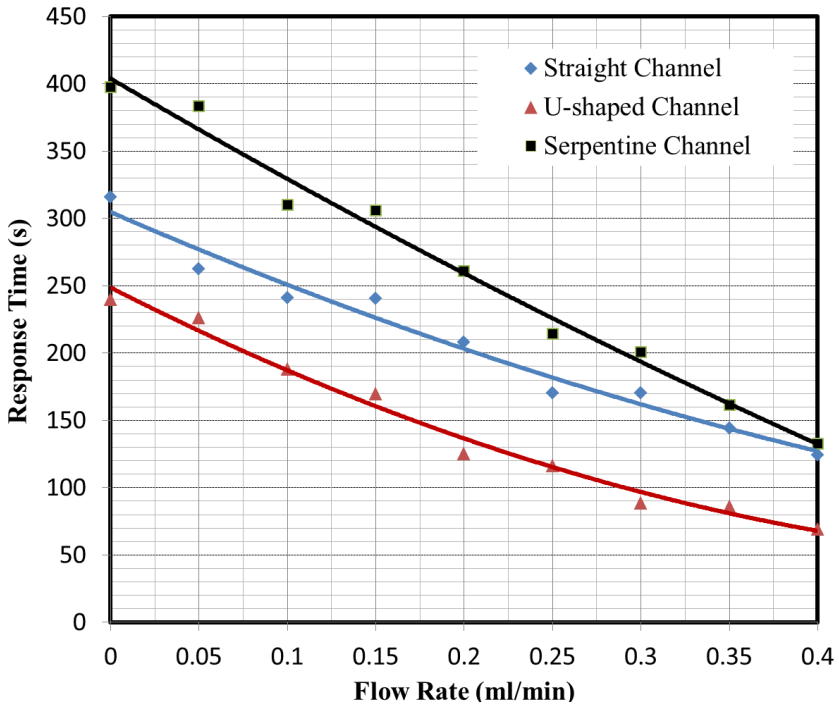

Figure 3.17. Response time vs. flow rate for high heat flux.

Figure 3.17 shows the response time for different flow configurations, with different heat flux but the same flow rate. The flow rate was fixed at 0.4ml/min, and response time varies between 83 sec and 101 sec for a U-shaped channel when the heat flux is increased. Straight channel and serpentine channels had longer response time, compare with U-shaped channel. Overall, the influence of the heat flux to the response time is smaller than the influence of the flow rate.

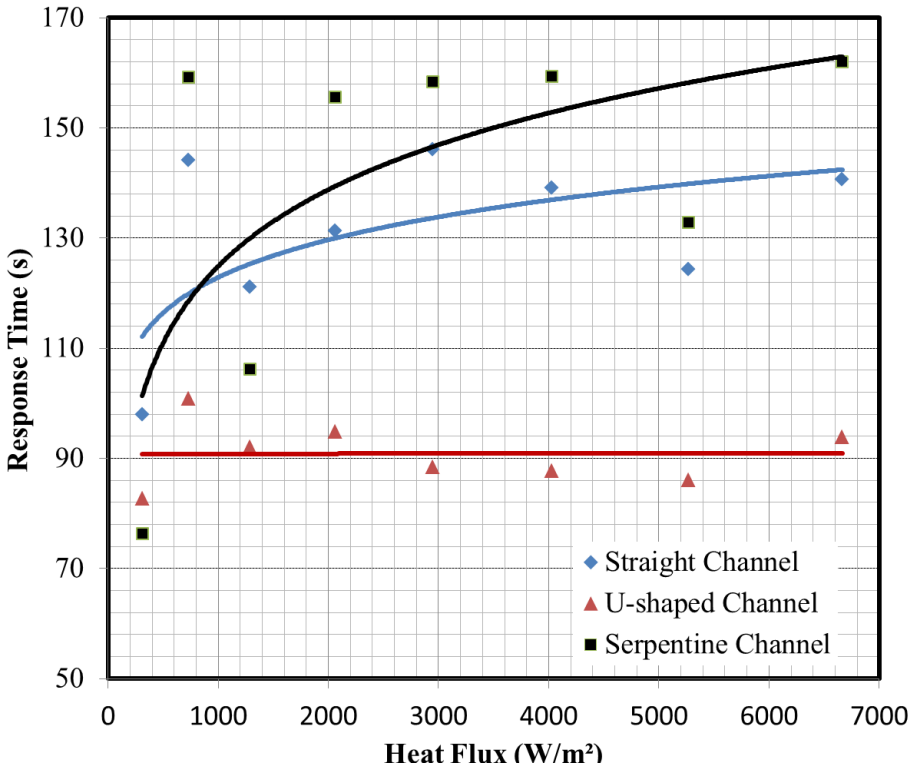

Figure 3.18. Response time vs. heat flux for different heat sinks.

Chapter 4 Numerical Simulation and Parametric Study of Microchannel Heat Sink

The purpose of this chapter is to build numerical models for the heat sink devices tested in the experiment including the straight channel, bended channel, and Y-shaped channel. The numerical models will be calibrated by the experimental results. The validated numerical models will be used to extend the experimental analysis to include higher aspect ratio channels and high Reynolds number flows. Effects of natural convection and radiation, viscous dissipation, and axial heat conduction are discussed. The numerical models are applied with constant pressure drop, constant pumping power and constant volumetric flow and the results will be presented and discussed.

4.1 Numerical model construction

4.1.1 The effect of viscous dissipation

The viscous dissipation refers to converting energy from work done by shear force of the liquid to heat. The coolant experiences a pressure drop due to friction as it flows downstream. Assuming that the walls are adiabatic, the thermal energy converted from the pressure drop will lead to the fluid temperature rise:

$$\Delta T_{vh} = \frac{\Delta P}{\rho C_p} \tag{4.1}$$

where ΔP is the pressure drop, ΔT_{vh} is the temperature rise due to viscous heating, which is independent of the heat flux applied on the walls. The effect of viscous heating can be significant given a large pressure drop. However, the effect of viscous heating on temperature is small for this study especially for the study range of the experiment. For example, room temperature (20 ºC) DI water with a pressure drop of 100kP will only lead to a temperature rise of 0.02 ºC. Hence, the effect of viscous dissipation on temperature rise is neglected in this study.

4.1.2 The heat transport mechanism other than forced convection

The effect of radiation heat transfer is small for electronic chips with high heat dissipation. The amount of heat removed by radiation can be calculated by the Stefan-Boltzmann Law. Tsutomu Sato (1967) observed that the emissivity of silicon varied from 0.4 to 15 at various temperatures from 340 K to 1070 K. For our study, the temperature of silicon is below 100 ºC. With a relatively low emissivity, the heat transferred by radiation is a small portion compare with the overall heat dissipation, which can be up to $1000 w/cm^2$ nowadays. Hence, radiation heat transfer is negligible for this study.

The free convection will become significant with high temperature gradient, large characteristic length of dimensions, or low diffusivity. A dimensionless number, Rayleigh number is used to characterize convection problems in heat transfer.

$$Ra_x = Gr_x \Pr = \frac{g\beta}{\nu\alpha}(T_s - T_\infty)x^3 \tag{4.2}$$

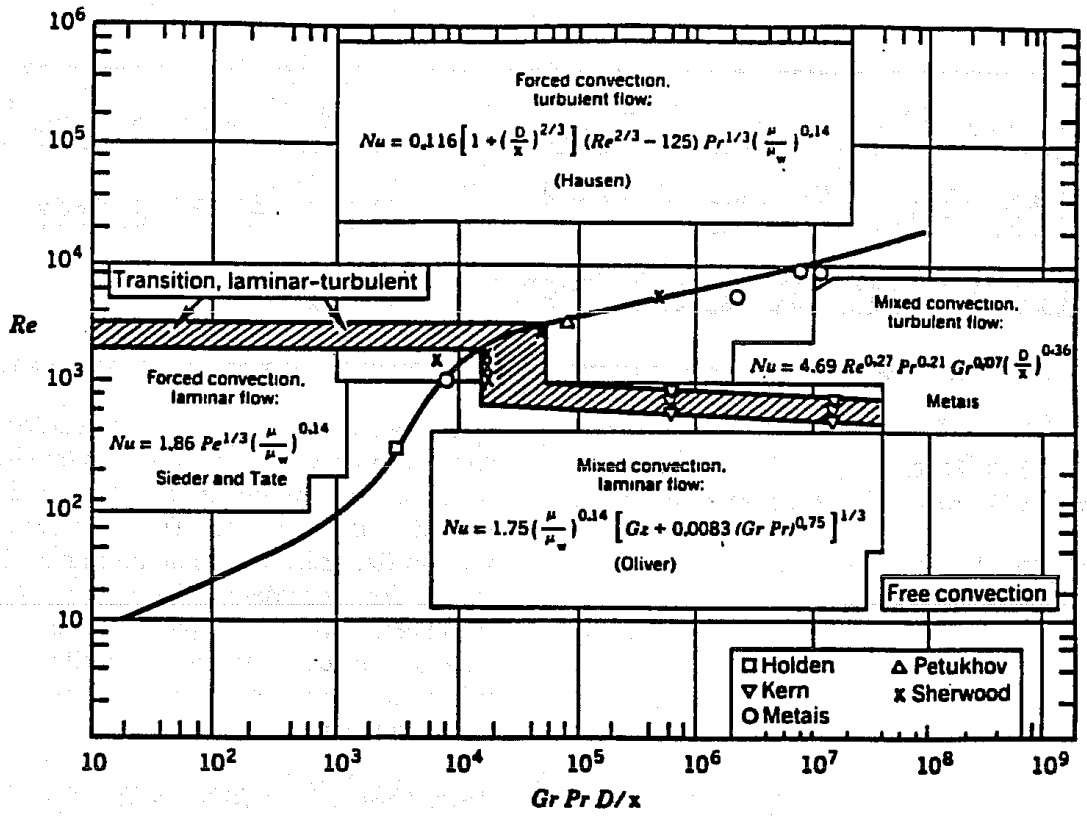

Figure 4.1. Free, forced and mixed convection regimes for flow in horizontal tubes. (Taken from Metais and Eckert).

Metais and Eckert recommended using figure 4.1 to identify the pure forced convection or the mixed convection heat transfer regime. The shaded area is the transition region. For any flow with given Reynolds number, the value of the parameter RaD_e/x represents whether it is necessary to consider buoyancy effects. In this study, if the velocity through the microchannels is low enough, the free convection may have significant effect on the heat transfer. One the other hand, if the Reynolds number is larger enough, and RaD_e/x

is small enough, then the superimposed natural convection is not important. For example, for room temperature water, the thermal expansion coefficient is about $\beta = 2.07 \times 10^{-4} K^{-1}$, the density is $998.3 kg/m^3$, and kinematic viscosity $\nu = 1.04 \times 10^{-6} m^2/s$, with the worst case scenario of $\Delta T = 100$ ºC, the Rayleigh number is of order 1. This suggests that the contribution of natural convection to the total heat transfer is small. Hence, it is not accounted in the numerical model.

4.1.3 The physical model

It is computationally intensive to model the entire microchannel heat sink with 56 (for straight and Y-shaped channel) or 28 microchannels (for U-shaped channel). Therefore, simplified domains were used in this study. Figure 4.2 and figure 4.3 shows the schematic computational domain of three different configurations of microchannel heat sink devices tested in the experiment.

For the straight microchannel heat sink, because the entire heat sink is geometrical symmetric, only half of the fin and half the microchannel are modeled as shown in figure 4.2(b). The left boundary and the right boundary are planes of symmetry. At the bottom of the silicon substrate, a given constant heat flux q was imposed. In the experiment, the top wall of the heat sink was covered with PDMS and its conductivity is three orders of magnitude lower than that of silicon, it is assumed to be an adiabatic wall. The front (z=0) and the back boundary (z=1cm) are velocity inlet and pressure outlet respectively.

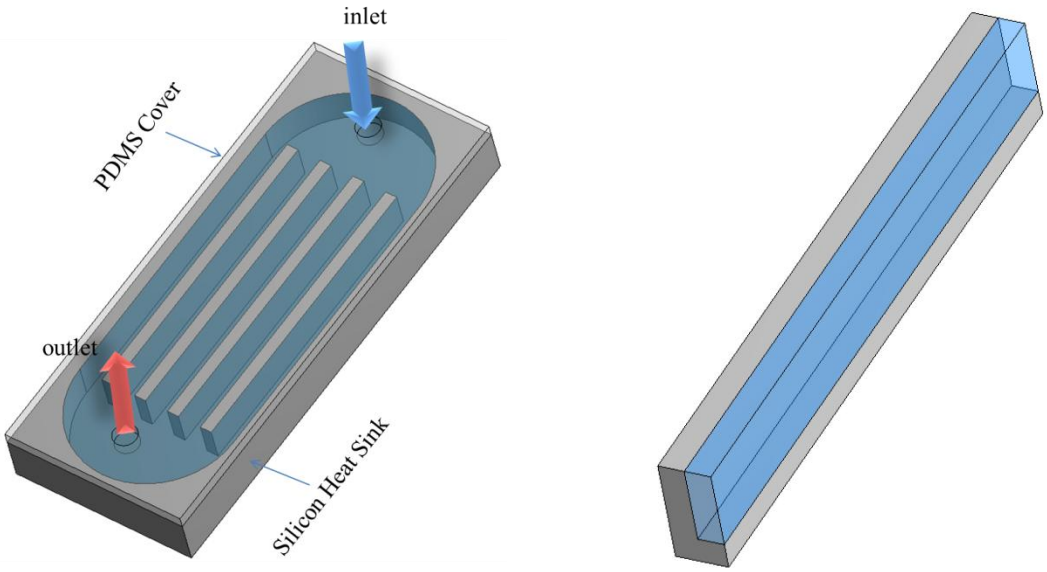

(a) General configuration (b) Computational domain

Figure 4.2. Sketch of straight microchannel heat sink model.

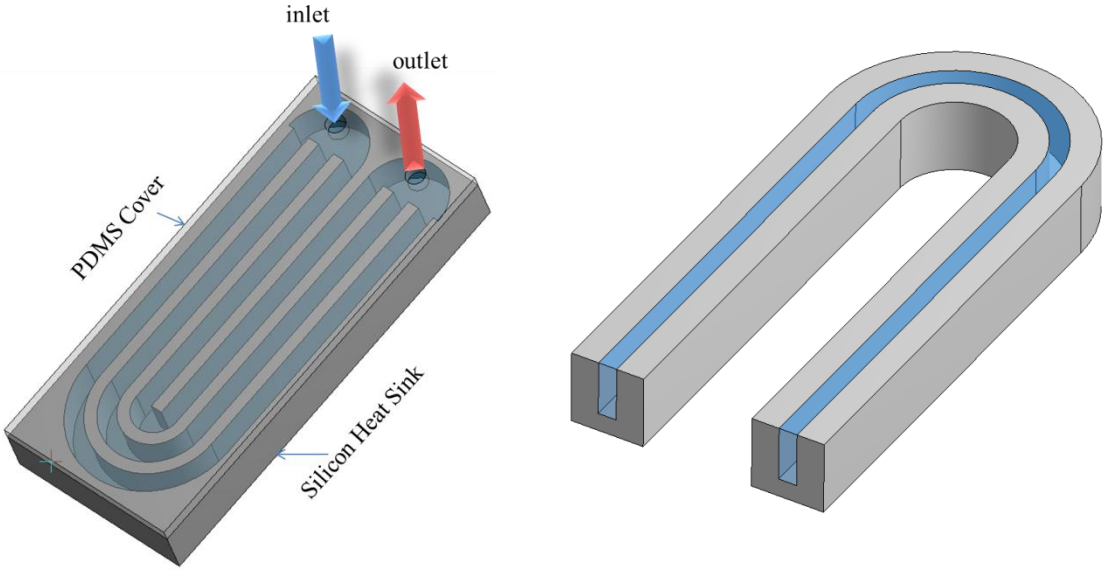

(a) General configuration (b) Computational domain

Figure 4.3. Sketch of U-shaped microchannel heat sink model.

It is noted that for the U-shaped channel, the length of each channel is different. The channel located at the center of the heat sink as shown in Figure 4.3(b) is chosen for our study as the computational domain because there is very little spreading of the heat towards the sides at the center. The computational domain for Y-shaped channel is shown in Figure 4.4. For the first segment of the microchannel, half of one channel and half of one fin with symmetric boundary condition were used. As the flow splits in the second segment of the channel, two half channels with one fin in the middle were chosen as the computational domain.

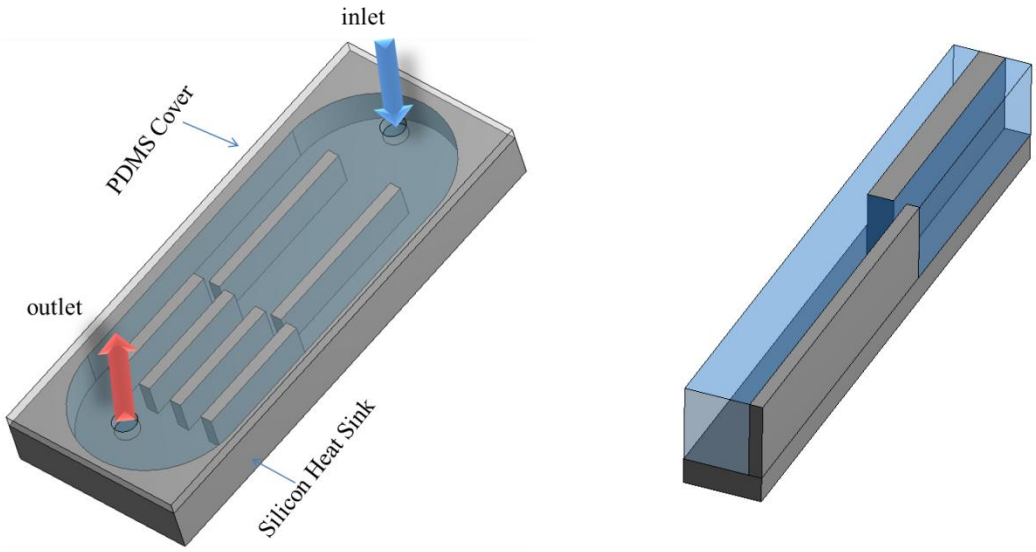

(a) General configuration (b) Computational domain

Figure 4.4. Sketch of Y-shaped microchannel heat sink model.

4.1.4 Mathematical formulation:

The mathematical formulation of the problem is described in this section. The numerical method used for this study is also discussed here.

a) Governing equations:

The single phase liquid fluid behaves as continuum, incompressible, and laminar in the presented study range, and there was no electrokinetic flow behavior. Therefore, the conservation of mass, momentum and energy equations are applicable for solving the steady state temperature and pressure:

Continuity equation:

$$\nabla \cdot \boldsymbol{V} = 0 \tag{4.3}$$

Navier-Stokes Equations:

$$\rho \boldsymbol{V} \cdot \nabla \boldsymbol{V} = \rho \boldsymbol{g} - \nabla P + \mu \nabla^2 \boldsymbol{V} \tag{4.4}$$

Energy Equation:

$$\rho c_p \boldsymbol{V} \cdot \nabla T = k \nabla^2 T + \dot{q} \tag{4.5}$$

b) Boundary conditions:

In the 3D Cartesian Coordinate system shown in Figure 4.2 to Figure 4.4, at the entrance of the heat sink assembly, uniformly distributed axial velocity and inlet temperature are specified. Velocity along other two directions at the inlet is assumed to be zero. At the exit for both configurations, pressure outlet boundary was used with zero gage pressure. The top wall is assumed to be adiabatic. On the silicon substrate, all the wall surfaces are

assumed to be adiabatic. At the bottom of the substrate, a constant heat flux q is imposed. The left boundary and the right boundary are symmetry boundaries.

The conjugate heat transfer is coupled with the fluid flow in the microchannels for this problem. Hence, the governing equation (4.3) to (4.5), including the continuity, momentum and energy equations are solved simultaneously. The finite volume method (FVM) based on commercial software-ANSYS FLUENT with SIMPLE algorithm was employed to solve the governing equations in the solid and fluid domains. The physical models were meshed with regular structured grid of hexahedral mesh elements. The QUICK scheme, which based on a weighted average of second order upwind and central interpolations of the variable, will generate more accurate results on structured grids aligned with the flow direction. Therefore, it was used to computing convective terms at faces in this study. The grid dependence was tested. The linear set of equations is solved with an implicit linear equation solver (Gauss-Seidel) in conjunction with an algebraic multigrid method. The scaled residual of continuity was set to 10^{-6} and the residual of energy was set to 10^{-8} magnitude as the convergence criterion.

4.1.5 Model validation

To validate the numerical model, the microchannel dimensions used in the experiment are reproduced. The width of each microchannel is 100 μm, the height of the microchannel is 175 μm, and the length of the channel is 1 cm, which is usually the same as the length of the electronic chip.

The inlet temperature recorded in the experiment is used as inlet boundary condition for the numerical model. With the total flow rate shown on the syringe pump during the experiment, given total channel numbers and channel dimensions, velocity at channel entrance is calculate as follows:

$$V_{\text{in}} = \frac{Q}{NW_c H_c} \tag{4.6}$$

where N is the total channel numbers, W_c is the channel width, and H_c is the channel height, Q is the volumetric flow rate.

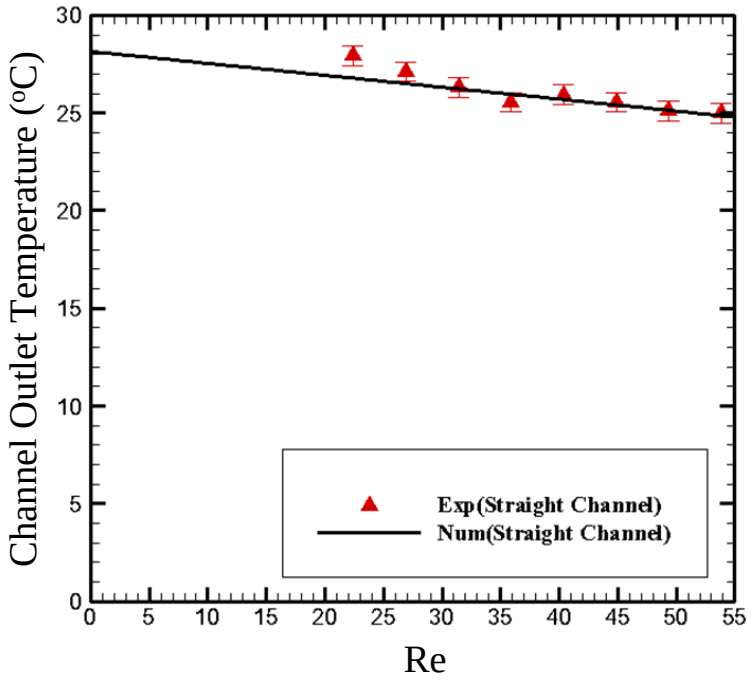

Figure 4.5. Numerical and experimental results comparison for straight channel model.

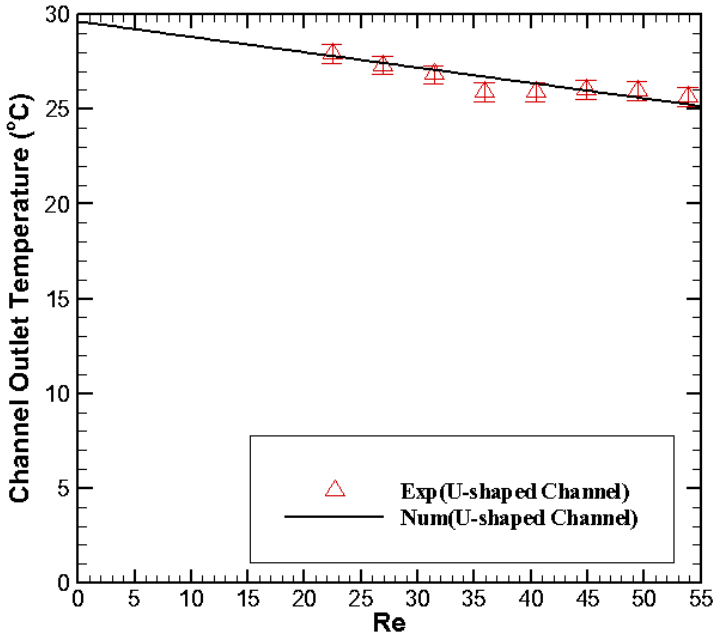

Figure 4.6. Numerical and experimental results comparison for U-shaped channel model.

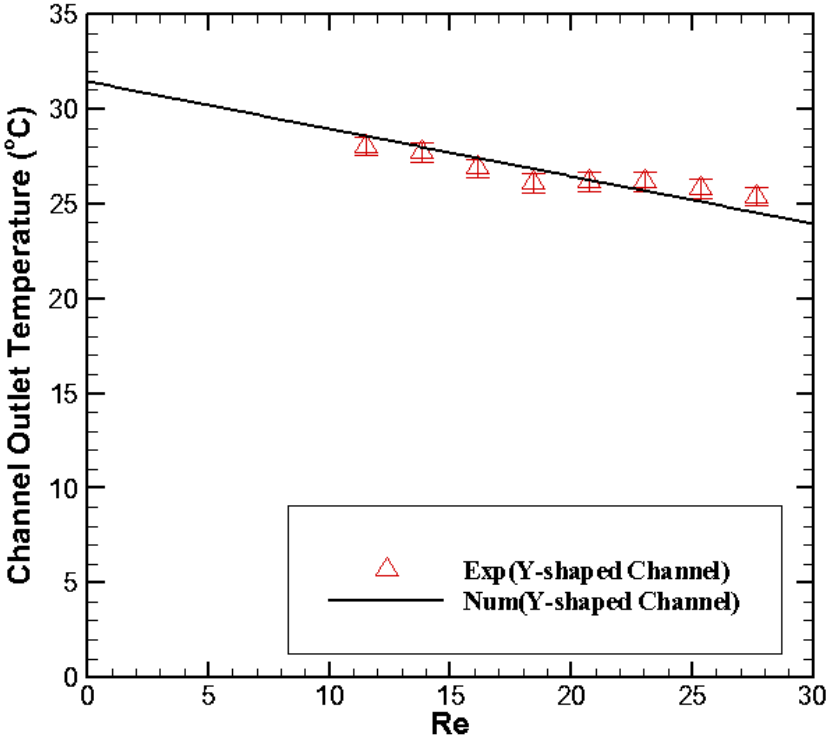

Figure 4.7. Numerical and experimental results comparison for Y-shaped channel model.

The comparison of current numerical study with experiment measured temperature results at the exit of the channel are shown in figure 4.5, figure 4.6 and figure 4.7. The agreement is very good and the difference is within 3.5% for straight channel model, and 2.2% for U-shaped channel model.

4.2 Parametric study for straight channel

The numerical model will be formulated for microchannels with different aspect ratios. Different heat sink material and coolant material will be investigated. The numerical models are also provided for different boundary conditions: constant heat flux, constant pumping power, constant pressure drop, and constant flow rate. When one design parameter is analyzed, all other design parameters will be held constant. The 'baseline' design is the water-cooled silicon heat sink, as described in the experiment. The thermal and fluid performance of other designs will be compared with the 'baseline' case.

Three different aspect ratios $\alpha = 2, 5, 10$ corresponding to small, moderate and high aspect ratio are included in the following figures. The channel height H_c is $300\mu m$, and the channel width w_c is $150, 60, 30\mu m$. The corresponding substrate thickness is $250\mu m$. Note the single channel in the model is used to represent the thermal performance of the heat sink with multiple channels. Hence, the total channel numbers are the same for heat sinks with different aspect ratios. The channel hydraulic diameters are 200, 100, and 54.5μm for the same channel height. The overall flow rate for the heat sink is 70 ml/min for figure 4.7. The corresponding Reynolds numbers are: 92, 115, and 125, respectively.

The actual channel length is 1 cm. The dimensionless axial distance in the flow direction L^+ is defined in equation 3.7. The thermal resistance is defined as:

$$\theta = \frac{\Delta T}{Q} A_s = \frac{\Delta T}{q''} \tag{4.7}$$

where $A_s$is the surface area over which heat flux occurs. The heat flux $q^{"}$ is assumed to be uniform over A_s. Note that the thermal resistance definition is different from equation 3.17. This definition makes it possible to formulate the thermal analysis for the entire heat sink based on a single channel and fin. Also, it makes more sense to compare the thermal performance of difference configurations based on this parameter.

The thermal resistance as a function of distance from upstream rises quickly as the aspect ratio decreases with constant flow rate as shown is figure 4.8. The black line, which represents high aspect ratio channel, has the lowest thermal resistance and shows a less thermal resistance gradient among three cases. Since the fin height and the distance from the channel center to the adjacent channel center are constant, the low thermal resistance for high aspect ratio channel is due to the increase of coolant velocity related to the decrease in the flow cross section area. The thermal resistance for $\alpha = 2$ is 50% larger than $\alpha = 5$.

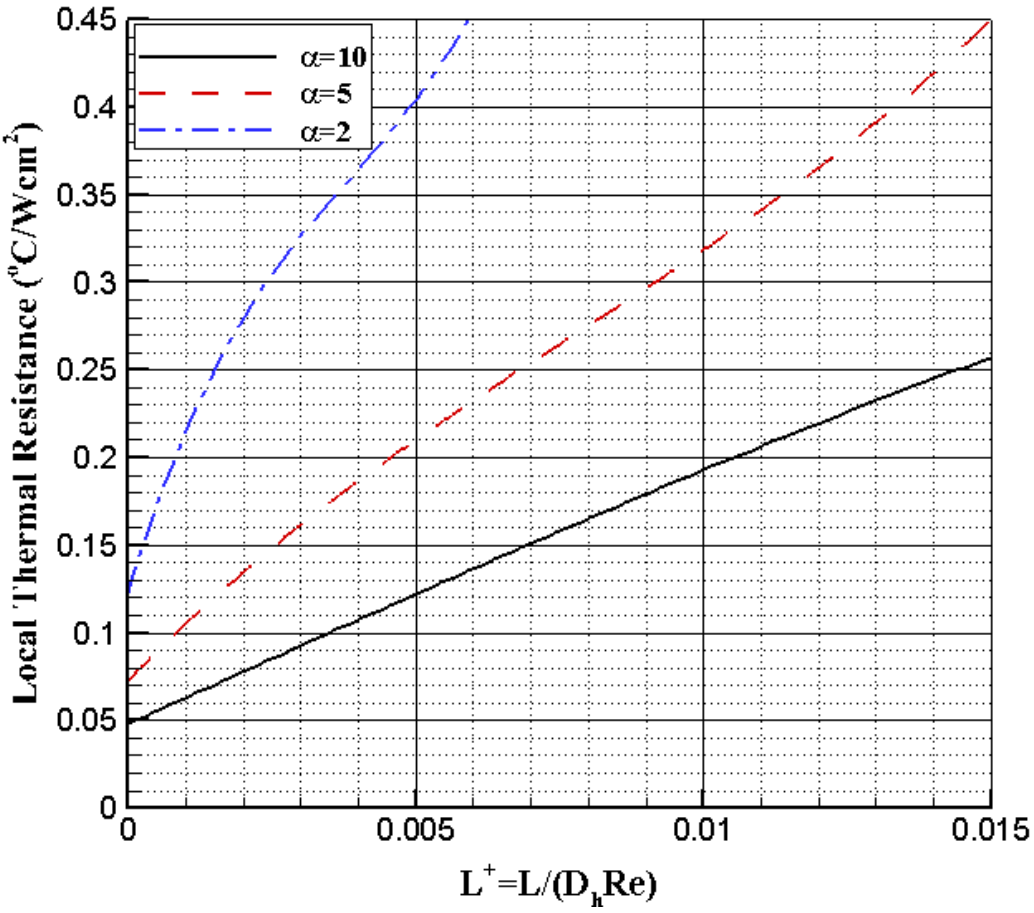

Figure 4.8. Thermal resistance vs. length for different aspect ratio.

The thermal resistance for three different flow rates is shown in figure 4.9. Three cases presented in this plot have identical geometry. The thermal resistance decreases as the flow rate increases as expected. The slope of the curve gets more and more flat when the flow rate becomes larger. When the flow rate is doubled from 70 ml/min to 140 ml/min, the average thermal resistance is increased by 32%. But when the flow rate is increased from 140 ml/min to 280 ml/min, the average thermal resistance is only increased 25%.

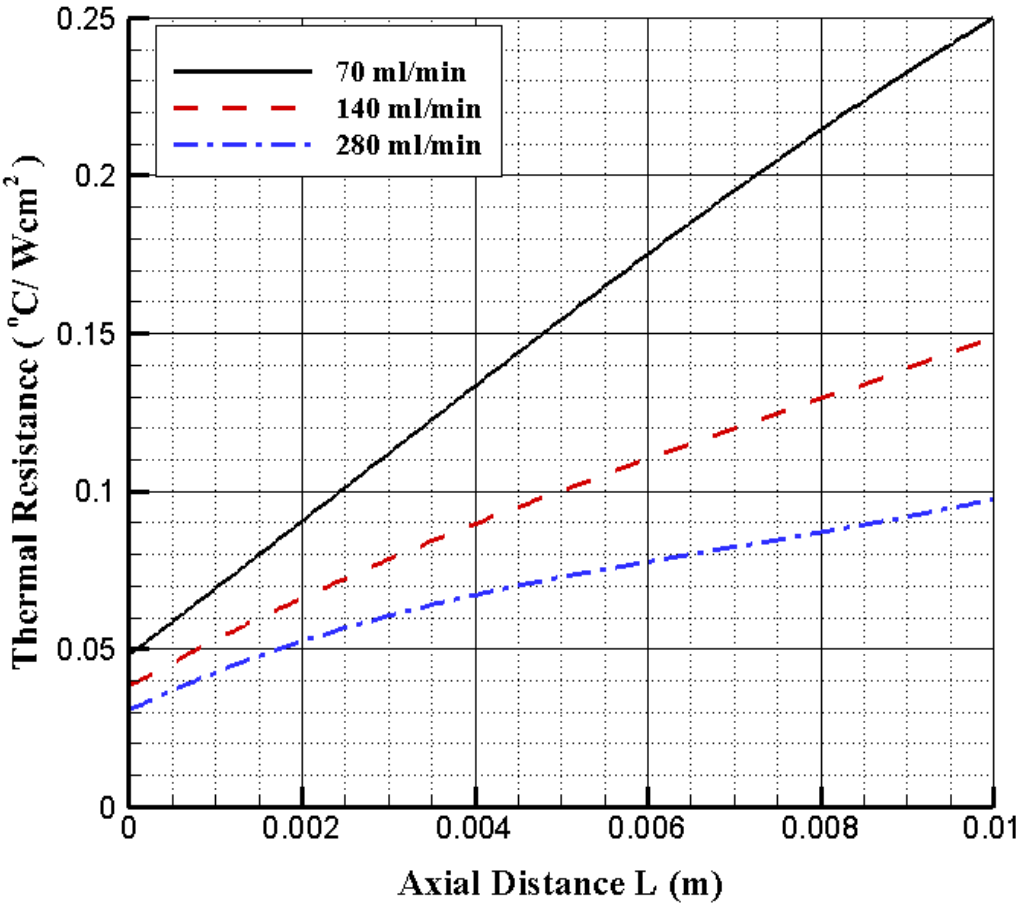

Figure 4.9. Thermal resistance vs axial distance for different flow rates ($\alpha = 10$).

The fluid performance is evaluated by pumping power of the heat sink, which is defined in equation 4.8:

$$\bar{P} = Q \cdot \Delta p = n \cdot u_{avg} \cdot A_c \cdot \Delta p \tag{4.8}$$

The pumping power corresponding to different aspect ratios is the starting points of the curves shown in figure 4.10. It is increased exponentially as the aspect ratio increases. The pumping power is 0.004W for $\alpha = 2$, 0.053W for $\alpha = 5$, and 0.389W for $\alpha = 10$.

Note that the pumping power is continuously increasing with the flow rate for different aspect ratios, as shown in figure 4.10. The pumping power requirements for $\alpha = 10$ are always larger.

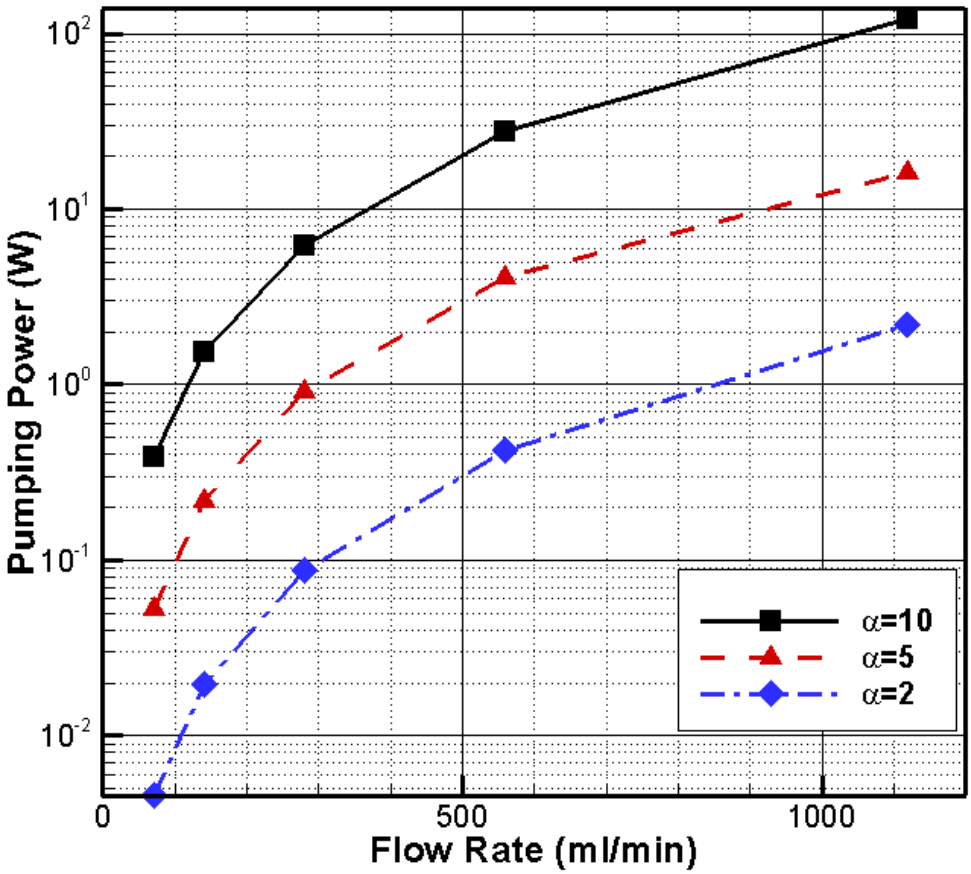

Figure 4.10. Pumping power vs flow rate for cases with different aspect ratios.

The pressure drop is represented by a dimensionless term-- Euler Number. Euler number is defined as:

$$Eu = \frac{\Delta P}{\rho u_m^2} = f_{app} \frac{L}{2D_h} \tag{4.9}$$

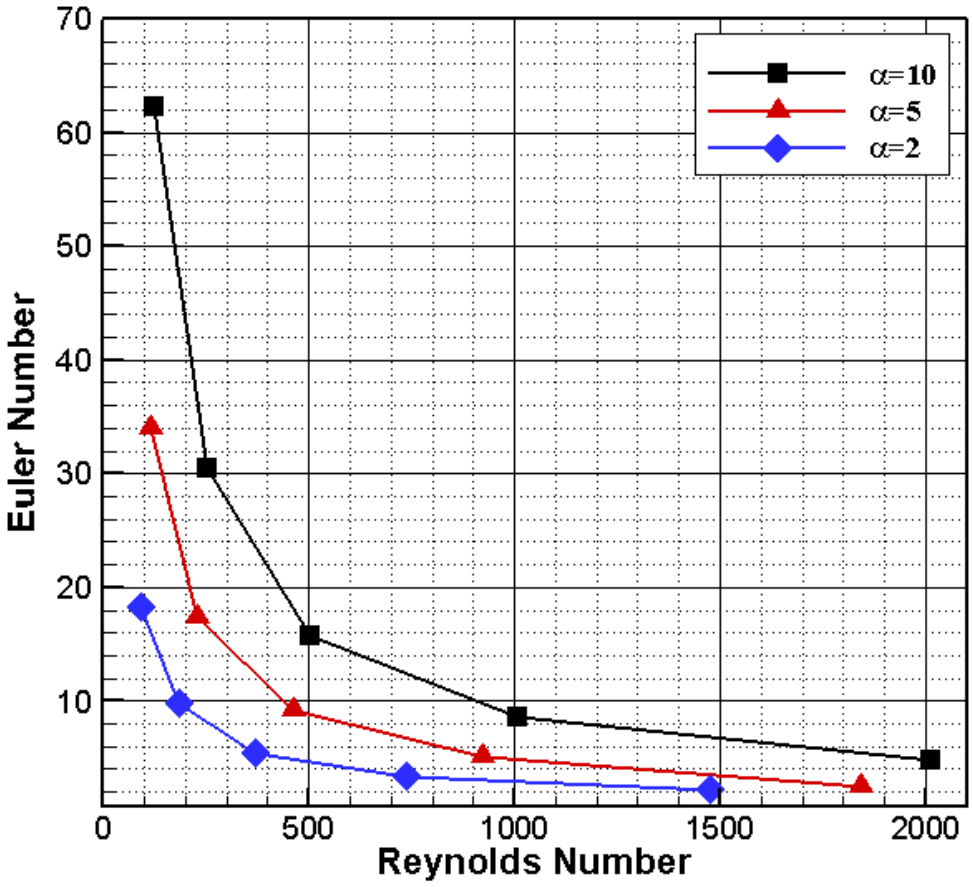

Figure 4.11. Euler number vs. Reynolds number for different aspect ratios.

With constant properties and fixed channel dimensions, Euler number essentially provides the same information as the fanning friction factor f_{app}. In laminar flow region as show in figure 4.11, the Euler number, which is corresponding to a smaller friction factor, keeps decreasing when Reynolds number is increased, but the decreasing rate is dropping. Better thermal performance is reached with high Reynolds number for laminar flow as shown in figure 4.12. The trade-off of reducing the friction

factor as well as thermal resistance is the large pumping power and low energy efficiency.

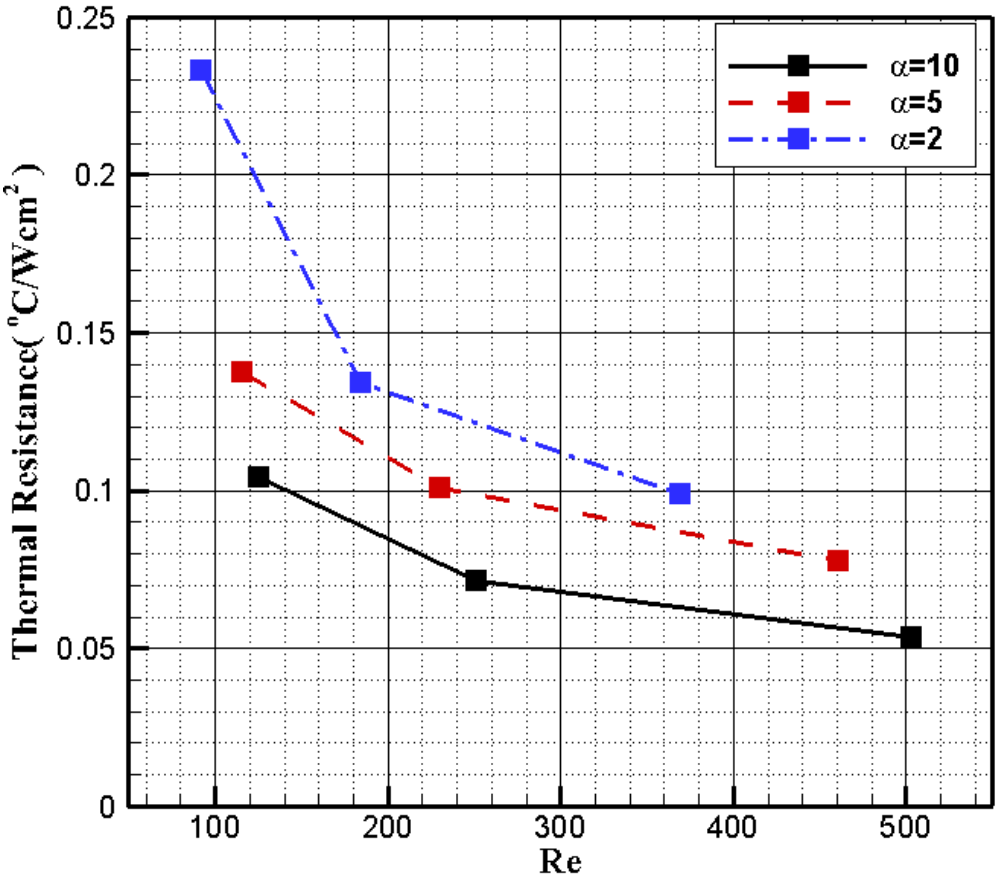

Figure 4.12. Thermal resistances vs. Reynolds number for different aspect ratios.

Figure 4.13 presents the thermal and fluid performance results for comparison of constant pressure drop. Note that the thermal resistance for constant pressure drop constraint behaves similar for $\alpha = 2$ and $\alpha = 5$, though the pumping power of the latter is 3.85 time larger. When the aspect ratio is 10, the thermal resistance is the highest, with a low pumping power requirement (0.16 W).

Table 4.1. Temperature vs. aspect ratio for different heat fluxes.

Heat Flux (W/m^2)	Temperature (°C)		
	$\alpha = 10$	$\alpha = 5$	$\alpha = 2$
100	30.43	33.76	43.26
200	40.86	47.51	66.6
400	71.72	75.02	113.06
Thermal resistance	0.1	0.14	0.23

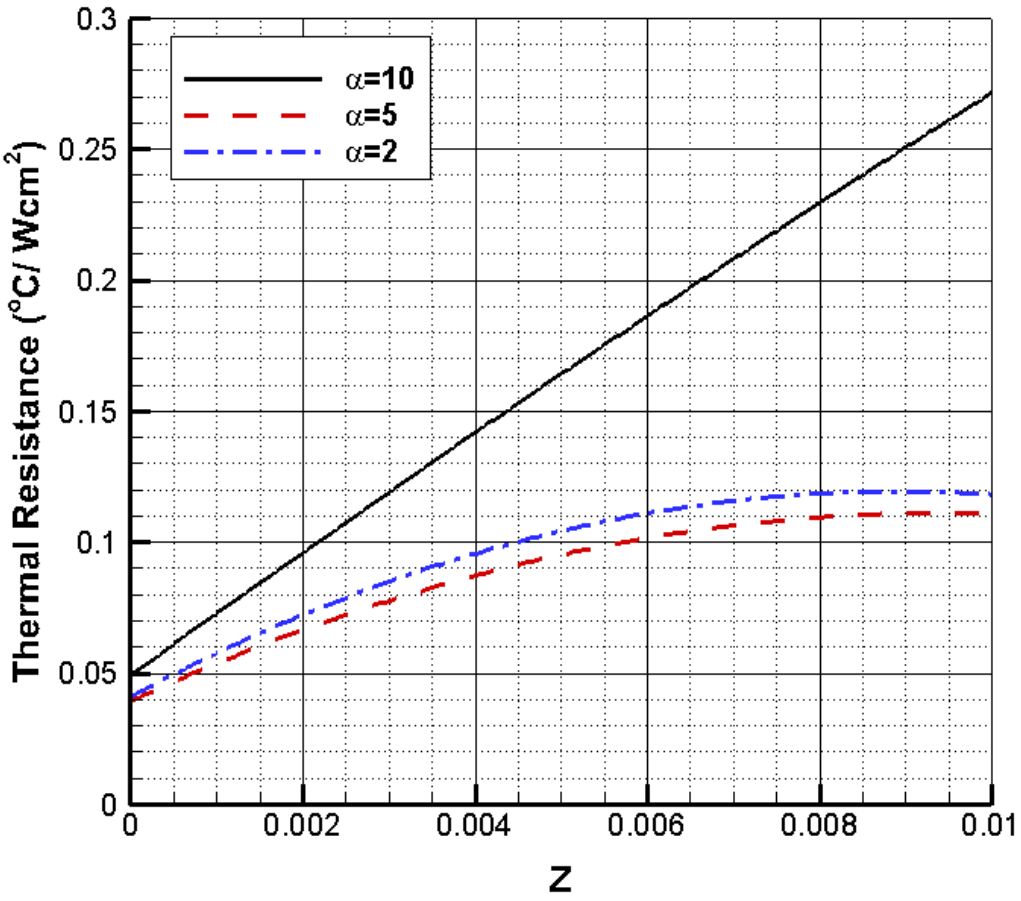

Figure 4.13. Thermal resistances vs. axial distance for constant pumping power.

The average temperature on the bottom of the channel for various heat fluxes is shown in table 4.1 (The pumping power requirements remain the same for the same aspect ratio).

The average thermal resistance of the heat sink with the same aspect ratio is shown in the last row. The purpose of this comparison is to show that the thermal performance of remains the same as the heat flux increases.

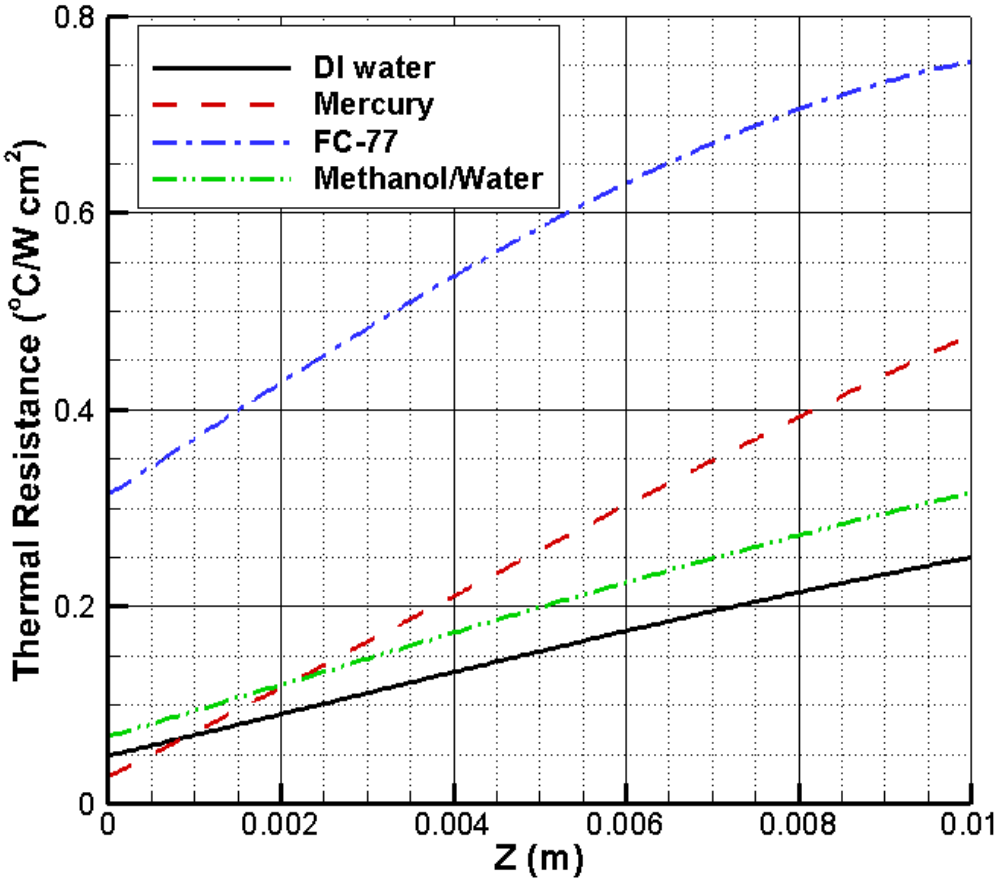

Figure 4.14. Thermal resistances for different coolants at constant flow rate.

Figure 4.14 and figure 4.15 present the thermal resistance for a comparison of various liquid coolants at constant flow rate and constant pressure drop, respectively. The corresponding pumping power of four different coolants is list in table 4.2. DI water

provides the best thermal performance. Methanol/water, which shows the second best performance, is a low cost antifreeze solution finding use in refrigeration services and ground source heat pumps. The major disadvantages of methanol are toxicological and flammable. FC-77 is preferable to water in certain circumstance to avoid contamination and corrosion of the chip when the coolant is in direct contact with the IC chip. Mercury are less practical, though recently, liquid metal has been utilized with magnetofluiddynamic(MFD) pump to remove high heat flux from microprocessors.

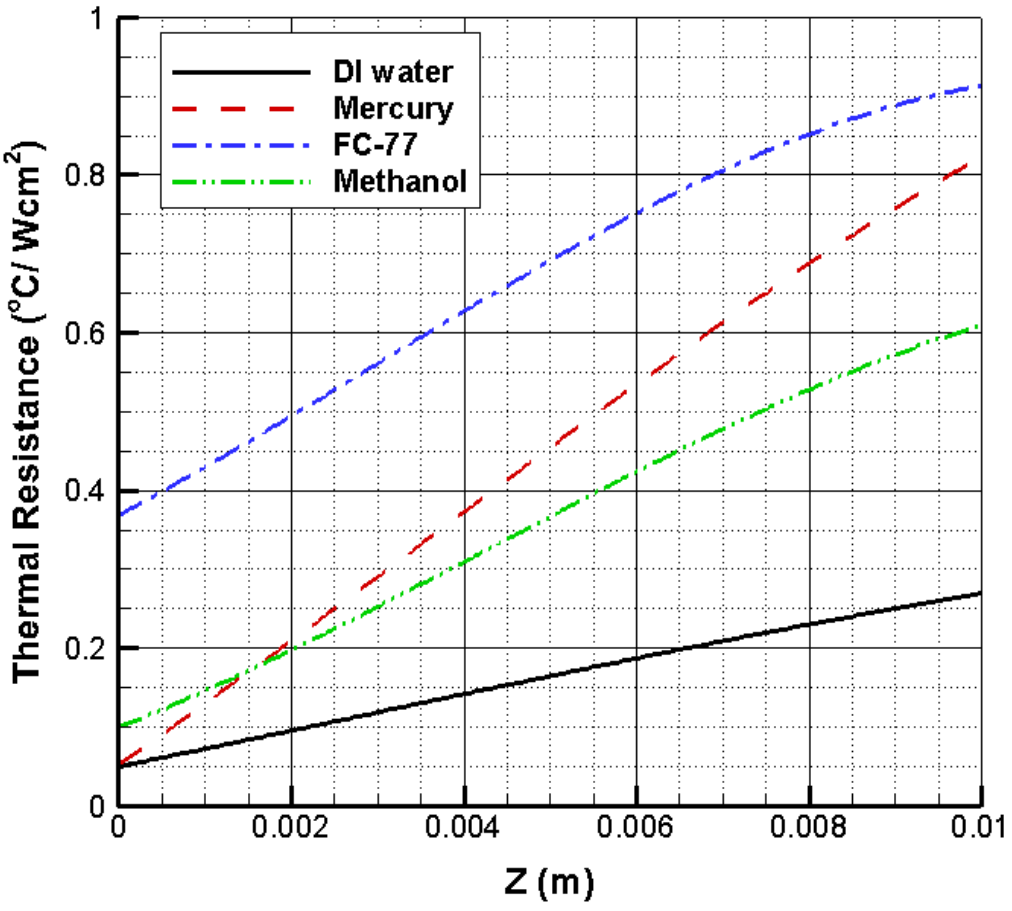

Figure 4.15. Thermal resistances for different coolants at constant pressure drop.

Table 4.2. Pumping power for various liquid coolants ($\alpha = 10$).

Coolant	Pumping Power (W)	
	Constant Flow Rate	Constant Pressure Drop
DI water	0.39	0.16
Mercury	0.66	0.1
FC-77	0.51	0.13
Methanol/water	0.77	0.08

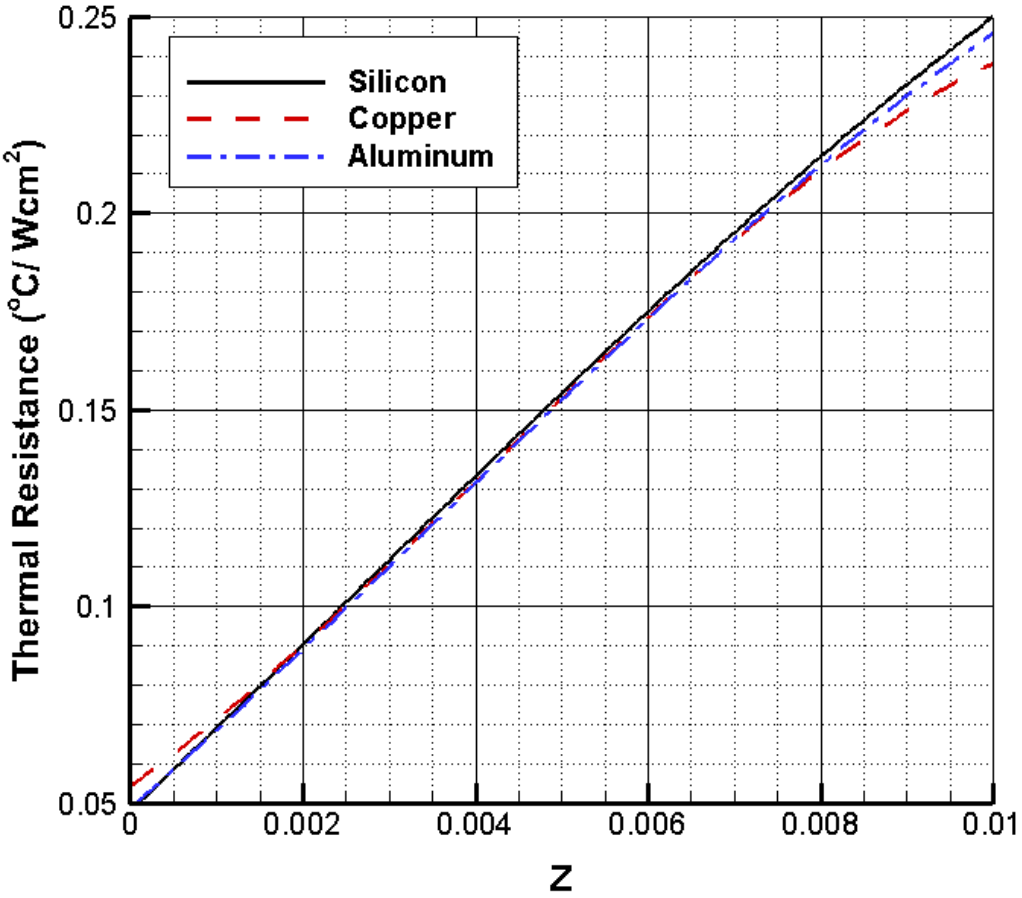

Figure 4.16. Thermal resistances for different heat sink materials at constant flow rate.

Figure 4.16 and figure 4.17 presents the thermal resistance results for a comparison of various heat sink materials. The pumping power requirements won't change. Copper and

aluminum provide slightly smaller thermal resistance due to the higher thermal conductivity compare to silicon, but not significantly. If the copper or aluminum will be used as the heat sink material, an interface will be required instead of directly fabricated on back of the electronic chip. Therefore, an extra interface thermal resistance will be generated and influence the overall thermal performance.

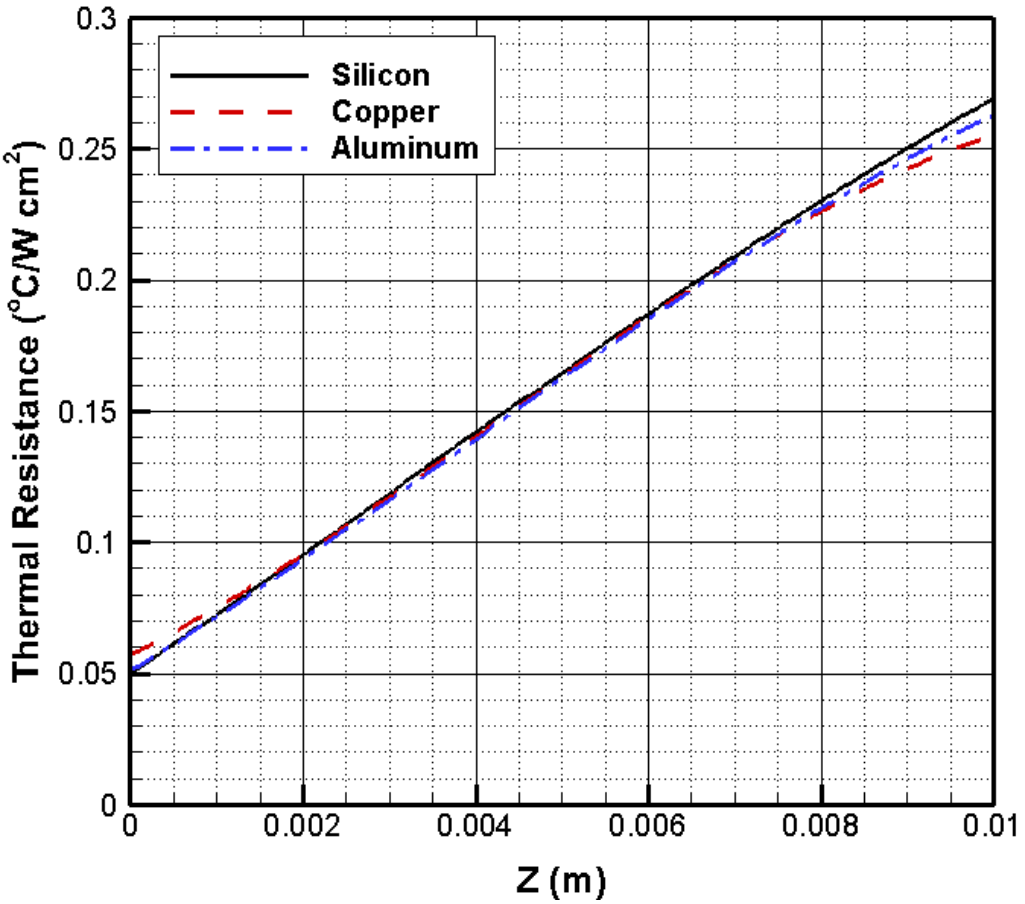

Figure 4.17. Thermal resistances for different heat sink materials at constant pressure drop.

4.3 Effectiveness of channel with bends

The bended microchannel heat sink will be examined in detail in this section. L bend and the 90 bend channel shown in figure 4.18 will be studied. U-shaped channel (180 bend) will be discussed in next chapter. Note that in this study, the single channel is assumed to be one of the microchannels in the middle of a heat sink, which is used to represent overall performance of the heat sink instead of only one channel. In the following results, the total channel numbers of the heat sink are 117 for both L bend and 90 bend. Each microchannel has the same channel cross section area and fin cross section area.

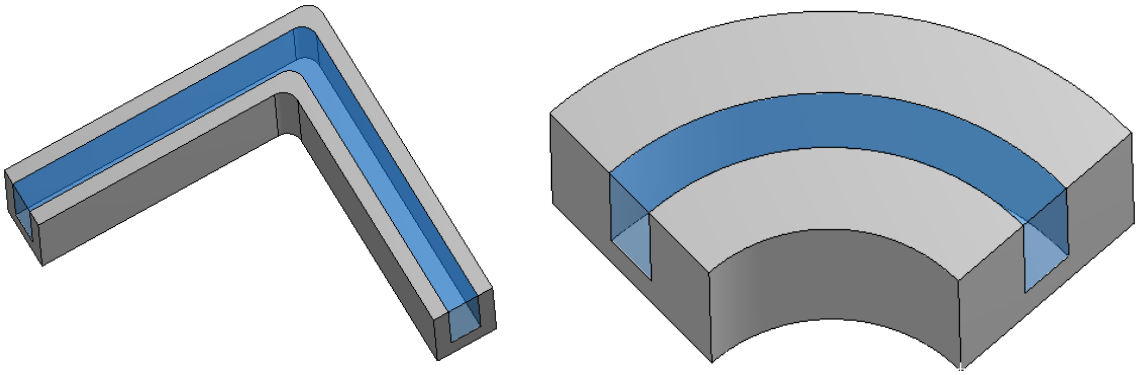

L-bend

90 bend

Figure 4.18. Sketch of L-bend channel and 90 bend.

The cross section pressure distribution along the flow direction is shown in figure 4.19. The height of each channel is 400 μm, and the substrate is 150 μm. The channel width is 54 μm. The left column L-bend microchannel has a smaller rounding corner. The pressure drops more significantly around the corner for the smaller fillet. The streamline plots along the flow direction at different channel height show that there is a vortex formulated at the outer corner as the flow turns, and another vortex were found after the

flow changes directions. This is adverse to heat transfer and may cause the local temperature increase at the corner. A large fillet helps to reduce the local flow circulation as shown on the right column in figure 4.19. For the 90 bend, there is no sharp corner hence the flow turns smoothly.

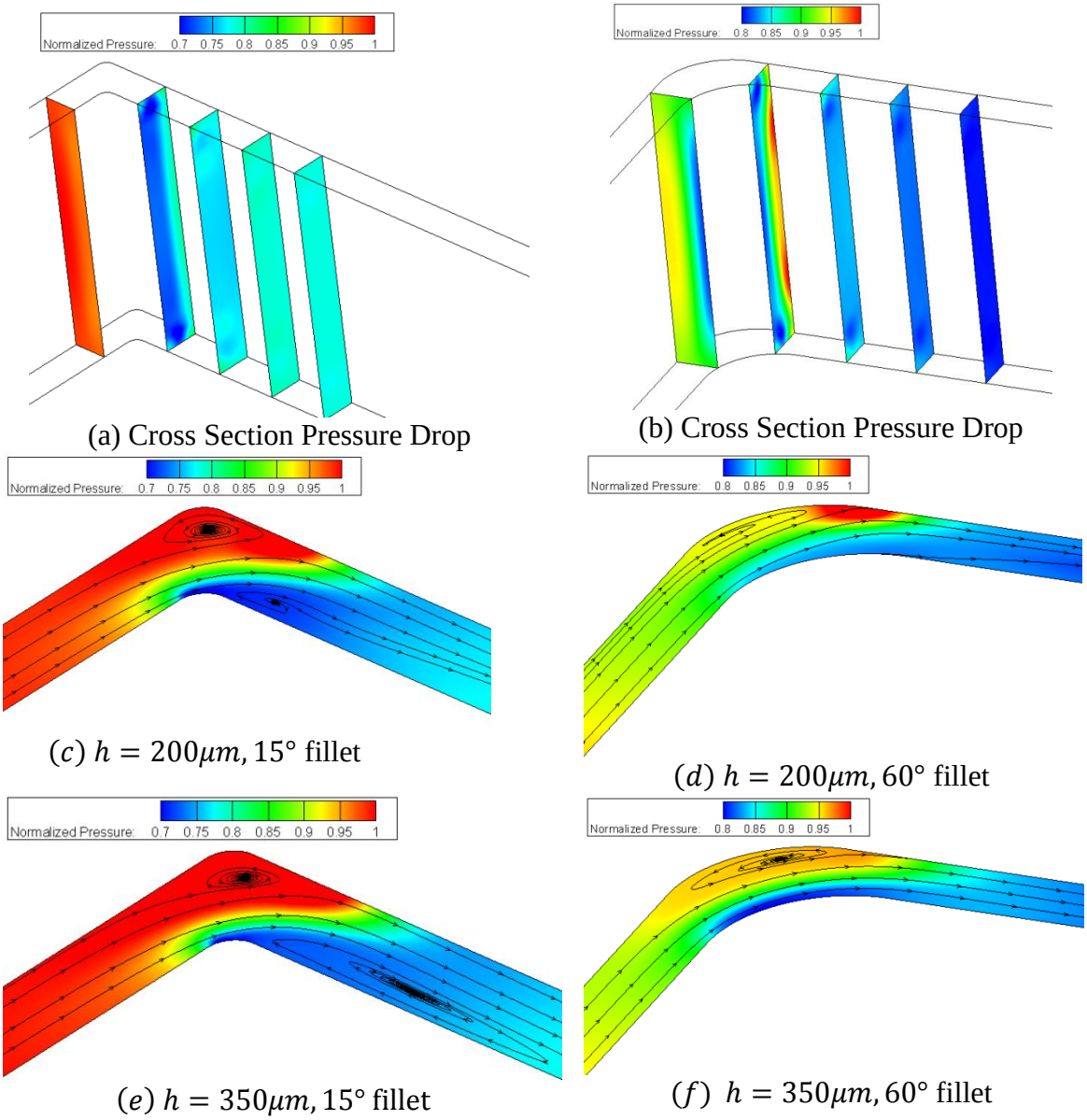

(a) Cross Section Pressure Drop

(b) Cross Section Pressure Drop

$(c)\ h = 200\mu m, 15°$ fillet

$(d)\ h = 200\mu m, 60°$ fillet

$(e)\ h = 350\mu m, 15°$ fillet

$(f)\ \ h = 350\mu m, 60°$ fillet

Figure 4.19. Normalized pressure and streamlines for L bend with different fillets.

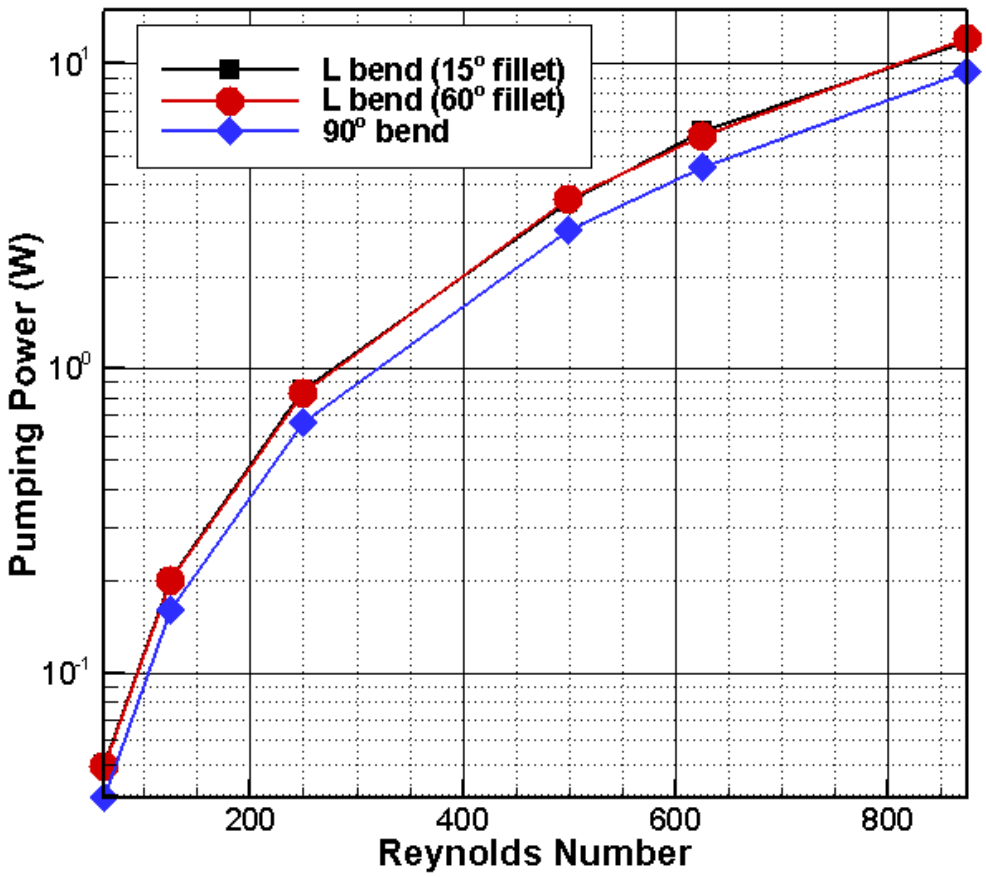

Figure 4.20. Pumping power vs. Reynolds number for L-bends and 90 bend.

Figure 4.20 and 4.21 presents the pumping power requirement and the thermal resistance for L bend and 90 bend. The L bend channel requires larger pumping power than the 90 bend. The thermal resistance of the 90 bend channel is smaller than the L bend channel. The thermal resistance difference decreases as the Reynolds number increases (figure 21). The 90 bend provides a better overall performance in the current study range.

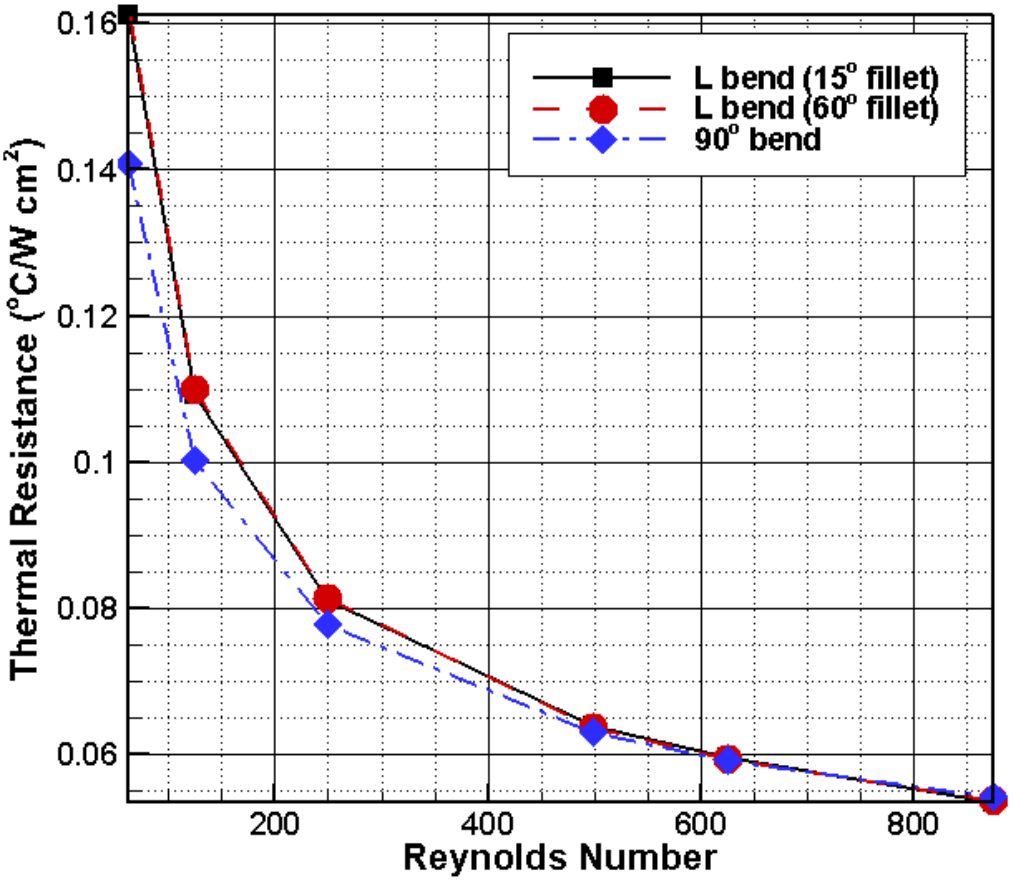

Figure 4.21. Thermal resistance vs. Reynolds number for L-bends and 90 bend.

4.4 Effectiveness of channels with branches (Y-shaped channels)

Given the same inlet coolant velocity, the thermal performance in a channel with fined structure will be enhanced when the flow is not fully developed. In this study, the second segment of the channel structure allows the fluid departure from the fully developed flow from the first segment.

Figure 4.22 shows the temperature distribution at y= 10, 75, and 160 μm in the channel, assuming the heat flux q̇ generated by the electronic chip is 200 W/cm^2, and the flow rate is 150 ml/min. the temperature is higher on the bottom of the channel, and it is more evenly distributed as y increases. It is noted that along the flow direction, the highest temperature happened in the first segment of the device, before the flow splitting into two different channels. It is different from the continuous straight channel, which usually has the highest temperature show at the exit of the channel.

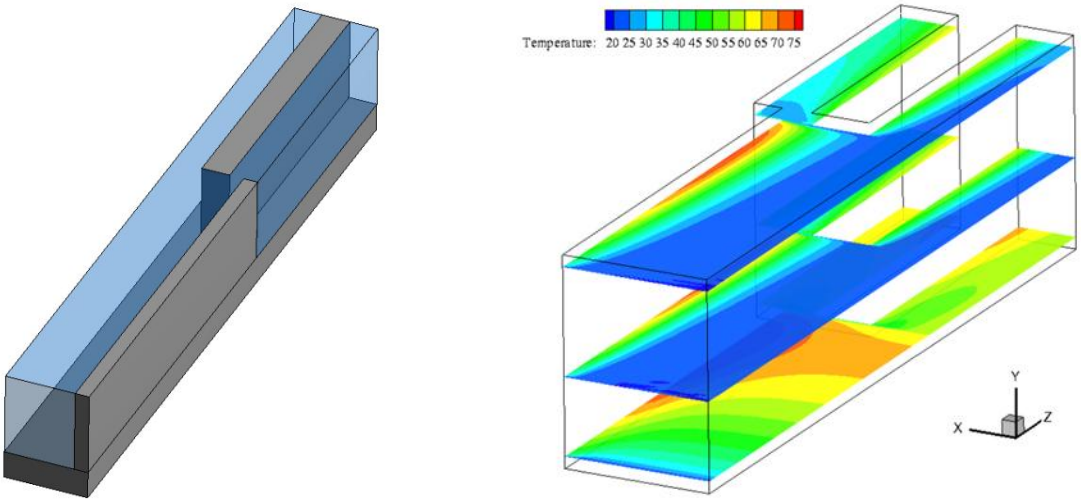

(a) Y-shaped channel sketch (b) Temperature distribution

Figure 4.22. Temperature distribution in Y-shaped channel.

Figure 4.23 gives the velocity distribution along z direction when y is75μm. The velocity reaches the maximum value after the channel pattern changed. The high velocity speed and the remixing at the entrance of the second segment of the channel causes the increasing of the heat transfer rate.

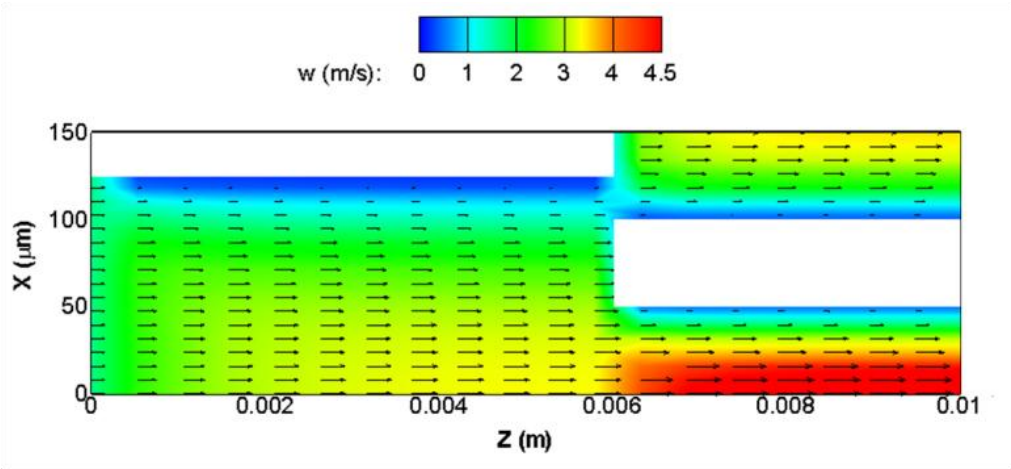

Figure 4.23. Velocity distribution in Y-shaped channel (along the flow direction).

An increase of flow rate appears to be necessary to increase the heat transfer coefficient. The high inlet velocity will increase the pressure drop at the same time. For the same channel length and hydraulic diameter, the pressure drop with inlet Reynolds number 1038 is increased by 77% than the pressure drop at Reynolds number 346, which corresponds to a three times larger flow rate. For low Reynolds number (Re=346), the flow is disturbed but smoothly redirected, so no vortices was created. The flow tends to gathered gradually from the top and bottom of the side walls to the center as shown on the left in Figure 4.24. High Reynolds number will tend to create transverse vortices. For example, when Re is 1038 in this study, two pairs of vortices were generated closer to the fin shown on the right in Figure 4.24. The vortices happened at the cross section area allow for transverse coolant mixing, which spreads out the downstream high coolant temperatures from high heat dissipation zones. They also draw more coolant to the hot-spots since the coolant viscosity is lower at high temperature region.

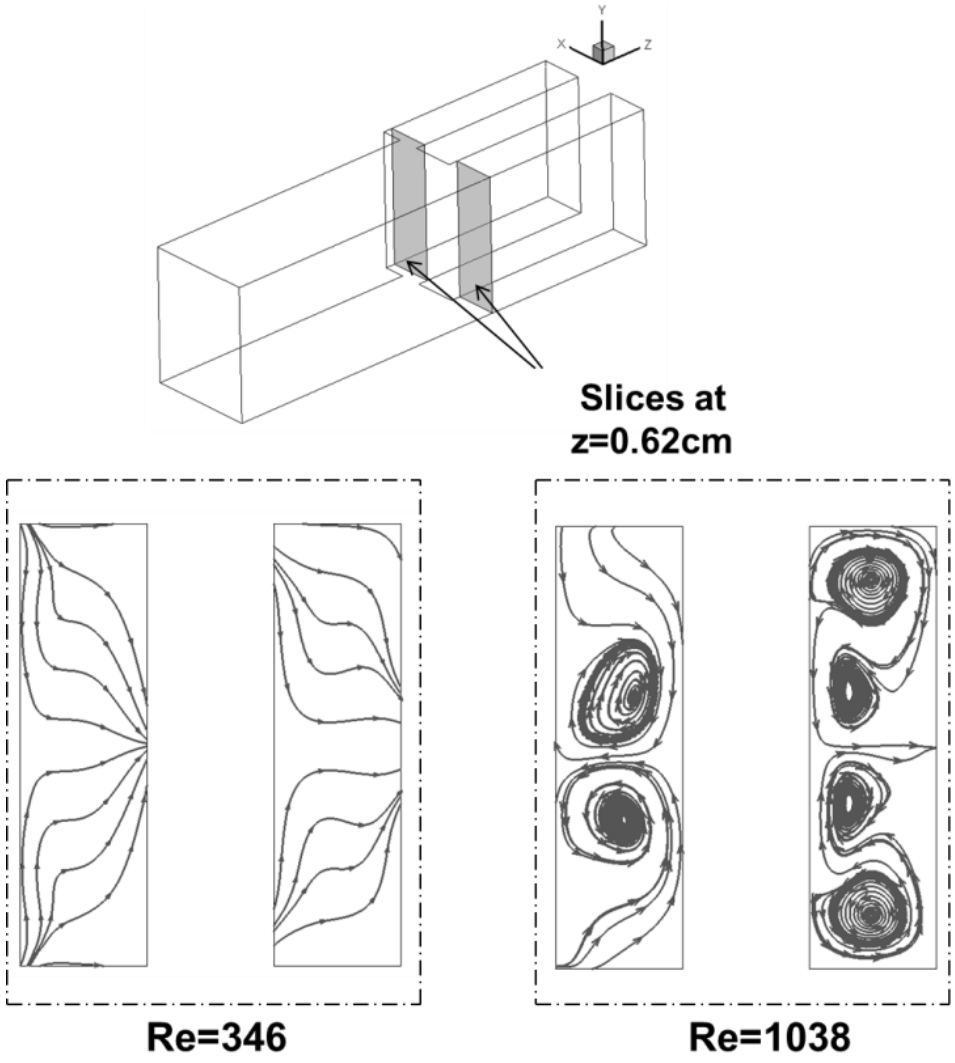

Figure 4.24. Transverse streamlines for different Re number.

The bifurcation microchannel heat sink (Y-shaped channel) provide potential advantages if design properly. Design and optimization of other geometry parameters, such as the total channel numbers, microchannel width, and height will be discussed for heat sink with continuous straight channel in chapter 5. The same approach and parameters can be used to study the heat sink bifurcation channels. In this section, the thermal and fluid

performance prediction for various channel length ratios is presented. Figure 2.25 shows the average thermal resistance versus α, which is defined as:

$$\alpha = \frac{L_1}{L} \tag{4.10}$$

L_1 is the channel length of the first segment, with the channel width $250\mu m$ and channel height $400\mu m$. L is the total length of the heat sink, which is fixed as 1 cm in this study.

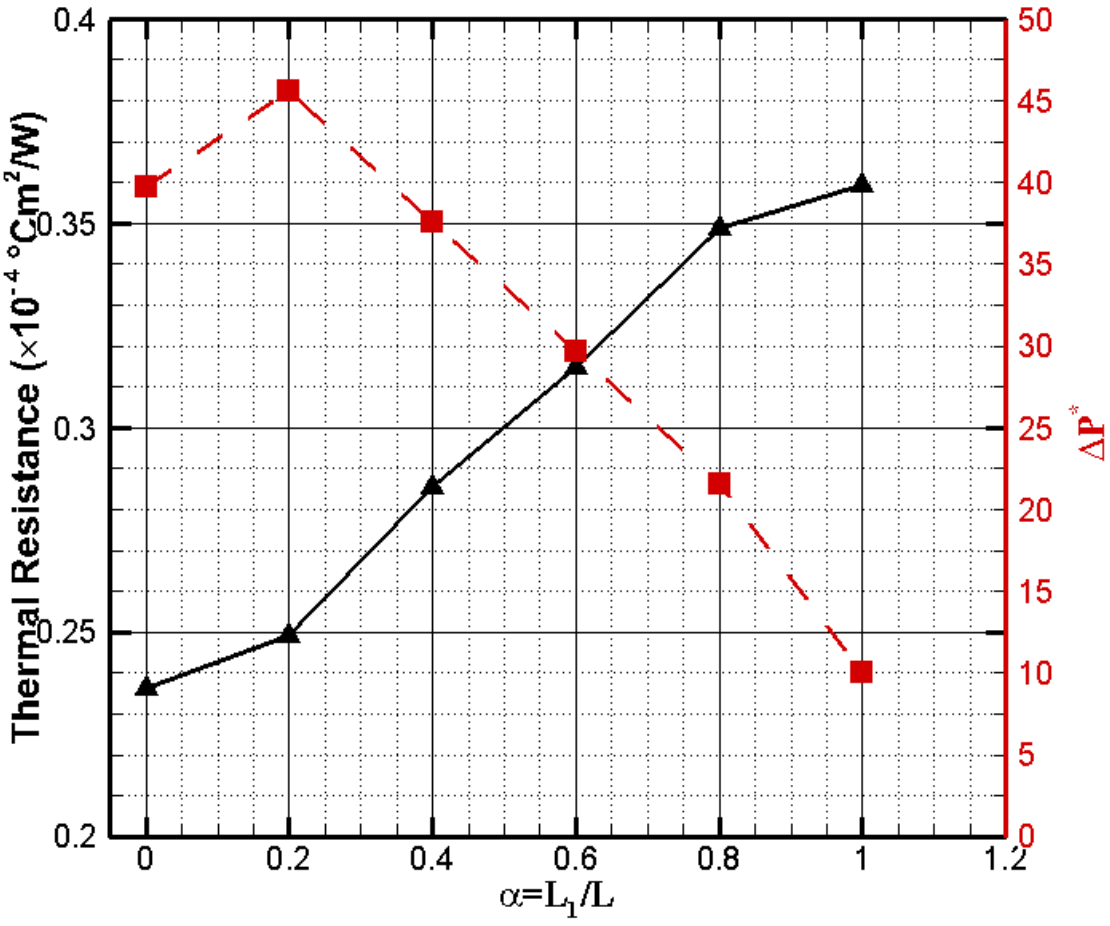

Figure 4.25. Thermal resistance and non-dimensional pressure drop vs. different channel length for Y-shaped channel

The corresponding non-dimensional pressure drop is also shown in Figure 4.25. For a given flow rate (150 ml/min for figure 4.25), having the flow splitting into two branches will change average thermal resistance. When L1 is 0.2 cm, the thermal resistance was increased by 5%, and the pressure drop was also increased by 14%. There are several factors which account for this degradation of the thermal performance. For example, the Reynolds number is too low to allow vortex generation and unsteady flow to occur as shown in figure 4.24. The ratio of the fin thickness to the fin length may have been too low. As the channel length of the first segment kept increasing, the thermal resistance will increase but the pressure drop will decrease.

Chapter 5 Design and Optimization of Microchannel Heat Sinks

The purpose of this chapter is to utilize numerical models built for the heat sink devices in the previous chapter to discuss the design and optimization of multi-microchannel heat sink systems. The parametric modeling techniques will be reviewed in this chapter, based on which the optimization problem will be formulated. Two different configurations of multiple microchannel heat sinks, straight and U-shaped channel designs with liquid flow are investigated for electronic chip cooling. Three responses including thermal resistance, pressure drop, and maximum temperature are parametrically modeled with respect to various design variables including dimensions of channels, total channel numbers, and flow rates. The multi-objective optimization problems, which minimize the thermal resistances and pressure drops simultaneously, are formulated and studied. Some physical constraints in terms of channel height, maximum temperature, and pressure are further investigated. The Pareto frontiers are studied and the trade-off behaviors between the thermal resistances and pressure drops are discussed.

5.1 Formulation of the design problem

The formulation of the design problem is a very important aspect in design and in other engineering activities. The design process depends on the problem statement and so does the evaluation of the design. Therefore, once the requirements of the system are decided, the design obtained must meet all the requirements, and satisfy all the constraints and

limitations. In this study for a cooling system for electronic system, the energy removal rate and maximum temperature of the electronic devices are two of the requirements. In addition, in the design of cooling system for electronic system, the electronic component size, the geometry and dimensions of the board, and number of electronic components on each board, and the distance between two boards may be given, which become the design limitations for the cooling system. Once the design problem is formulated based on the requirements, given parameters, design variables, limitations and constraints, as well as other considerations, the process to obtain an acceptable design is shown in figure 5.1(Jaluria ,1998)

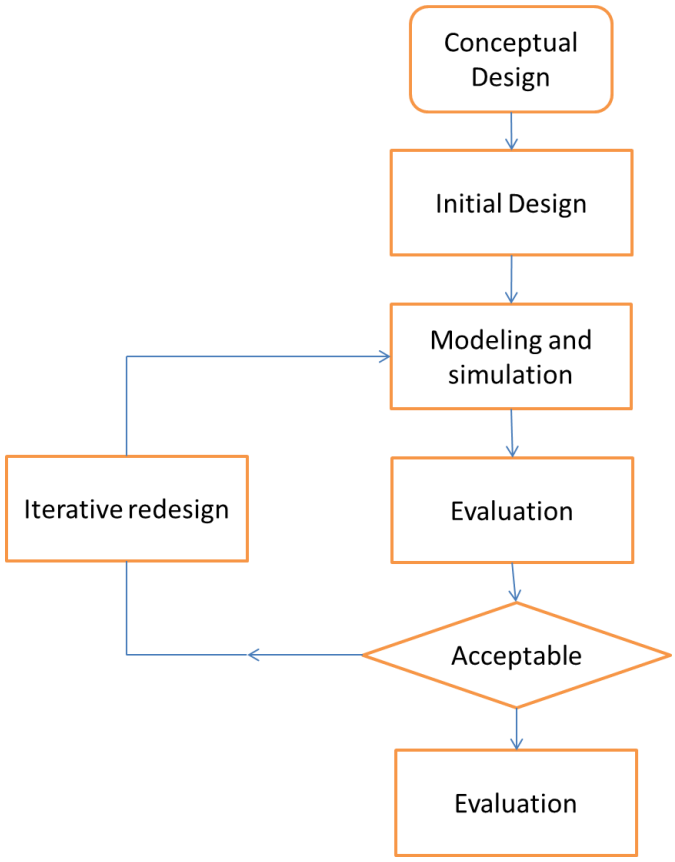

Figure 5.1. Iterative process to obtain an acceptable design.

5.2 Curve Fitting

The physical system design, modeling and simulation were already explained in the previous chapters. The heat transfer and fluid flow with various design parameters for the configurations of straight and U-shaped microchannels will be studied using the validated numerical simulations. The responses of thermal resistance, pressure drop, and maximum temperature will be used to quantitatively represent the performances of the heat sink designs in this chapter. Since results obtained from the numerical simulation are discrete points, curve fitting technique will be used to obtain values at intermediate points where data are not available.

There are two major curve fitting approaches, exact fit and best fit. Exact fit will determine a curve that passed through all the provided data points. Hence, this approach is appropriate for data set that is very accurate. Some of the important exact fitting includes general polynomial, Lagrange interpolation, splines, Newton's dividend-difference polynomial etc. If the data set is large, and/or generating an interpolating curve to pass through every data point is not appropriate, the best fit can be used for such case, to generate a curve that represents the general trend of the data, without necessarily passing through all the points.

The Kriging method applied in this study is one of the exact fittings to predict the responses from experimental or simulation data with minimum error variation estimation. It has been widely utilized for parametric modeling of thermal systems.

The covariance vector which contains M components of the covariance functions is given by:

$$C_x(x, x^S) = \sum_{j=1}^{M} \mathrm{Cov}\left(\boldsymbol{x}, \boldsymbol{x}_j^S\right)\boldsymbol{e}_j \tag{5.1}$$

The approximation function F is defined by the dot product between the coefficient vector w and the covariance vector$C_x(x, x^j)$:

$$F(\boldsymbol{x}) \cong \boldsymbol{w} \cdot C_x(x, x^S) \tag{5.2}$$

where x is the design variable; x_j^S is the j^{th}sampling point; M is the number of sampling points; $\boldsymbol{e}_j$ is the j^{th} normal basis; the notation of dot product is used for the scalar product, the tensor operating on a vector, and the product of tensors.

For each sampling point $\boldsymbol{x}_j^S$, the response $F_j^S\left(\boldsymbol{x}_j^S\right)$ is expressed by

$$F_j^S \boldsymbol{e}_j = w_k \boldsymbol{e}_k \cdot C_{nm}\boldsymbol{e}_m\boldsymbol{e}_n = C_{mn}\boldsymbol{e}_m\boldsymbol{e}_n \cdot w_k\boldsymbol{e}_k \tag{5.3}$$

which is written in the Einstein summation convention. In Equation 6.3, the component of the covariance tensor $\boldsymbol{C}$ is defined as $C_{mn} \equiv \mathrm{Cov}\left(\boldsymbol{x}_m^S, \boldsymbol{x}_n^S\right)$ and $\boldsymbol{C} = \boldsymbol{C}^T$ is given. Therefore, the coefficient vector $\boldsymbol{w}$ can be determined by

$$\boldsymbol{w} = \boldsymbol{C}^{-1}\left(\boldsymbol{x}_1^S, \ldots, \boldsymbol{x}_M^S\right) \cdot \boldsymbol{F}^S\left(\boldsymbol{x}_1^S, \ldots, \boldsymbol{x}_M^S\right) \tag{5.4}$$

where $\boldsymbol{F}^S \equiv F_j^S \boldsymbol{e}_j$. Common Covariance Functions for different Kriging Techniques including Gaussion covariance function, Pseudo-cubic spline, Radial basis function, and etc. In this study, the exponential covariance function is considered:

$$\mathrm{Cov}(\boldsymbol{x}_m, \boldsymbol{x}_n) = 1 - \exp\left(-\left\|\boldsymbol{x}_m, \boldsymbol{x}_n\right\|\right) \tag{5.5}$$

It is noted that there is no approximation error at the sampling points; however, the approximations near the boundaries of design of experiments are less accurate than the interior part. The interior sampling spaces are chosen to be the design spaces for the parametric models in this section and the optimization processes in the next section.

5.3 Straight Channel Model

In the design of straight microchannels, various parameters affect the heat transfer performances, including the experimental parameters of fluid flows and the geometries of heat sinks. In order to simplify the complicated models of microchannel thermal systems, the flow rate $Q\,(\mathrm{m^3 s^{-1}})$ and three geometrical parameters are considered while other parameters are fixed. The first geometrical variable is the dimensionless height H , which is given by

$$H \equiv H_c / (H_c + H_s) \tag{5.6}$$

where $H_c + H_s$ equals the wafer thickness, $550\,\mu\mathrm{m}$. The second one is the dimensionless width W which is defined as

$$W \equiv W_c / (W_c + W_f) \tag{5.7}$$

And the last one is the number of microchannels N. The denominator in Equation 6.7 remains constant when N is fixed.

The validated model shares the same dimension with the experimental device, which corresponding to 56 channel numbers. Instead of modeling with respect to the four design variables, the responses are first parametrically modeled with respect to Q, H and W as baseline models considering constant $N = 56$. Five uniformly distributed sampling points are considered for each design variable, listed in Table 5.1, and only $5 \times 5 \times 5 \times 1 = 125$, simulations are needed. Next, the effects of channel number are studied while fixing the channel height. In our experiment settings, the thickness of photoresist 1518 for the plasma etching of microchannels in the silicon wafer is limited to $\leq 4.6\mu m$; accordingly, the maximum height of microchannel is around 400 μm. Therefore, the responses are also modeled with respect to $Q, N\ and\ W$, under the consideration of $H = 400/550$. Due to the scaling effects in the channel numbers, the five integer points are uniformly sampled in the logarithm of N, listed in Table 5.1, and further $5 \times 1 \times 5 \times 4 = 100$ simulations are considered. The sampling space of N is chosen to ensure the channel hydraulic diameter ranges from 10 to $200\mu m$; following Kandlikar (2003)'s classification of microchannels

For each numerical simulation, three significant responses are studied. Two quantitative measures, including thermal resistance θ and pressure drop ΔP, to represent the thermal performances are chosen as the first two responses. The lower the first two responses are,

the higher the efficiency is and the lower the pumping power requirement is. Since the existence of any hot spot will decrease the reliability of the electronic chip, the maximum temperature T_{max} is considered as the third response and monitored to avoid malfunctions.

Table 5.1. Sampling points for straight channel model.

Sampling points	1	2	3	4	5
Q ($\times 10^{-6}$m^{3}s^{-1})	1.17	1.33	1.50	1.67	1.83
H	100/550	200/550	300/550	400/550	500/550
W	1/6	1/3	1/2	2/3	5/6
N	56	97	167	289	500

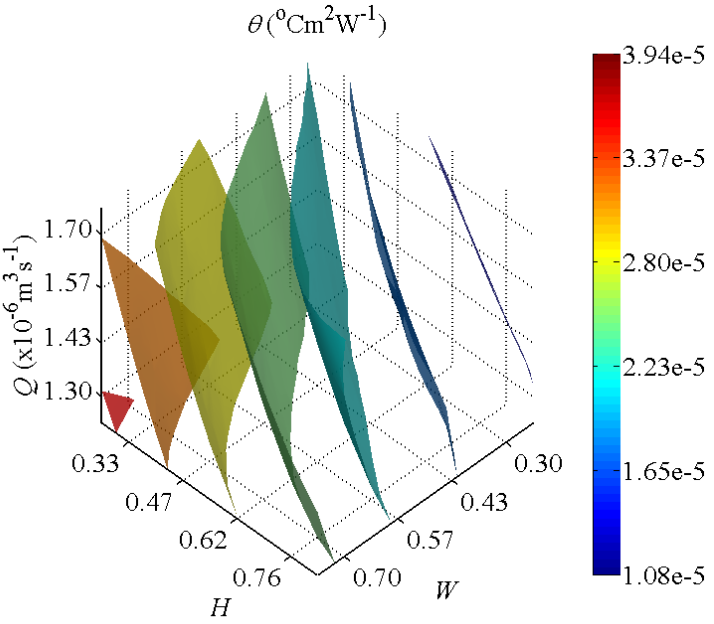

(a) Response with respect to Q, H, and W

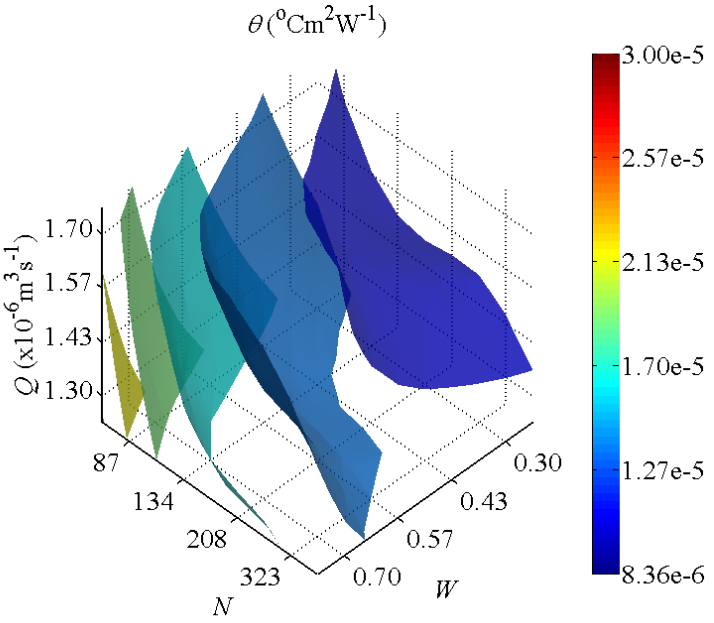

(b) Response with respect to *Q*, *N*, and *W*

Figure 5.2. Thermal resistance isosurfaces for straight channel model.

The first response, thermal resistance θ, is calculated using the heat flux q as the current and $T_{avg} - T_{in}$ as the potential:

$$\theta = \left(T_{\text{avg}} - T_{\text{in}}\right)/q \tag{5.8}$$

where T_{avg} is the average temperature of the heating area; $T_{in} = 20℃$ is the inlet coolant temperature; $q = 2 \times 10^6 wm^{-2}$ remains constant. The response isosurfaces of θ are shown in Figure 5.2. The isosurface (a) is formulated under the constant $N = 56$ while θ varies from 1.08 to 3.94×10^{-5} $℃m^2W^{-1}$. In the given sampling space, θ monotonically decreases when Q and H increase and W decreases. The isosurface (b) considers constant $H = 400/550$. As a result, θ decreases as N increases because of the increment of the total surface area for heat transfer.

The second response, pressure drop ΔP, is parametrically modeled with respect to the previously described variables. Figure 5.3(a) shows the isosurface of ΔP with respect to Q, H, and W while the subfigure (b) presents the one with respect to Q, N, and W. The colorbars are presented in the scale of logarithm of ΔP due to the wide range of responses in the sampling spaces. It is as expected that the pressure drop between the inlet and outlet of fluid decreases when the velocity decreases. The pressure drop decreases when H and W increases; on the other hand, ΔP is smaller when N decreases because of the resultant decrement of inlet velocity. It is noted that the physical behaviors of θ and ΔP both decrease with higher H but conflict with each other associated with $Q,\ N, and\ W$. Hence, the trade-off between θ and ΔP is studied in the formulations of the multi-objective optimization problems in the next section.

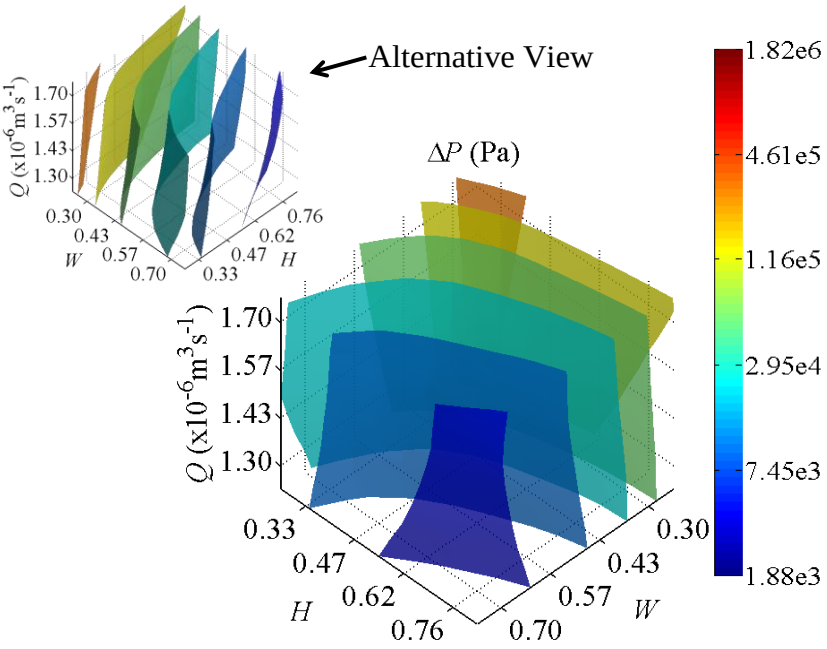

(a) Response with respect to Q, H, and W

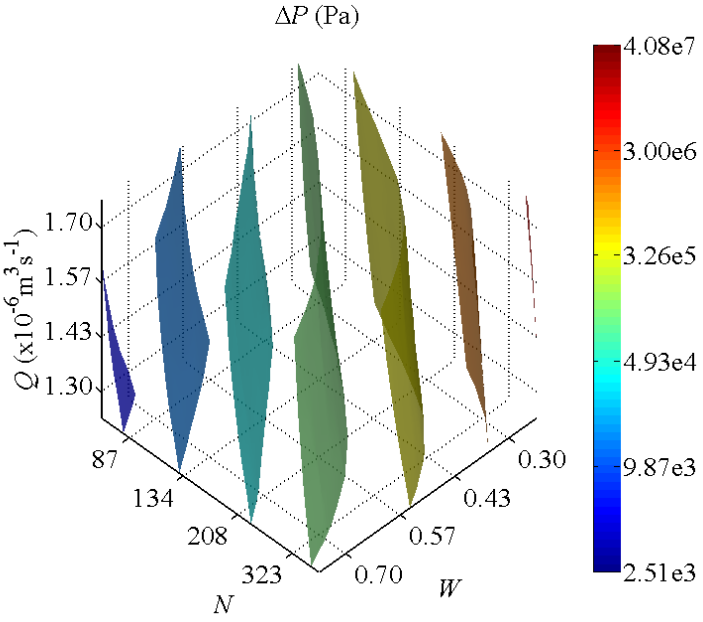

(b) Response with respect to Q, N, and W

Figure 5.3. Pressure drop isosurfaces for straight channel model.

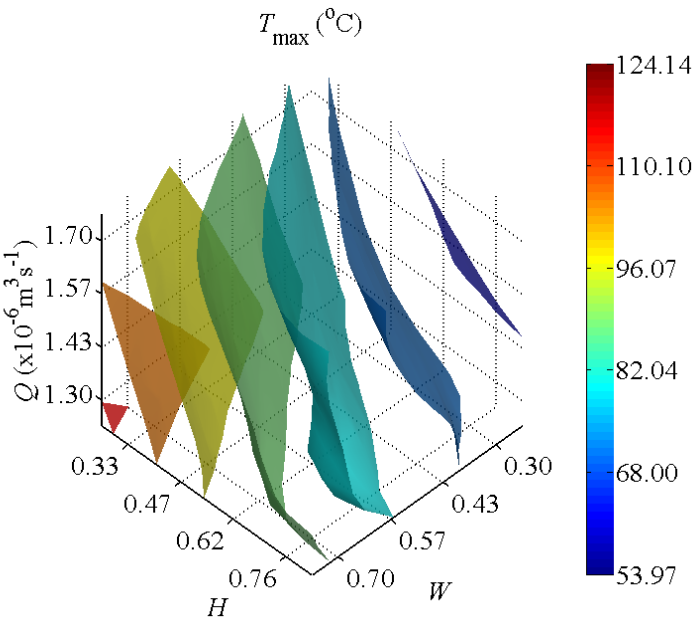

(a) Response with respect to Q, H, and W

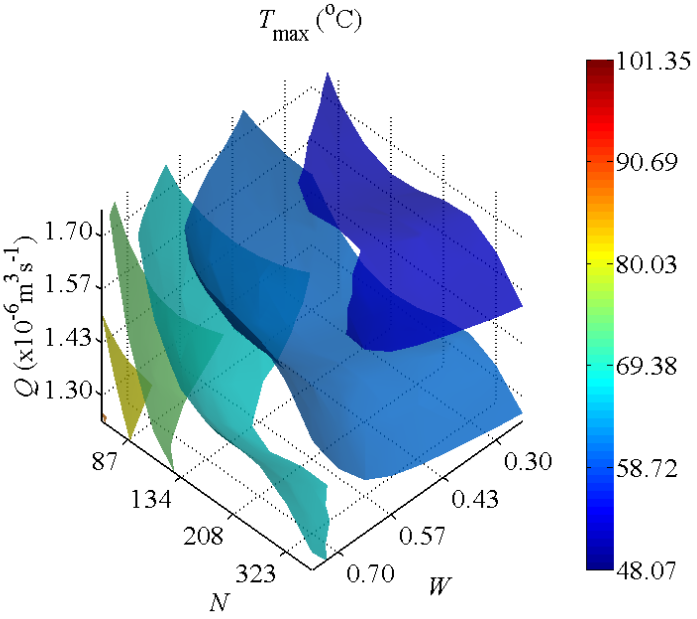

(b)Response with respect to Q, N, and W

Figure 5.4. Maximum temperature isosurfaces for straight channel.

Lastly, the third response, the maximum temperature T_{max}, is shown in Figure 5.4. The behaviors of T_{max} are similar to the thermal resistance: T_{max} is inversely proportional to $Q, H\ and\ N$ but positively proportional to W. The responses of θ represent the average performances of the microchannel heat sink designs while the responses of T_{max} provide the extreme thermal behaviors of the designs. The measure of T_{max} is important because it cannot exceed the allowable level and the hot spots can be avoided. In the next section, the constraints associated with the maximum temperatures are also studied in the optimization formulations.

5.4 U-shape channel model

The second configuration is the U-shaped microchannel design. Similar to the straight microchannel design, the three responses for the U-shaped designs are first parametrically modeled with respect to $Q, H\ and\ W$ considering constant $N = 28$, which is one half of the straight channel number, requiring 125 simulations. The U-shaped microchannel design with $N = 28$ can be compared with the straight design with $N = 56$ because their total surface areas are the same and the channels of inlet and outlet cross sections are identical at the front sides. The sampling points in $Q, H\ and\ W$ for the U-shaped designs, listed in Table 5.2, follow the straight designs; accordingly, the Re varies from 127 to 1003 and the flow remains laminar. Furthermore, the responses are modeled with respect to $Q, N\ and\ W$ with the considerations of constant $H = 400/550$, which needs 100 more simulations. The five uniformly sampling points in the logarithm of N are also listed in table 5.2.

The thermal resistances, shown in figure 5.5, behave differently compared with the straight designs. The measures of θ are very nonlinear with respect to W while the trends against $Q, H\ and\ N$ are similar. The maximum thermal resistance of the U-shaped channel design, 3.68×10^{-5}°Cm^2W^{-1} m in subfigure (a), is lower than the straight channel designs: 3.94×10^{-5}°Cm^2W^{-1} in figure 5.2 (a); however, the minimum measure, 1.65×10^{-5}°Cm^2W^{-1} in Figure 5.5 (a), is higher than the straight designs: 1.08×10^{-5}°Cm^2W^{-1} in Figure 5.2 (a). For U-shaped designs, the flow directions at the curved areas are changed resulting in the formations of flow circulations, which provide better mixing of fluid and enhance heat transfer, but leading to backflows, which are not favorable for cooling. The overall performances of the U-shaped channel designs depend on the dominance of the aspects of circulations and backflows. Similar behaviors can be found in the responses of thermal resistances with respect to $Q, N\ and\ W$.

Table 5.2. Sampling points for U-shaped channel model.

Sampling points	1	2	3	4	5
Q ($\times 10^{-6}$m^{3}s^{-1})	1.17	1.33	1.50	1.67	1.83
H	100/550	200/550	300/550	400/550	500/550
W	1/6	1/3	1/2	2/3	5/6
N	28	48	84	145	250

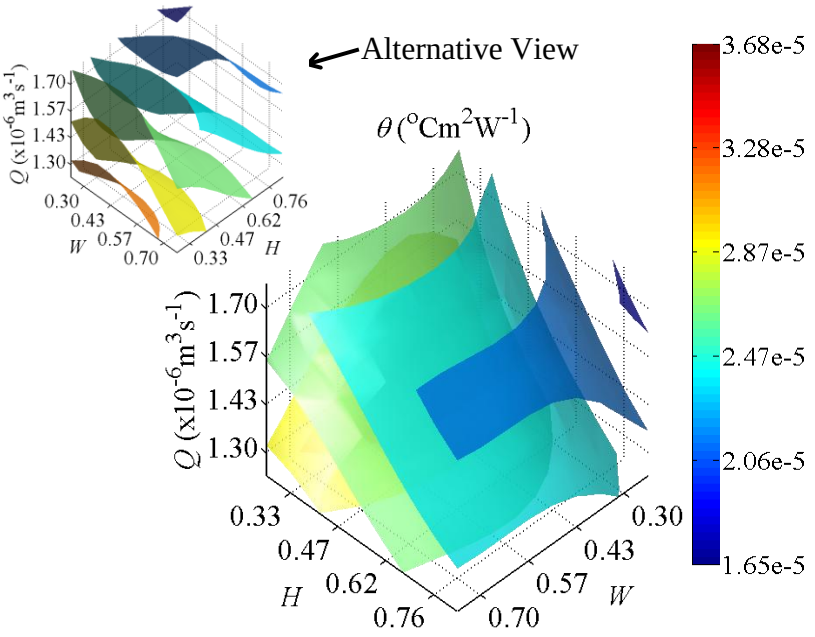

(a) Response with respect to Q, H, and W

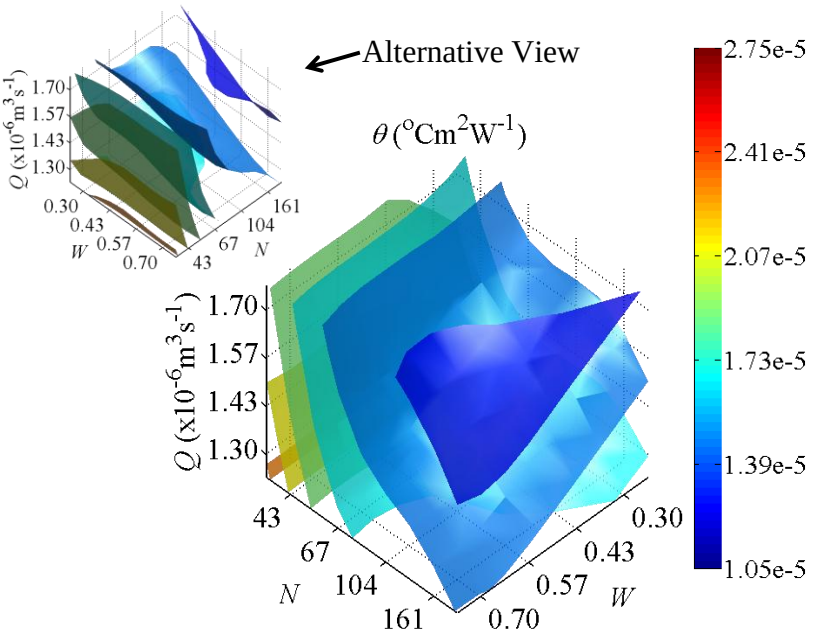

(b) Response with respect to Q, N, and W

Figure 5.5. Thermal resistance isosurfaces for U-shaped channel.

The pressure drops for the U-shaped channel models are shown in Figure 5.6. The alternative views are used for better visualizations of the isosurfaces while the colorbars are used in the scale of double logarithms of ΔP. In the U-shaped designs, the trade-off of enhancement of the thermal resistance is the increment of the pressure drop. Though the trends of pressure drops in the U-shaped designs are similar to the straight designs, the maximum ΔP in Figure 5.6(a), $6.01 \times 10^6 Pa$ is higher than the straight design in Figure 5.3 (a), $1.82 \times 10^6 Pa$; furthermore, the maximum ΔP in Figure 5.6 (b), $1.45 \times 10^8 Pa$, is further greater than the one in Figure 5.3 (b), $4.08 \times 10^7 Pa$. The additional pressure drop for the U-shaped channel is primarily the result of secondary flow which is happened at the bended area.

Lastly, the responses of maximum temperatures, shown in Figure 5.7, are nonlinear associated with W. Furthermore, the maximum T_{max} in the subfigure (a) is around 10ºC higher than the straight channel design in Fig.5.4 (a). Therefore, it is important to find the optimal designs which have allowable maximum temperatures to avoid the malfunctions of the electronic devices.

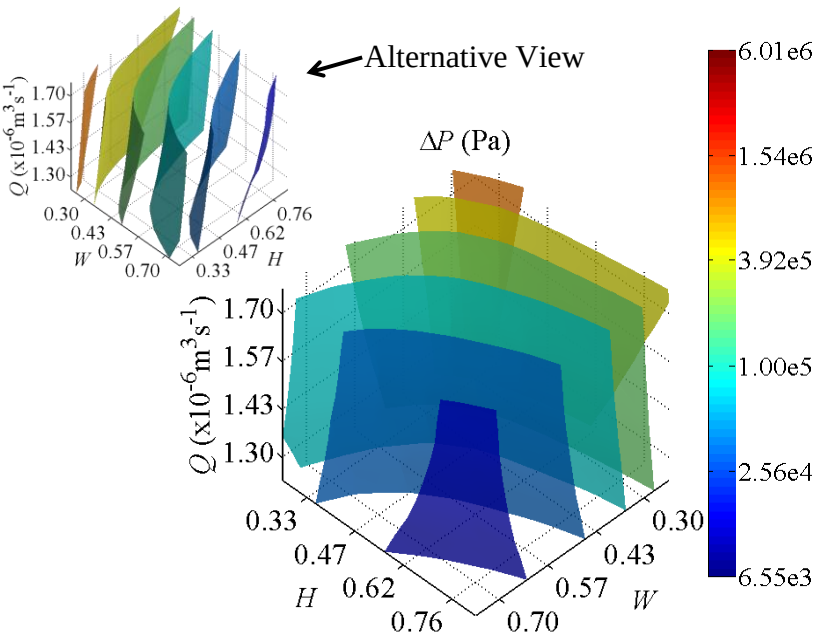

(a) Response with respect to *Q*, *H*, and *W*

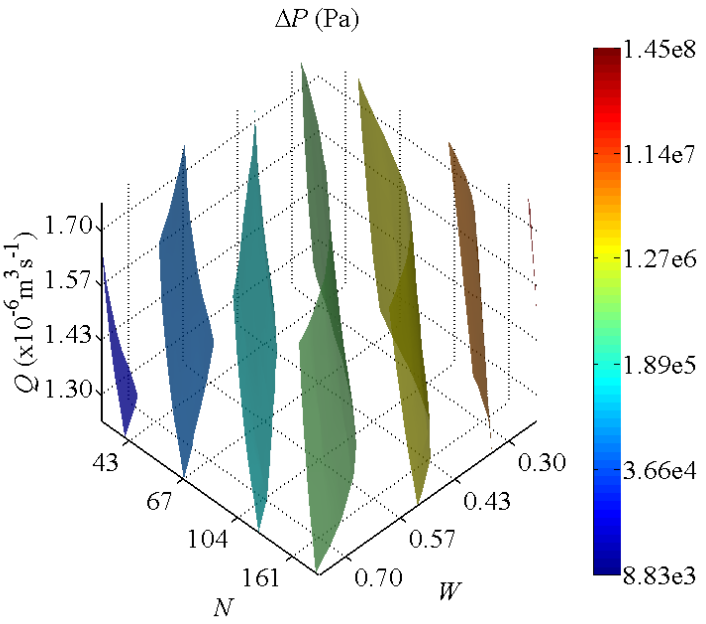

(b) Response with respect to *Q*, *N*, and *W*

Figure 5.6. Pressure drop isosurfaces for U-shaped channel.

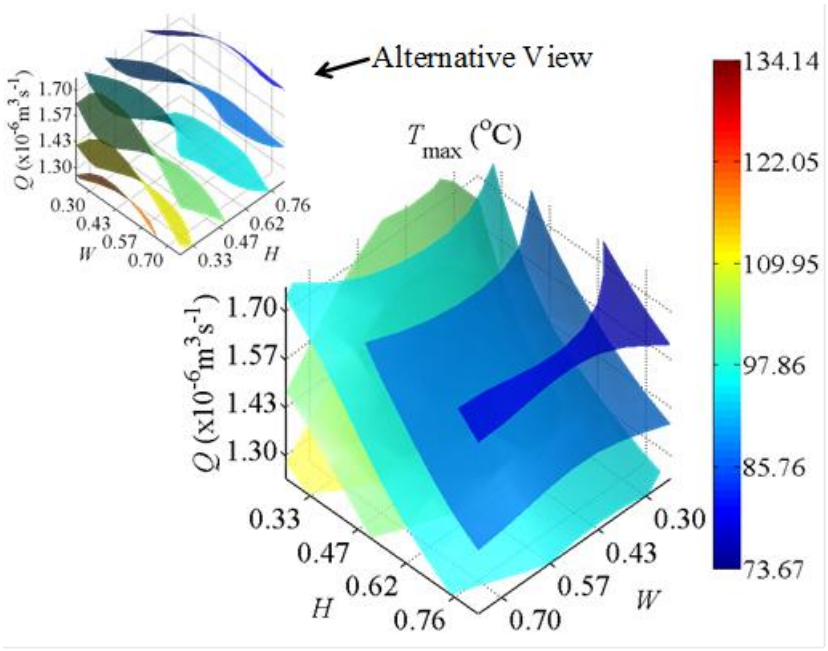

(a) Response with respect to *Q*, *H*, and *W*

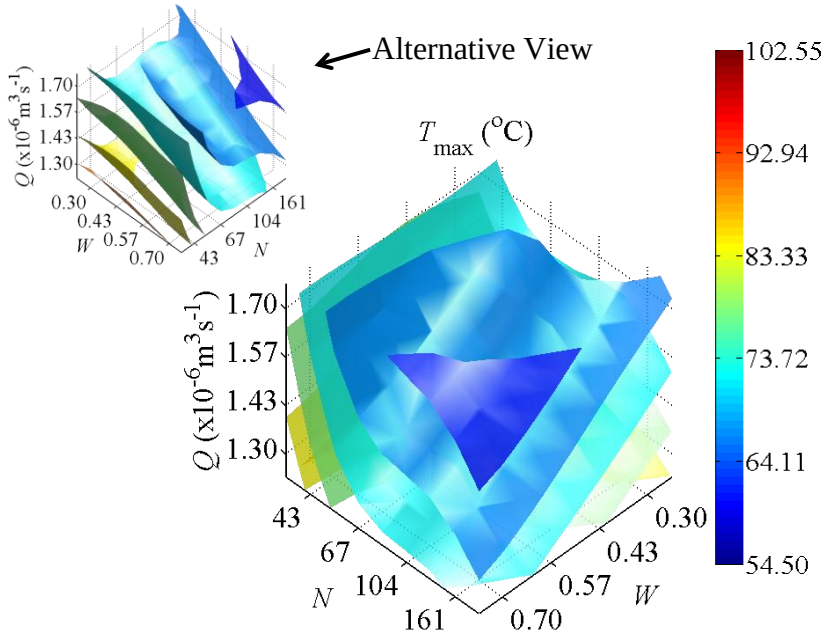

(b) Response with respect to Q, N, and W

Figure 5.7. Max. Temperature isosurfaces for U-shaped channel.

5.5 Optimization problems

In this section, the response surfaces presented previously are used to formulate the optimization problems for both the straight and U-shaped microchannel heat sink designs. In order to get a better thermal performance with a reasonable pumping power requirement, the thermal resistance and pressure drop should be minimized simultaneously. The multi-objective optimization formulations are presented as well as the effects of physical constraints.

5.5.1 Example 1 for straight channel model

The first example is a multi-objective formulation using the weighted-sum method (Deb, 2001):

$$\begin{aligned} \underset{Q,H,W}{Min} \quad & w\theta(Q,H,W)+(1-w)\Delta P(Q,H,W) \\ s.t. \quad & 1.23 \le Q \le 1.77 \ (\times 10^{-6}\ \mathrm{m^3 s^{-1}}) \\ & 0.25 \le H \le 0.84 \\ & 0.23 \le W \le 0.77 \\ & 0 \le w \le 1 \end{aligned} \qquad (5.9)$$

where the thermal resistance and pressure drop, shown in Figures 5.2(a) and 5.3 (a) respectively, are minimized simultaneously with respect to $Q, H\ and\ W$ considering constant $N = 56$. The design variables are bounded in the intervals chosen from the interiors of the sampling spaces. The optimization problem listed in equation 5.9 is solved by the optimization toolbox in Matlab® with various weighting parameters, i.e. $w = 0, 0.025, 0.05, \ldots, 0.975, 1$. The optimal solutions vary with respect to w and the trade-off behavior between both objectives is presented by the Pareto frontier in Figure 5.8. The Pareto frontier not only provides a set of optimal solutions which satisfy the

multi-objective problem in equation 5.9 but also offers more flexibility for design engineers than single-objective formulations.

When $w = 0$, the optimal solution is found at $[Q^*\ H^*\ W^*] = [1.23 \times 10^{-6}\ 0.84\ 0.77]$ and the minimum pressure drop $\Delta P^* = 2350Pa$ is obtained; furthermore, the thermal resistance is $\theta^* = 2.65 \times 10^{-5}°\mathrm{C}m^2W^{-1}$. On the other hand, the minimum thermal resistance $\theta^* = 1.19 \times 10^{-5}°\mathrm{C}m^2W^{-1}$ but higher pressure drop $\Delta P^* = 1.42 \times 10^5 Pa$ are found when $w = 1$; accordingly, the optimal Q^* reaches the upper bound 1.77×10^{-6} and w^* is found at the lower bound 0.23. For each value of , , H^* is found at the upper bound 0.84 indicating that maximum channel height provides the best heat transfer performance.

The problem listed in equation 5.9 is furthermore studied with the considerations of the following physical constraints:

$$\begin{aligned} &g_1 : T_m(Q,H,W) \le 90\ (^{\circ}\mathrm{C}) \\ &g_2 : \Delta P(Q,H,W) \le 2.1\times10^5\ (\mathrm{Pa}) \\ &g_3 : H_c(Q,H,W) \le 400\ (\mu\mathrm{m}) \end{aligned} \qquad (5.10)$$

First of all, the maximum temperature, shown in Figure 5.4 (a), is controlled under 90 ℃ to prevent the malfunction of the electronic chips. According the performance curve of Parker miniature diaphragm pump (Data Sheet of Miniature Diaphragm Pumps from Parker Hannifin Corp), the pressure drop cannot exceed $2.1 \times 10^5\ Pa$ in order to deliver the flow rate and keep the pumping power in the acceptable ranges. As noted previously,

the channel height cannot be larger than $400\mu m$ due to the fabrication limitations. The Pareto frontier under the constraints equation 5.10 is also shown in Figure 5.8.

The physical constraints narrow the design spaces and the optimal solutions are found on the active constraint g_3 for each value of w. Instead of reaching the upper limit of H in the unconstrained problem (Equation 5.9), the optimal $H^* = 0.73$ is found on the third constraint; therefore, the constant $H^* = 0.73$ is considered in the next optimization problem with respect to Q, N, W. Furthermore, more conservative designs with higher thermal resistances and pressures drops are found when considering the physical constraints (Equation 5.10). For example, the optimal objectives are $[\theta^* \ \Delta P^*] = [2.66 \times 10^{-5} \ 3246]$ for $w = 0$ and equal $[1.27 \times 10^{-5} \ 1.65 \times 10^5]$ for $w = 1$. More detailed information about the optimal solutions is listed in table 5.3.

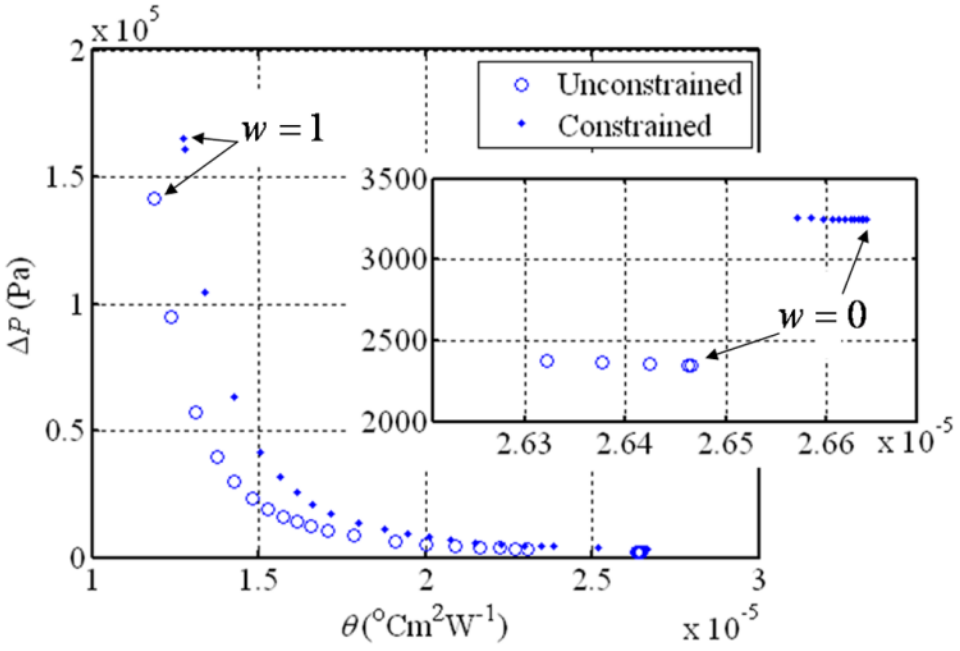

Figure 5.8. Pareto frontiers of example 1.

5.5.2 Example 2 for straight channel model

The second example first presents the unconstrained multi-objective problem investigating the effects of channel numbers:

$$\begin{aligned} \underset{Q,N,W}{Min} \quad & w\theta(Q,N,W)+(1-w)\Delta P(Q,N,W) \\ s.t. \quad & 1.23 \le Q \le 1.77 \ (\times 10^{-6} \ \mathrm{m^3 s^{-1}}) \\ & 70 \le N \le 402 \\ & 0.23 \le W \le 0.77 \\ & 0 \le w \le 1 \end{aligned} \tag{5.11}$$

which considers constant $h = 0.73$. The thermal resistance and pressure drop, shown in Figures 5.2 (b) and 5.3 (b) respectively, are minimized simultaneously following the optimization settings in Example 1. Furthermore, the optimization problem considering the following physical constraints is investigated.

$$\begin{aligned} & g_1 : T_m(Q,N,W) \le 90 \ (^{\circ}\mathrm{C}) \\ & g_2 : \Delta P(Q,N,W) \le 2.1\times 10^5 \ (\mathrm{Pa}) \end{aligned} \tag{5.12}$$

The Pareto frontiers for the unconstrained and constrained problems are shown in Figure 5.9.

As a result, the optimal solutions for both cases are identical when $0 \le w \le 0.75$. For $w \ge 0.75$, the solutions $[Q^* \ N^* \ W^*] = [1.77 \times 10^{-6} \ 149 \ 0.39]$ reach the limit state of g_2 g_2 for the constrained problems and the objectives are $[\theta^*, \Delta P^*] = [1.04 \times 10^{-5} \ 2.10 \times 10^5]$. On the other hand, θ^* is as low as 8.89×10^{-6} at $w = 0.75$ for the unconstrained formulation; in this case, the channel number reaches the upper limit, i.e.

$N = 402$. It is as expected that maximum channel number produces largest surface area for heat transfer resulting lowest thermal resistance; however, the highest pressure drop $\Delta P^* = 9.91 \times 10^6$ is found. More detailed information about the optimal solutions is listed in Table 5.4

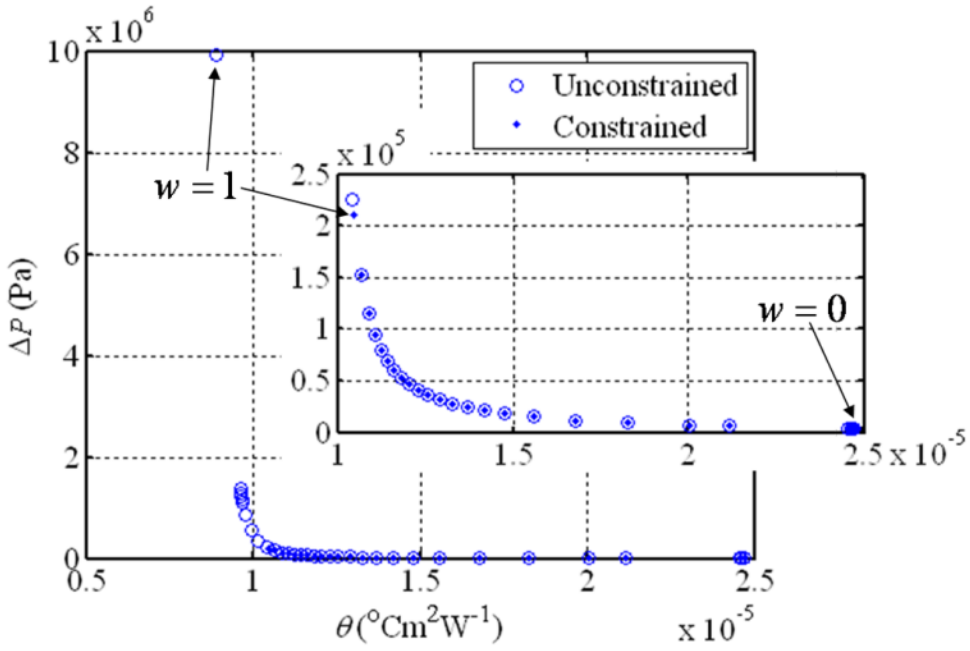

Figure 5.9. Pareto frontiers of example 2.

5.5.3 Example 3 for U-shape channel model

For the U-shaped microchannel heat sink designs, the multi-objective formulations follow the Equation 5.9 and physical constraints in Equation 5.10 are also studied. The optimization settings follow the Example 1. The Pareto frontiers for both unconstrained and constrained formulations are shown in Figure 5.10. The detailed information of the optimal solutions is given in Table 5.5. Similar to Example 1, the design spaces become smaller and more conservative designs are found when physical constraints are

considered. For both constrained and unconstrained formulations, the optimal thermal resistances of the U-shaped designs, enhanced by the circulations of fluids in the curved geometries of microchannels, are lower than the straight designs when $w < 0.45$. However, both the thermal resistances and pressures drops in the U-shaped designs are relatively higher than the straight designs in the other cases.

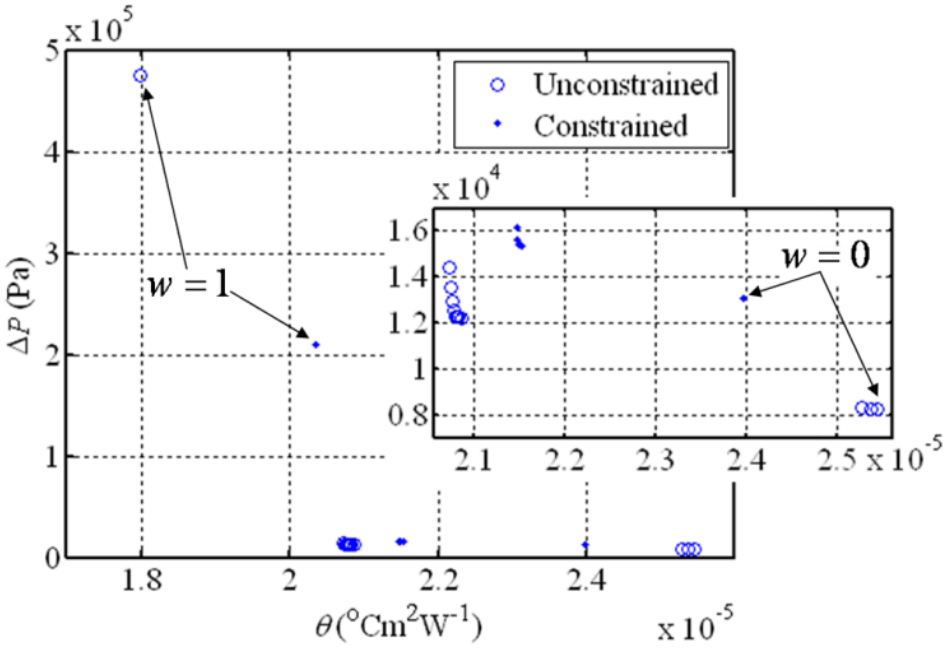

Figure 5.10. Pareto frontiers of example 3.

5.5.4 Example 4 for U-shaped Channel model

In order to study the effects of channel numbers, the multi-objective formulations in equation 5.11 with and without the physical constraints (equation 5.12) are investigated while N is bounded by [35, 201] for the U-shaped designs. Following the same optimization settings, the resultant Pareto frontiers and optimal solutions are shown in Figure 5.11 and Table 5.6 respectively. In the cases of$0.15 \leq w \leq 0.7$, identical results

are found for both unconstrained and constrained problems; otherwise, more conservative designs are found in the constrained formulations. Compared with the straight microchannel designs, lower thermal resistances in the U-shaped designs are found at $w \leq 0.4$ for both unconstrained and constrained formulations. Furthermore, the pressure drops in U-shaped designs are lower than straight designs when $w \geq 0.875$ for unconstrained formulations and $w \geq 0.775$ for constrained ones. The optimal results presented in this paper provide a comprehensive guideline for the selections of the geometries of microchannels, the experimental parameters, and the weighting coefficients in the optimization formulations.

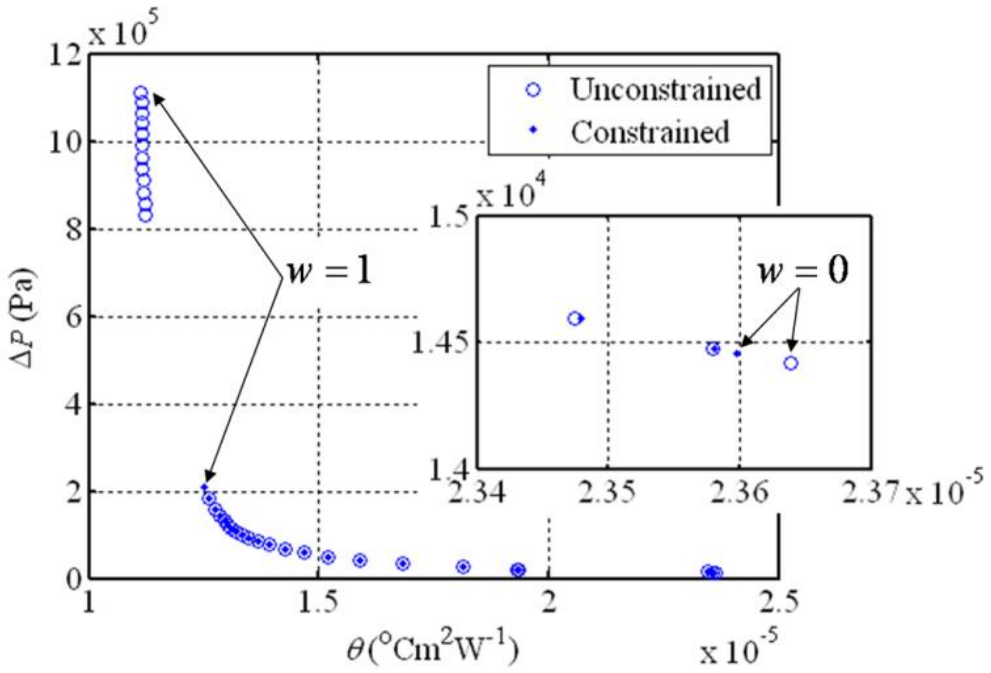

Figure 5.11. Pareto frontiers of example 4.

Two different configurations of multiple microchannel heat sinks, including the straight and U-shaped channel designs, have been studied. The models have been designed with

respect to the experimental and geometrical parameters and studied by the numerical simulations. The simulation data have been validated by comparing with the experimental results. Various responses to represent the influences of flow rates and geometrical variables to the heat transfer performances have been parametrically modeled and studied. For both straight and U-shaped microchannel designs, the optimization problems have been formulated to minimize the thermal resistances and pressure drops simultaneously. The Pareto frontiers have been found and presented to demonstrate the trade-off behaviors between the multiple objective functions. Furthermore, the optimization problems have been studied with the considerations of the physical constraints. In the constrained formulations, the feasible design spaces were narrowed and more conservative optimal solutions have been found.

Table 5.3. Optimal solutions in example 1.

w	Unconstrained	
	$[Q^*\ H^*\ W^*]$	$[\theta^*, \Delta P^*]$
0	$[1.23 \times 10^{-6}\ 0.84\ 0.77]$	$[2.65 \times 10^{-5}\ 2.35 \times 10^{3}]$
0.25	$[1.24 \times 10^{-6}\ 0.84\ 0.77]$	$[2.64 \times 10^{-5}\ 2.36 \times 10^{3}]$
0.5	$[1.76 \times 10^{-6}\ 0.84\ 0.55]$	$[1.78 \times 10^{-5}\ 8.78 \times 10^{3}]$
0.75	$[1.77 \times 10^{-6}\ 0.84\ 0.27]$	$[1.24 \times 10^{-5}\ 9.48 \times 10^{4}]$
1	$[1.77 \times 10^{-6}\ 0.84\ 0.23]$	$[1.19 \times 10^{-5}\ 1.42 \times 10^{5}]$

w	Constrained	
	$[Q^*\ H^*\ W^*]$	$[\theta^*, \Delta P^*, T_{max}]$
0	$[1.29 \times 10^{-6}\ 0.73\ 0.76]$	$[2.66 \times 10^{-5}\ 3.25 \times 10^{3}\ 90.0]$
0.25	$[1.28 \times 10^{-6}\ 0.73\ 0.75]$	$[2.66 \times 10^{-5}\ \ 3.25 \times 10^{3}\ 90.0]$
0.5	$[1.77 \times 10^{-6}\ 0.73\ 0.59]$	$[1.95 \times 10^{-5}\ 9.17 \times 10^{3}\ 73.1]$
0.75	$[1.77 \times 10^{-6}\ 0.73\ 0.24]$	$[1.77 \times 10^{-6}\ 1.61 \times 10^{5}\ 58.0]$
1	$[1.77 \times 10^{-6}\ 0.73\ 0.23]$	$[1.27 \times 10^{-5}\ 1.65 \times 10^{5}\ 57.9]$

Table 5.4 Optimal solutions in example 2

w	Unconstrained	
	$[Q^*\ N^*\ W^*]$	$[\theta^*, \Delta P^*]$
0	$[1.23 \times 10^{-6}70\ 0.77]$	$[2.47 \times 10^{-5}\ 4.08 \times 10^{3}]$
0.25	$[1.25 \times 10^{-6}\ 70\ 0.77]$	$[2.46 \times 10^{-5}\ 4.114 \times 10^{3}]$
0.5	$[1.76 \times 10^{-6}\ 117\ 0.63]$	$[1.29 \times 10^{-5}\ 3.15 \times 10^{4}]$
0.75	$[1.77 \times 10^{-6}\ 149\ 0.43]$	$[1.07 \times 10^{-5}1.53 \times 10^{5}]$
1	$[1.77 \times 10^{-6}\ 402\ 0.23]$	$[8.89 \times 10^{-5}\ 9.91 \times 10^{6}]$

w	Constrained	
	$[Q^*\ N^*\ W^*]$	$[\theta^*, \Delta P^*, T_{max}]$
0	$[1.23 \times 10^{-6}\ 70\ 0.77]$	$[2.47 \times 10^{-5}\ 4.08 \times 10^{3}\ 88.8]$
0.25	$[1.25 \times 10^{-6}\ 70\ 0.77]$	$[2.46 \times 10^{-5}\ \ 4.14 \times 10^{3}\ 88.2]$
0.5	$[1.77 \times 10^{-6}\ 117\ 0.63]$	$[1.29 \times 10^{-5}\ 3.15 \times 10^{4}\ 58.4]$
0.75	$[1.77 \times 10^{-6}\ 149\ 0.43]$	$[1.07 \times 10^{-5}\ 1.53 \times 10^{5}\ 54.0]$
1	$[1.77 \times 10^{-6}\ 149\ 0.39]$	$[1.07 \times 10^{-5}\ 2.10 \times 10^{5}\ 53.6]$

Table 5.5. Optimal solutions in example 3.

w	Unconstrained	
	$[Q^*\ H^*\ W^*]$	$[\theta^*, \Delta P^*]$
0	$[1.23 \times 10^{-6}\ 0.84\ 0.77]$	$[2.54 \times 10^{-5}\ 8.22 \times 10^{3}]$
0.25	$[1.76 \times 10^{-6}\ 0.84\ 0.77]$	$[2.08 \times 10^{-5}\ 1.22 \times 10^{4}]$
0.5	$[1.77 \times 10^{-6}\ 0.84\ 0.77]$	$[2.08 \times 10^{-5}\ 1.23 \times 10^{4}]$
0.75	$[1.77 \times 10^{-6}\ 0.84\ 0.77]$	$[2.08 \times 10^{-5}\ 1.24 \times 10^{4}]$
1	$[1.77 \times 10^{-6}\ 0.84\ 0.23]$	$[1.80 \times 10^{-5}\ 4.76 \times 10^{5}]$

w	Constrained	
	$[Q^*\ H^*\ W^*]$	$[\theta^*, \Delta P^*, T_{max}]$
0	$[1.45 \times 10^{-6}\ 0.73\ 0.77]$	$[2.40 \times 10^{-5}\ 1.31 \times 10^{4}\ 90.0]$
0.25	$[1.76 \times 10^{-6}\ 0.73\ 0.77]$	$[2.15 \times 10^{-5}\ \ 1.54 \times 10^{4}\ 82.3]$
0.5	$[1.77 \times 10^{-6}\ 0.73\ 0.77]$	$[2.15 \times 10^{-5}\ 1.54 \times 10^{4}\ 82.3]$
0.75	$[1.77 \times 10^{-6}\ 0.73\ 0.77$	$[2.15 \times 10^{-6}\ 1.54 \times 10^{4}\ 82.3]$
1	$[1.77 \times 10^{-6}\ 0.73\ 0.31$	$[2.03 \times 10^{-5}\ 2.10 \times 10^{5}\ 81.0]$

Table 5.6. Optimal solutions in example 4.

w	Unconstrained	
	$[Q^*\ N^*\ W^*]$	$[\theta^*, \Delta P^*]$
0	$[1.23 \times 10^{-6}35\ 0.77]$	$[2.36 \times 10^{-5}\ 1.44 \times 10^{4}]$
0.25	$[1.77 \times 10^{-6}\ 35\ 0.77]$	$[1.93 \times 10^{-5}\ 2.15 \times 10^{4}]$
0.5	$[1.77 \times 10^{-6}\ 75\ 0.77]$	$[1.35 \times 10^{-5}\ 9.36 \times 10^{4}]$
0.75	$[1.77 \times 10^{-6}\ 201\ 0.73]$	$[1.12 \times 10^{-5}8.57 \times 10^{5}]$
1	$[1.77 \times 10^{-6}\ 201\ 0.67]$	$[1.11 \times 10^{-5}\ 1.11 \times 10^{6}]$

w	Constrained	
	$[Q^*\ N^*\ W^*]$	$[\theta^*, \Delta P^*, T_{max}]$
0	$[1.24 \times 10^{-6}\ 35\ 0.77]$	$[2.36 \times 10^{-5}\ 1.45 \times 10^{4}\ 90]$
0.25	$[1.77 \times 10^{-6}\ 35\ 0.77]$	$[1.93 \times 10^{-5}\ \ 2.15 \times 10^{4}\ 76]$
0.5	$[1.77 \times 10^{-6}\ 75\ 0.77]$	$[1.35 \times 10^{-5}\ 9.36 \times 10^{4}\ 61.1]$
0.75	$[1.77 \times 10^{-6}\ 116\ 0.75]$	$[1.25 \times 10^{-5}\ 2.10 \times 10^{5}\ 60.0$
1	$[1.77 \times 10^{-6}\ 116\ 0.75]$	$[1.25 \times 10^{-5}\ 2.10 \times 10^{5}\ 60.0]$

It has been shown that the optimal experimental and geometrical parameters for the minimum thermal resistances and pressure drops vary with respect to the preferences from the designers. The detailed investigations presented in this paper not only provide a comprehensive understanding of the influences of the design variables to the heat transfer performances in both the straight and U-shaped microchannel models but also offer a useful guideline for the selections of design parameters in the heat sink designs. Furthermore, the developed strategies are useful for not only understanding the fundamental heat transfer and fluid flow characteristics in the multiple microchannel designs but also providing quantitative inputs for the processes of design and optimization. Accordingly, the designs of multiple microchannel heat transfer systems can be accomplished.

Chapter 6 Data Center Thermal Management

The purpose of this chapter is to build a numerical model to investigate the cooling system for data centers. The temperature distribution and flow distribution at both steady state and transient state will be studied. The objective of the model is to control the temperature in the data center at an allowable range, as well as reduce the energy and cost for the cooling system.

6.1 Computer room air conditioning units (CRAC) and cooling system

Microchips with high heat dissipation results in significant cooling challenges at the data center facility level. The power density is in a range of 2-20kW/rack today. In a typical data center, the power consumption on cooling and thermal management is as much as 54% of the total power consumption. For a 10 MW facility, this would lead to a cost of up to $3.9M annually assuming an energy price of $0.1 per kWh. Therefore, the thermal management is one of the most important and challenging tasks for data center and computer room managers.

There are two classes of thermal management policies for data centers: those that manage temperature under normal operation and those that manage thermal emergencies. The objective of normal operation thermal management is to reduce cooling cost. On the other

hand, a large increase in load that causes temperatures to rise quickly can be considered a thermal emergency. The main objective for managing thermal emergencies is to control temperatures while avoiding unnecessary performance degradation. In this chapter, both thermal management policies will be studied.

The air distribution within a data center has a major impact on the temperature distribution of the equipment located in the rooms. In some data centers, the cold air enters the data center from the ceiling through diffusers, and exits the room via vents on the sides of the room. Most of the data centers use the hot aisle/cold aisle layout, which is designed to supply cold air through a raise floor. CRACs are used to pump the cooling air into the plenum underneath the data center room. There are perforated tiles on the floor that are used to replace solid tiles and allow air to enter the above floor space. The aisles with perforated tiles are cold aisles. The aisles without the cold air delivery are hot aisles.

The raised floor data center is popular because of its flexibility. The floor tiles are designed to be removable. If the layout arrangement of the server racks is changed, the corresponding perforated tile locations can be changed so that the cold air can be delivered to where the hot rack is located.

6.2 Model setup

6.2.1 The physical model layout

A physical model based on the configuration of actual data center including the under floor plenum, server rack, CRACs, perforated tiles is created as shown in figure 6.1. The cooling system is a typical today's cooling system. The data center model consists of 6 CRAC units and 16 electronic racks (each 1m×1m×2m tall). The overall dimension of the data center is 7m× 8m×3m. The under-floor plenum height is 0.5m. Each rack is assumed to contain 24 servers, and the dimension of each server is 0.43m× 0.22m×0.046m (17in×8.5in×1.8in). Each rack has a power of 10 kW when fully utilized.

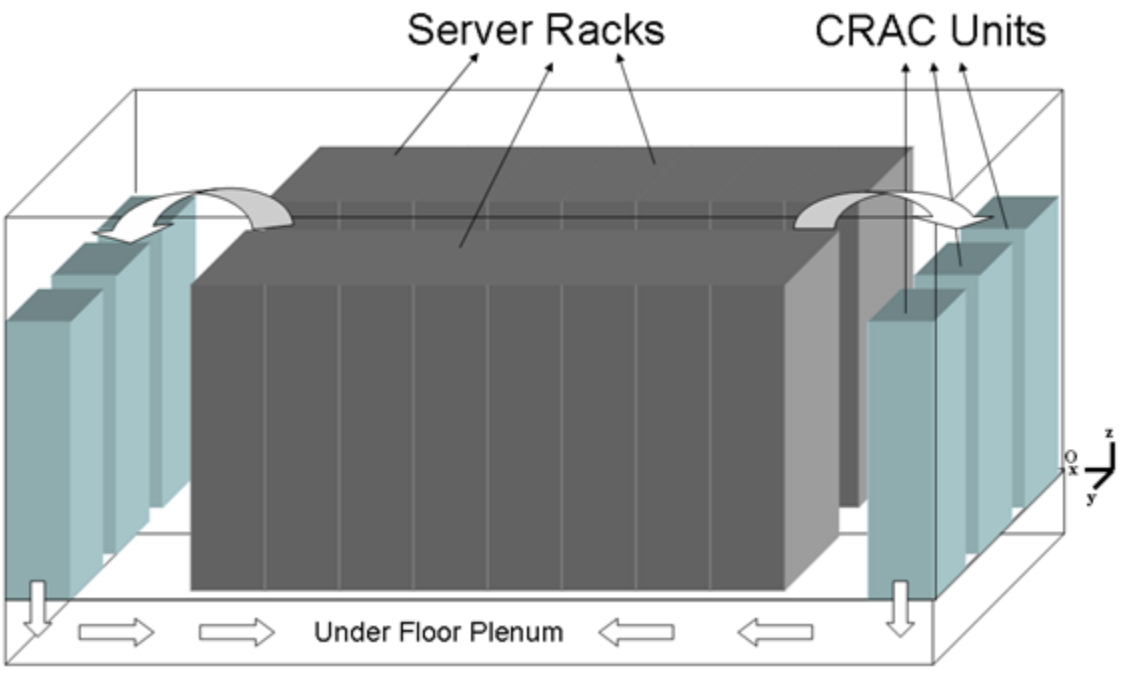

(a) 3D sketch of the Data Center

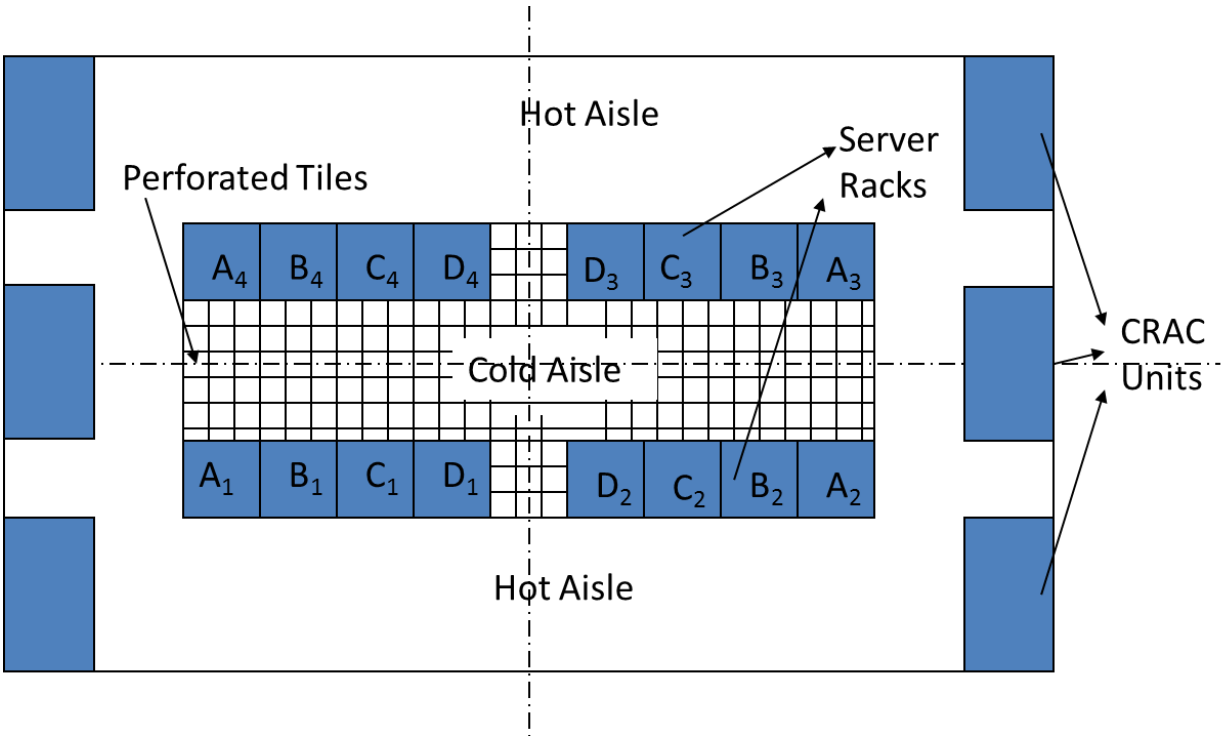

(b) Top View of the CFD model

Figure 6.1. Schematic drawing of the CFD data center model.

The CRAC units discharge cold air in the under floor plenum. The air is delivered to the raised floor through perforated tiles, and then the hot air returns to the CRAC units. The entire data center is symmetric so one fourth of the room was selected as the computational domain to reduce the simulation overheads. Different utilization levels are modeled by turning on/off the heat source within the server racks.

6.2.2 Governing equations

A turbulent flow instantaneously satisfies the Navier-Stokes equations shown as follows (Kundu and Cohen, 2002):

$$\frac{\partial \tilde{u}_i}{\partial x_i} = 0 \tag{6.1}$$

$$\frac{\partial \tilde{u}_i}{\partial t} + \tilde{u}_j \frac{\partial \tilde{u}_i}{\partial x_i} = -\frac{\partial \tilde{p}}{\partial x_i} - g[1-\alpha(\tilde{T}-T_0)]\delta_{i3} + \nu \frac{\partial^2 \tilde{u}_i}{\partial x_j \partial x_j} \tag{6.2}$$

$$\frac{\partial \tilde{T}}{\partial t} + \tilde{u}_j \frac{\partial \tilde{T}}{\partial x_i} = \kappa \frac{\partial^2 \tilde{T}}{\partial x_j \partial x_j} \tag{6.3}$$

However, it is a challenge to predict the flow in detail since there are different scales to be resolved. The averaged equations are used to find to mean velocity and temperature of a turbulence flow. The simplest "complete models" of turbulence are the two equation models in which the solution of two separate transport equations allows the turbulent velocity and length scales to be independently determined.

The turbulence kinetic energy κ and its rate of dissipation ε are obtained from the following transport equations:

$$\frac{\partial}{\partial t}(\rho\kappa) + \frac{\partial}{\partial x_i}(\rho\kappa u_i) = \frac{\partial}{\partial x_j}[(\mu + \frac{\mu_t}{\sigma_k})\frac{\partial \kappa}{\partial x_j}] + G_k + G_b - \rho\varepsilon - Y_M \tag{6.4}$$

and

$$\frac{\partial}{\partial t}(\rho\varepsilon) + \frac{\partial}{\partial x_i}(\rho\varepsilon u_i) = \frac{\partial}{\partial x_j}[(\mu + \frac{\mu_t}{\sigma_\varepsilon})\frac{\partial \varepsilon}{\partial x_j}] + C_{1\varepsilon}\frac{\varepsilon}{k}(G_k + C_{3\varepsilon}G_b) - C_{2\varepsilon}\rho\frac{\varepsilon^2}{\kappa} \tag{6.5}$$

where G_k represents the generation of turbulence kinetic energy due to the mean velocity gradient, calculated as:

$$G_k = -\rho \overline{u_i' u_j'} \frac{\partial u_j}{\partial x_j} \tag{6.6}$$

G_b is turbulence kinetic energy due to buoyancy. For ideal gas calculated as described:

$$G_b = -g_i \frac{\mu}{\rho \Pr_t} \frac{\partial \rho}{\partial x_i} \tag{6.7}$$

Y_M represents the contribution of the fluctuating dilatation in compressible turbulence to the overall dissipation rate:

$$Y_M = 2\rho\varepsilon \frac{\kappa}{a^2} \tag{6.8}$$

In this study, the air is treated as incompressible flow, so this term is zero.

$C_{1\varepsilon}$, $C_{2\varepsilon}$, $C_{3\varepsilon}$ are constants, σ_k and μ_t are the turbulent Prandtl numbers for κ and ε, respectively. The corresponding values are 1.44, 1.92, 0.09, 1.0 and 1.3. Ansys Fluent 12.0 turbulent k-epsilon model was applied with standard wall functions was applied to solve the equations listed above. The server rack is simplified as porous media with heat source. The perforated tiles were treated as one dimensional porous jump boundary condition. The pressure drop across the perforated tiles is expressed as:

$$\Delta p = K(0.5\rho V^2) \tag{6.9}$$

where V is the velocity entering the perforated tile, and K is the flow resistance factor.

It was calculated by the equations given by Idelchik (1986):

$$K = \frac{1}{F_p}(1 + 0.5(1 - F_p)^{0.75} + 1.414(1 - F_p)^{0.375}) \quad (6.10)$$

where F_p is the fractional open area of the perforated tile.

The effects of the inlet temperature and flow rate were studied. Note that we simulated a relatively small data center to keep simulation times reasonable. When scaling to larger data centers, efficiency of the cooling system can be improved in various ways, possibly leading to decreased energy consumption in the order of 30% (NREL 2010).

The grid dependence was first studied. The physical model showed in figure 6.1 was meshed with different interval sizes 0.1m, 0.08m and 0.05m, respectively. The results showed that the temperature and air flow distribution don't change when the interval size is smaller than 0.08m. Thus, the model with 0.08 interval size, which generated 162,409 structural hex mesh elements, was applied for all the following simulations.

6.3 CFD/HF modeling results

The data center utilization may vary on a need base. It will not be 100% all the time. In this study, the temperature and air flow at utilization of 25%, 50%, 75% and 100% are investigated. When the utilization is 25% for the entire data center room, one of the racks need to be in operation. Since the computation domain is a quarter of the entire room, Rack A_1 in operation means A_i (i=1, 2, 3, 4) are all in operation (figure 6.1).

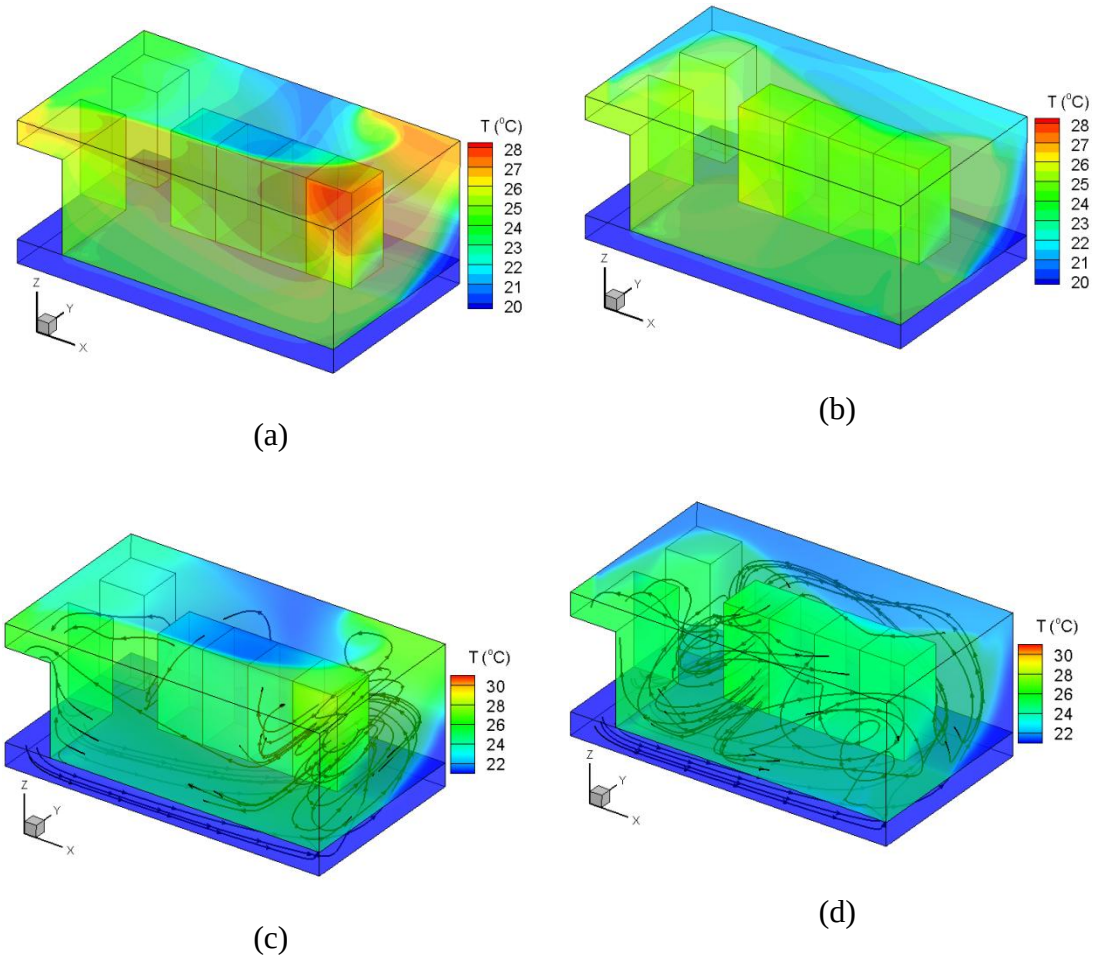

Figure 6.2. Temperature distribution in the data center with 25% utilization. (a) D_i racks are operating (b) $A_i$racks are operating (c) Streamlines with D_i operating (d) Streamlines with A_i operating.

Figure 6.2 shows the temperature distribution in the data center room with different racks in operation. The CRAC inlet temperature is 20 ºC, and the flow rate for both cases is 3350CFM. When rack D is in operation (figure 6.2a), the maximum room temperature is

higher than the case that has the same utilization but with rack A in operation. This is because rack D is further away from the air outlet, the hot air needs to travel longer time in the room. Moreover, more vortexes are generated as it goes toward the outlet as shown in figure 6.2c.

On the other hand, if rack A is operating, the hot air travels a shorter distance and the CRAC system runs more efficiently, and the temperature distribution in the room ismore uniformly distributed. Hence, in the following study, rack A will be operating when the utilization is 25%.

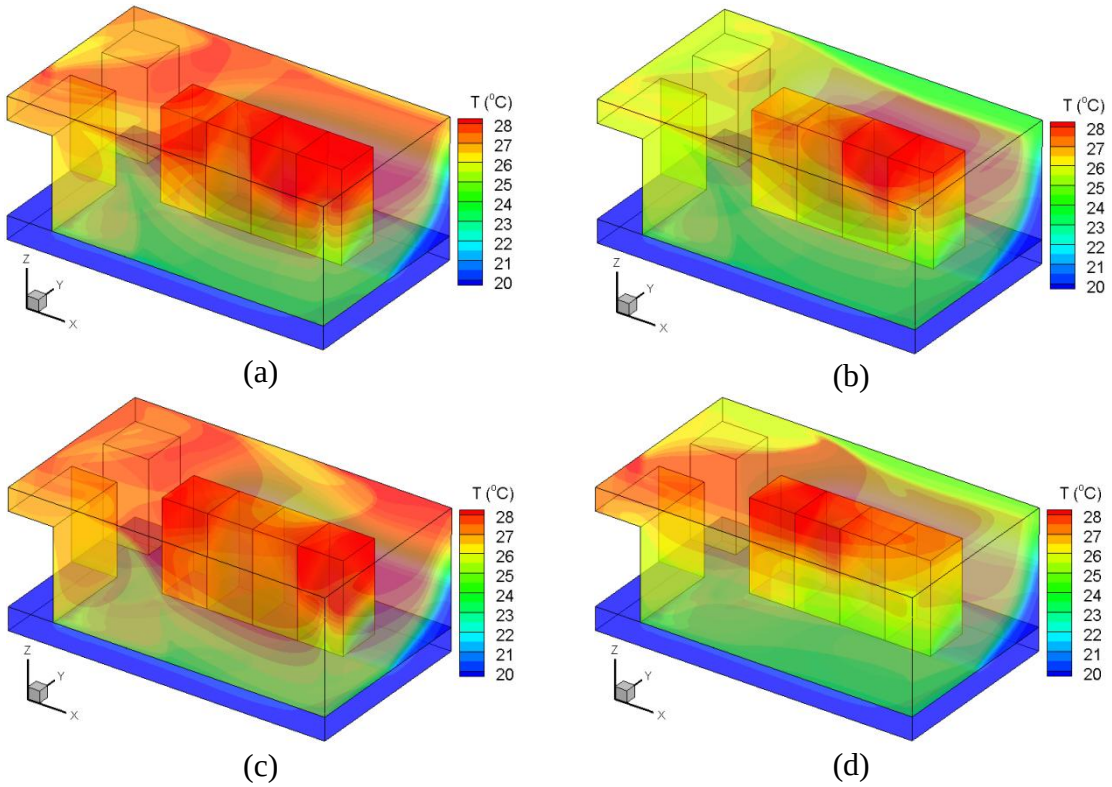

Figure 6.3. Temperature distribution in the data center with 50% untilization.

(a) A_i& C_i racks are operating, flow rate 4650CFM (b) A_i&$C_i$racks are operating, flow rate 5650CFM (c) A_i& D_i racks are operating, flow rate 4650CFM (d) A_i&$B_i$racks are operating, flow rate 4650CFM

As the utilization increases to 50%, a higher flow rate is required to keep the tempeature below a certain value. ASHRAE suggests that for most data centers, the high side ambient temperature limit is 27°C, with an allowable limit of 32°C. Some data centers are designed to work at warmer temperature between 27 to 32°C to save energy on cooling, and some data centers are designed to operate at lower temperature for the better performance of the equipment. In this study, we choose 30°C as the upper limit temperature for the data center room. The CRAC system flow rate will be adjusted to keep the maximum temperature under 30°C. The available flow rates are chosen from Liebert Delux system/3, including 3350, 4650, 5650, 8400, 10200, 15200CFM. As shown in figure 6.3a, when A_i& C_i racks are operating, since the maximum temperature exceeds 30°C, the top of the racks and the CRAC outlet are the high temperature zones. The flow rate is inscrease to 5650CFM to control the tempreature as shown in figure 6.3b. For 50% utilization, the best case that meets the temperature requirement and saves energy is to turn on rack A_i& B_i with CRAC flow rate 4650CFM. The corresponding temperature distribution is shown in figure 6.3d.

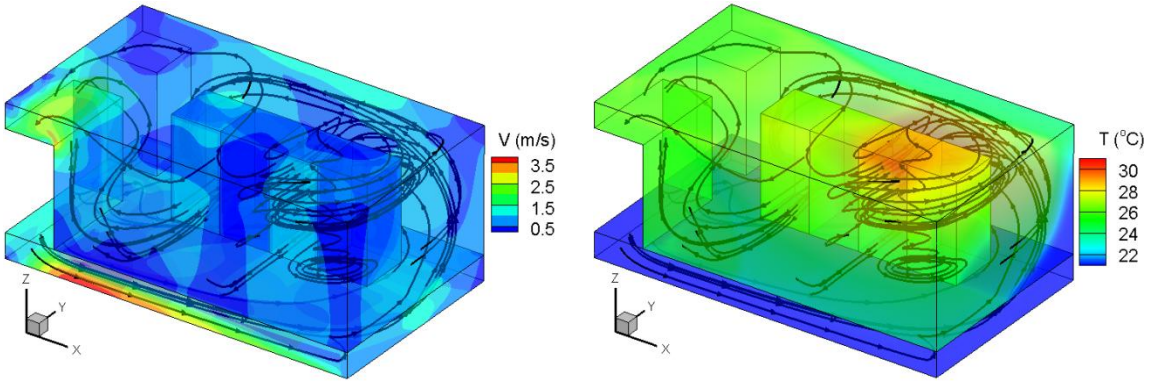

(a) (b)

Figure 6.4. Streamlines for utilization 50%, A_i& C_i are operating.

(a) velocity magnitude (b) temperature distrubtion

Base on our previous observation, it is beneficial for the temperature control and saving energy to have rack A operating. When the utilization is increased, other racks will be turned on accordingly. When the utilization is increased to 50%, the combination of A_i& C_i is the worst senario. This is because all the C_i racks are further from the CRAC outlet, and they are located between B_i and D_i racks, which block the air flow path and lead to more local circulations before the hot air goes to the outside (figure 6.4). B_i racks are also in the middle comparing with C_i rack, but they are closer to the outlet.

When the utilization is increase to 75%, if rack A_i, C_i& D_i are operating, the flow rate has to increase from 10200 to 12000 CFM to maintain the room temperature under 30°C (figure 6.5 (a) and (b)). The combination of A_i, B_i& $D_i$racks is the best case for 75%

utilization (figure 6.5(c)). When the utilization is 100%, the steady state temperature distribution is shown in figure 6.5(d).

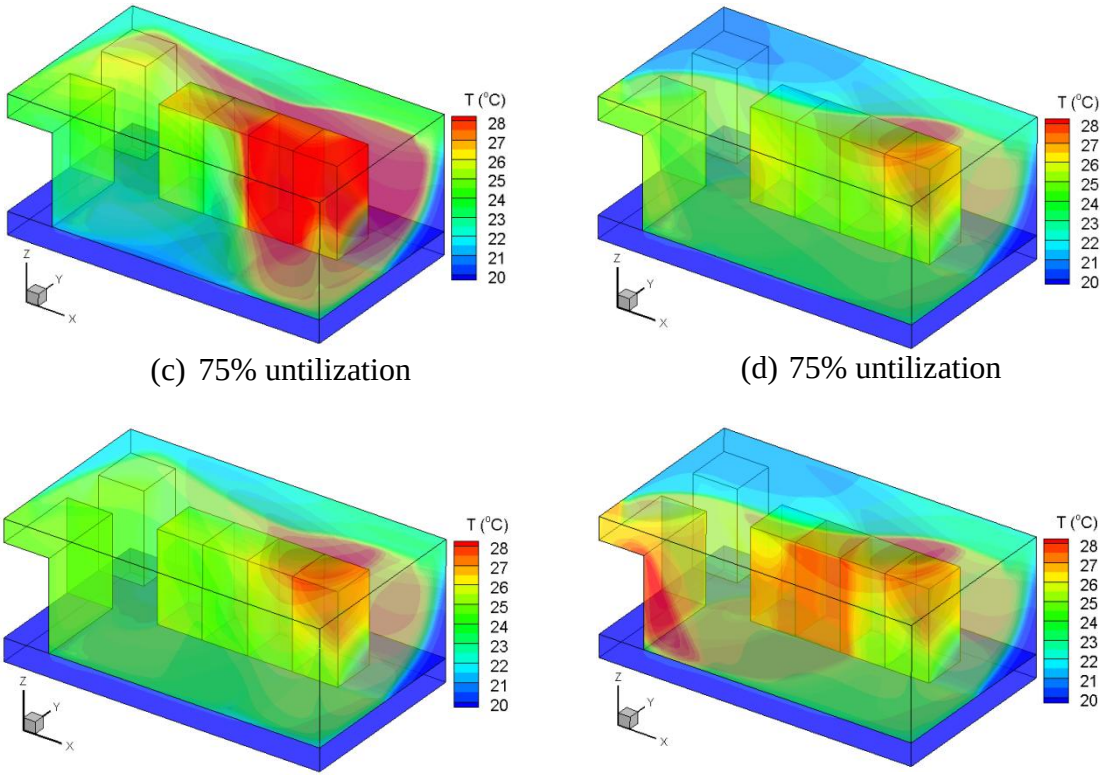

(c) 75% untilization (d) 75% untilization

(e) 75% untilization (f) 100% untilization

Figure 6.5. Temperature distribution with untilization 75% and 100%.

(a) A_i, C_i& D_i racks are operating, flow rate 10200CFM (b) A_i, C_i& $D_i$racks are operating, flow rate 12000CFM (c) A_i, B_i& $D_i$racks are operating, flow rate 10200CFM (d) utilization 100%, all racks are operating, flow rate 12000CFM

The results from CFD/HF simulation can provide guidence for the data center operators to choose the parameters that fit their own situations according to the heat load and the capacity of the CRAC units and chillers.

6.4 Energy consumption

When the data center load is fixed, the total cooling energy consumed by the data center is the sum of the work done by the CRAC and chiller. There are two main settings which affect the cooling system's energy consumption: the CRAC fan speed which determines the air flow rate through the data center, and whether the chiller is turned on. Given an outside temperature and a data center utilization level, the cooling system can be designed to adjust the CRAC fan speed and chiller on/off setting to ensure not only the operation reliability, but also to operate the data center in the most energy-efficient manner.

The work done by CRAC fan is usually a linear function of the air flow rate, which can be calculated as:

$$W_{CRAC} = 2.7V_{in} \tag{6.11}$$

The chiller work is calculated by:

$$W_{chiller} = Q / COP \tag{6.12}$$

The coefficient of performance(COP) of chiller-CRAC loop is a function of CRAC supply temperature. The COP as a function of CRAC inlet temperature is applied in this study:

$$COP = 0.0068T_s^2 + 0.0008T_s + 0.458 \qquad (6.13)$$

The higher the COP is, the less energy the chiller consumes.

If the outside temperature is sufficiently low, then the CRACs take the cold air from the outside and discharge the hot air to the ambient. The chiller will be turned off in this case to save energy. If the outside temperature is too high, then CRACs will need to circulate the hot air through the chiller for cooling and send the cold air into the data center. In the following section, total cooling energy consumption of the same data center at two different locations will be presented and one can easily see that the cooling energy consumption can change significantly throughout the day. Figures 6.6 to 6.8 are examples to show the energy consumption corresponding to different boundary conditions.

Figure 6.6 shows the total energy consumption by the fan and chiller for different loads during winter time in Seattle. Since the outside temperature is low enough, the chiller is turned off. Hence, the energy consumed by chiller is zeros. Similarly, figure 6.7 shows that the energy consumption for fan only during winter time in Princeton. Note that from the equation 6.10 and 6.11, for the same amount of air flow, the chiller will consume

much more energy than the fan. Hence, the energy consumption during winter will be reduced significantly.

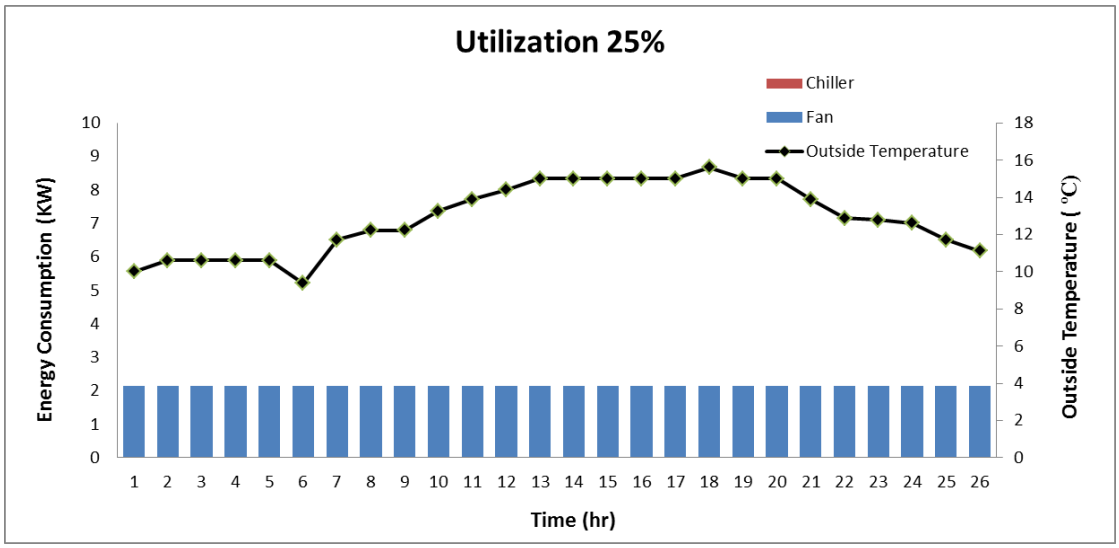

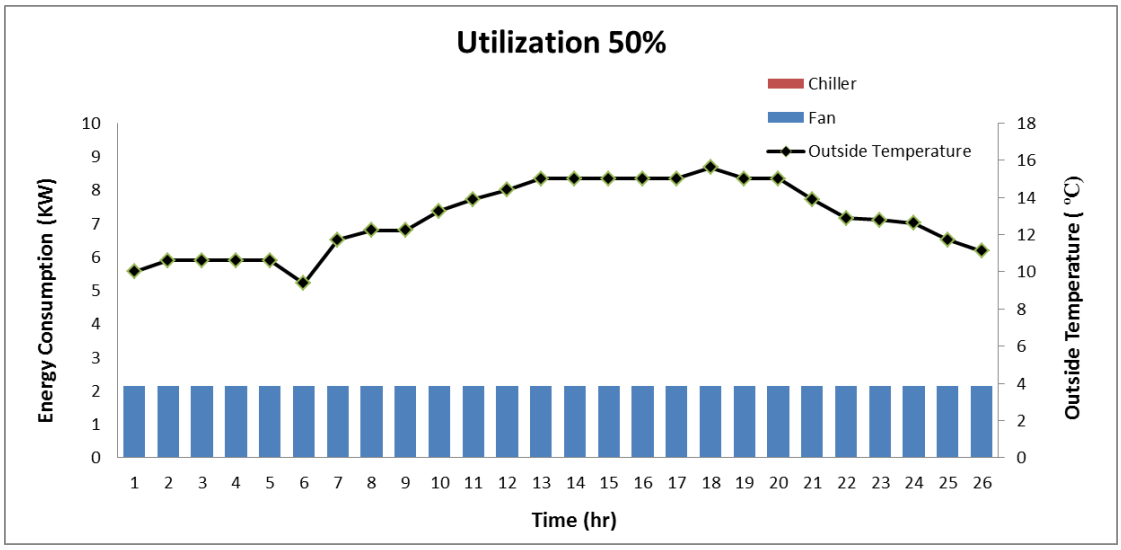

Figure 6.6. The impact of outside temperature on energy consumption (Janurary, Seattle).

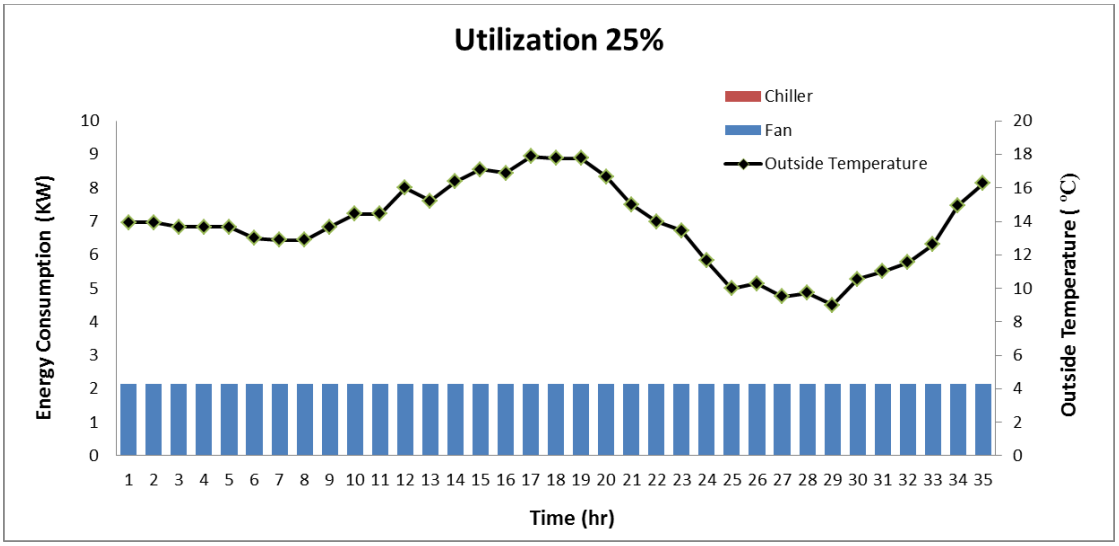
Utilization 25%
Chiller
Fan
Outside Temperature
Energy Consumption (KW)
Outside Temperature (℃)
Time (hr)

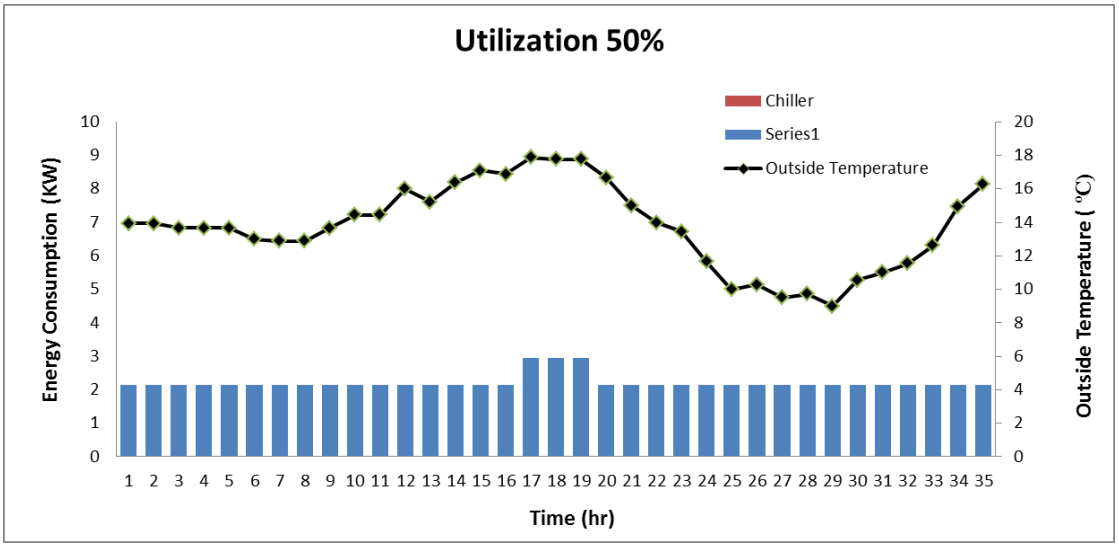
Utilization 50%
Chiller
Series1
Outside Temperature
Energy Consumption (KW)
Outside Temperature (℃)
Time (hr)

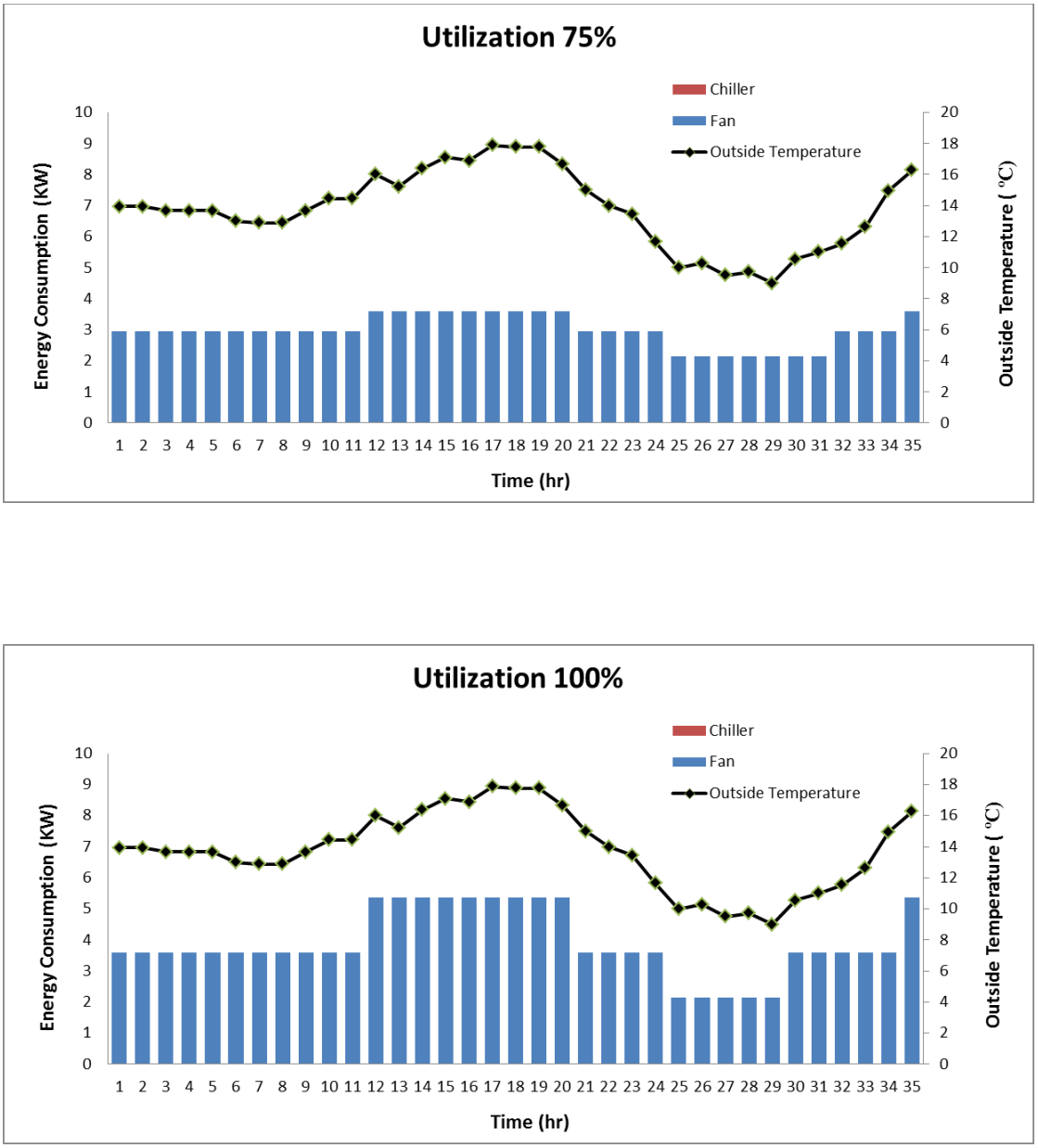

Figure 6.7. The impact of outside temperature on energy consumption (Janurary, Princeton).

When the outside temperature is high, as shown in figure 6.8, simply increasing the flow rate will not be able to maitain the low room temperature. In this case, the chiller needs to be turned on to cool the air temperature down. When the load is 25%, with the lowest

available flow rate, the data center room temperature can be maintained below 30°C if the CRAC supply temperature is at 24°C. During one day period showing in figure 6.8, the chiller needs to be on if the outside temperature is higher than 24°C. The energy consumed by the chiller takes from 30.4% to 72.4% of the total energy consumption.

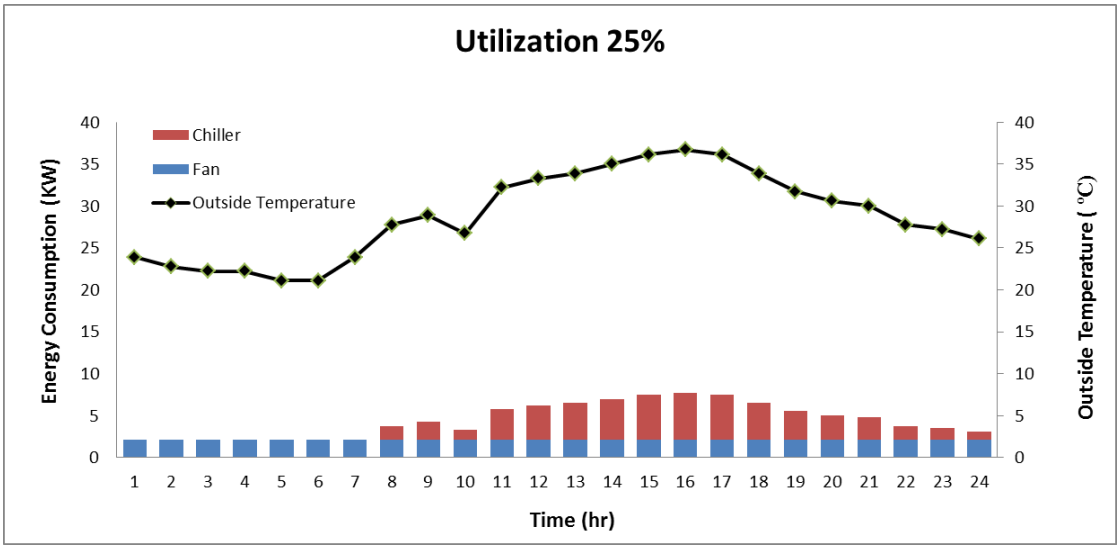

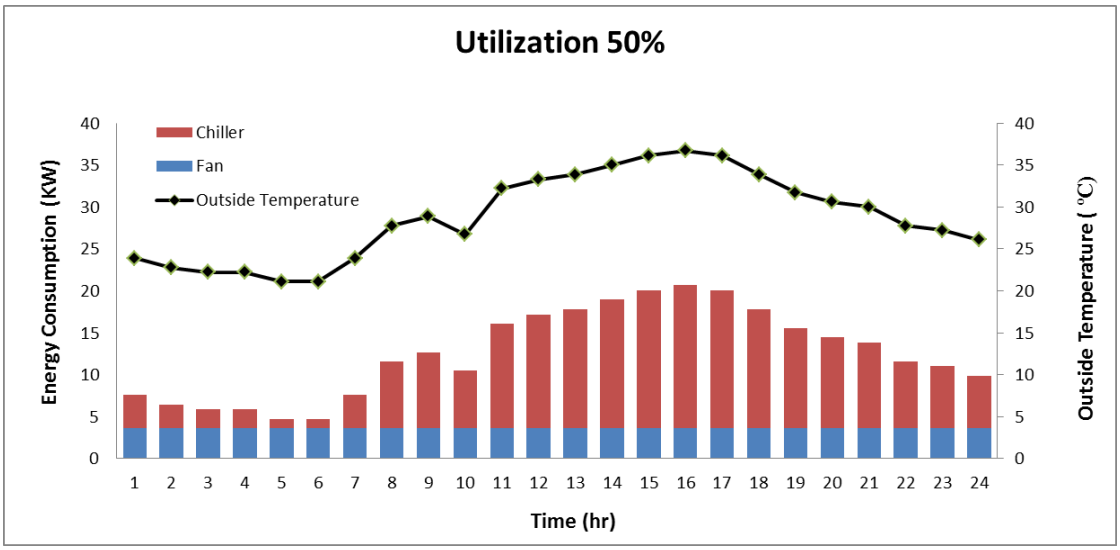

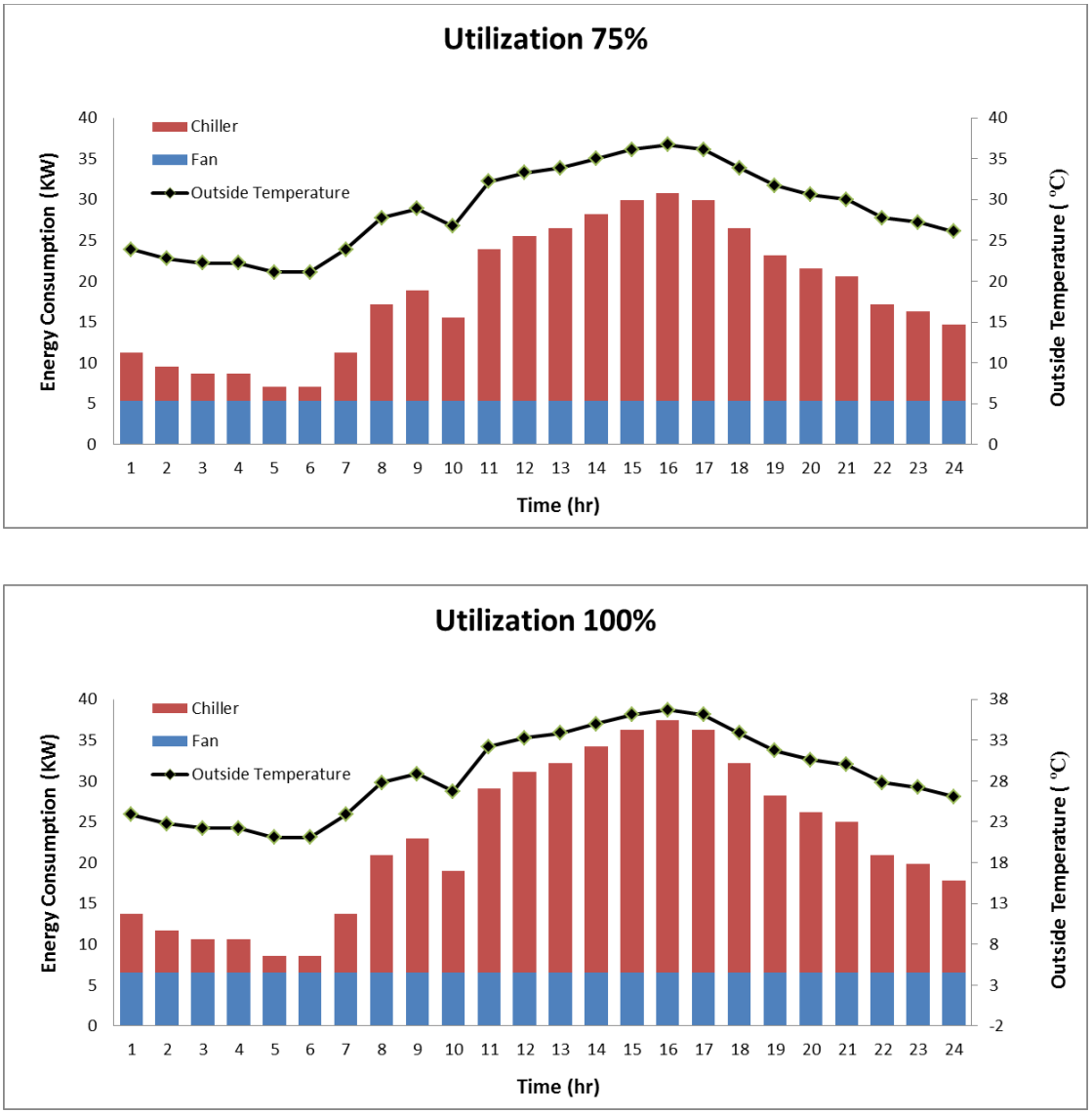

Figure 6.8. The impact of outside temperature on energy consumption (August, Princeton).

As the load is increased to 50%, the required CRAC supply temperature is at 20°C to keep the data center room temperature below 30°C with air flow rate 5650CFM . The chiller needs to be turned on all the time, and the total energy consumption is greatly increased because of the work done by the chiller. For example, if the outside temperature is 30.6°C, the chiller spends 75.2% of the total energy.

The energy consumption apparently does not vary linearly with the load increasement. When the load is increased from 50% to 75%, with the same CRAC supply temperature, the total energy consumption is increased about 49%. As the load keeps increasing to 100% from 75%, the total energy consumption is only increased by 22%. Therefore, if one large data center A has the same capacity as four small same-sized data centers , A is probably consumes less energy than the sumb of the four B data centers. It is more enconomical to build one large data center with high load capacity compared to several smaller ones.

The significant variability of cooling energy consumption versus temperautre and load presents an interesting opportunity for dynamic load distribution to either minimize enrgy consumption and/or cost. If a service is replicated across two data centers, one in Northern California and one in Georgia, during the hottest and coolest periods of the day, it might make sense to direct load to Georgia because the cooling energy consumed is similar but the energy price might be lower in Georgia. On the other hand, when it is hot in Georgia but cool in Northern California, it might be beneficial to direct more load to Northern California because the cooling energy consumption will be much less.

While it makes sense to explore dynamic load distribution because of variable electricity prices as well as cooling(Le. et al 2011), note that transient cooling effects need to be carefully considered, which will be discussed in the next section.

6.5 Transient effects and pre-cooling

ASHRAE (2008) suggests that the recommended environment range of 18 to 27^{o}C with an allowable range from 15 to 32 ^{o}C for most data centers. Most data centers are running with high temperature environment to minimize the cost. If there is a sudden load increase, the cooling systems need a quick response and the CRAC systems have to be able the handle the sudden change. For example, assume the CRAC system was on standby mode, and ambient air was cold enough so it went through a bypass and served directly to the under floor plenum room. When the load is suddenly increased, and a lower supply temperature is required, the CRAC is switched to running mode with the chiller turned on; it will experience a transient ramping period before it can completely cool down the air.

There are two ways to decide the time for the CRAC system to become fully functional numerically. One is to have the entire CRAC system details included in the CFD model and monitor the time needed when the air flow coming out of the CRAC reaches the required temperature. This might be more accurate, but will be very time consuming and requires the detail drawing, dimension as well as materials of the CRAC system. The other way is to use the lumped system analysis. It is relatively easy and simple. Moreover, for the data center cooling system, it is preferable to have this number be conservative.

The time that is needed for the CRAC system and the air flow to reach the supply temperature criterion (20^{o}C in this case) is estimated as follows:

$$\frac{T-T_\infty}{T_i-T_\infty}=\exp(-\frac{t}{RC})=\exp(-\frac{t}{\tau}) \tag{6.14}$$

Where τ is the time constant,

$$\tau=\frac{\rho c_p V}{hA_s} \tag{6.15}$$

Some assumptions and parameters are obtained by using the Liebert Delux system/3 (A frame coil) shown in table 6.1. Based on the numbers obtained from the lumped system analysis, the average response time for the CRAC system is assumed to be 20 minutes in the following study.

Table 6.1. Response time for different flow rate.

Standard Air Volume-CFM	3350	4650	5650	8400	10200	12000	15200
Weight-lbs (kg)-Deluxe System/3	1455 (660)	1675 (760)	1690 (767)	2110 (957)	2280 (1034)	2345 (1064)	2500 (1134)
Face Area-Sq. ft. (m2)	14.2 (1.32)	14.2 (1.32)	14.2 (1.32)	22.2 (2.06)	22.2 (2.06)	22.2 (2.06)	29.38 (2.73)
Rows of Coil	3	3	4	4	4	4	4
Time Constant (min)	14	17	13	10	11	11	9
Response time (to reach 80% of the required temp) (min)	24	27	21	16	18	18	15

Different cooling responses (scenarios) for sudden load change occurring at t=0s were listed in table 6.2. Each scenario is a sequence of different actions taken, which include increasing the air flow, turning on the chiller or the combination of the two.

The initial conditions for all the scenarios are the same: the utilization was increased from 25% to 75% instantaneously. The chiller was off before the change and the flow rate was 3350 CFM. Since very little heat is lost from the system, if the cooling system settings remain the same, the temperature will ramp up to 42ºC (the maximum temperature will exceed 30 ºC in less than 5 minutes) with nearly all of the heat contributing to raise the temperature as shown in figure 6.10 scenario 1. When the cooling level is increased, the temperature rise will slowly decrease until a steady state temperature is again reached. For scenario 2, the flow rate remained the same as the chiller was turned on right away at t=0s, however, it will need about 20 minutes to respond. The initial response of scenario 2 is the same as scenario 1, except that the steady state temperature is lower as expected.

Table 6.2. Potential Responses of Cooling System to Sudden Large Load Increase.

Scenario	1	2		3	4		5	
Time(min)		t<20	t>20		t<20	t>20	t<20	t>20
Flow Rate (CFM)	3350	3350		10200	3350	10200	10200	
Chiller	OFF	ON		OFF	ON		ON	
Flow go through Chiller or not	No	No	Yes	No	No	Yes	No	Yes

Table 6.2(continued)

Scenario	6		
Time (min)	t<5	5<T<10	t>10
Flow Rate (CFM)	3350	5650	10200
Chiller	OFF		
Flow go through Chiller or not	No		

Table 6.2(continued)

Scenario	7			
Time (min)	t<5	5<T<10	10<T<15	t>15
Flow Rate (CFM)	3350	5650	10200	15200
Chiller	OFF			
Flow go through Chiller or not	No			

Table 6.2(continued)

Scenario	8			
Time(min)	t<5	5<T<10	10<T<15	t>15
Flow Rate (CFM)	3350	5650	10200	10200
Chiller	OFF			ON
Flow go through Chiller or not	No			Yes

Table 6.2(continued)

Scenario	9				
Time (min)	t<5	5<T<10	10<T<15	15<T<35	t>35
Flow Rate (CFM)	3350	5650	10200	10200	10200
Chiller	OFF			ON	ON
Flow go through Chiller or not	No				Yes

Assuming that a maximum allowable operating temperature is 30ºC and the outside temperature is 23 ºC, the only responses that eventually lead to a stable temperature under 30ºC are those that use the chiller. For example, scenario 3, which aggressively increases the flow rate, stabilized the temperature at above 30ºC. Scenario 7, which ultimately uses a larger flow rate than scenario 3, but increases the flow rate more conservatively is not beneficial, allowing the temperature to rise over 32ºC before settling to a stable temperature slightly above 30ºC.

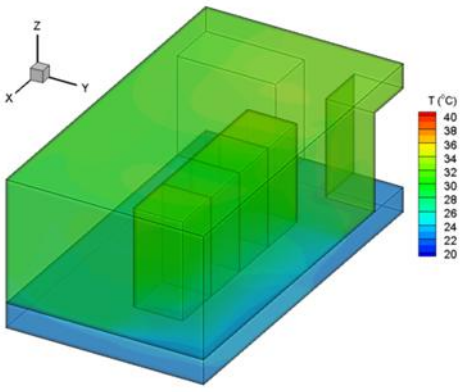

t=8 min

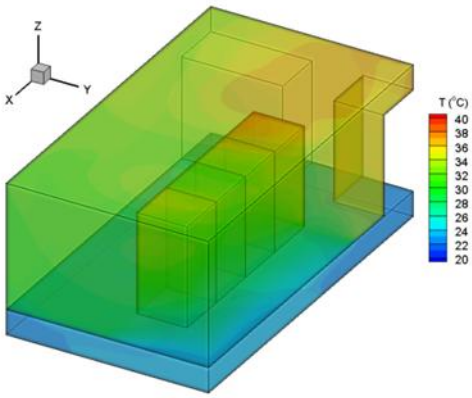

t=16 min

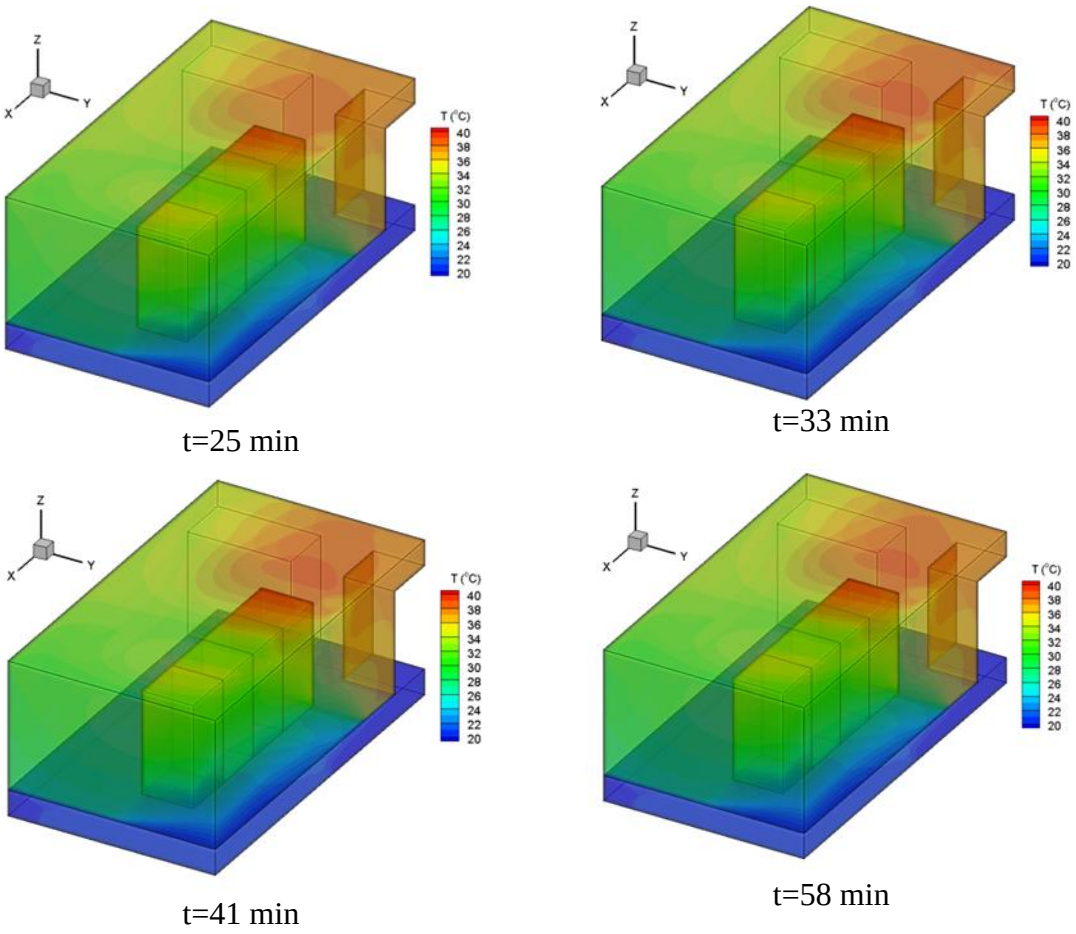

Figure 6.9. Transient temperature distribution in the data center for scenario 2.

Furthermore, note that for scenario 4, 5 and 8, even though temperatures are either high above the allowable temperature (scenario 4), or slightly higher than the allowable temperature (scenario 5 and 8) as the load changed initially, the steady state temperature of all the three scenarios are under 30ºC. Apparently, it is not sufficient to turn on the chiller when the load change is observed. This will put the equipment under high risk and may cause a break down because of the high temperature.

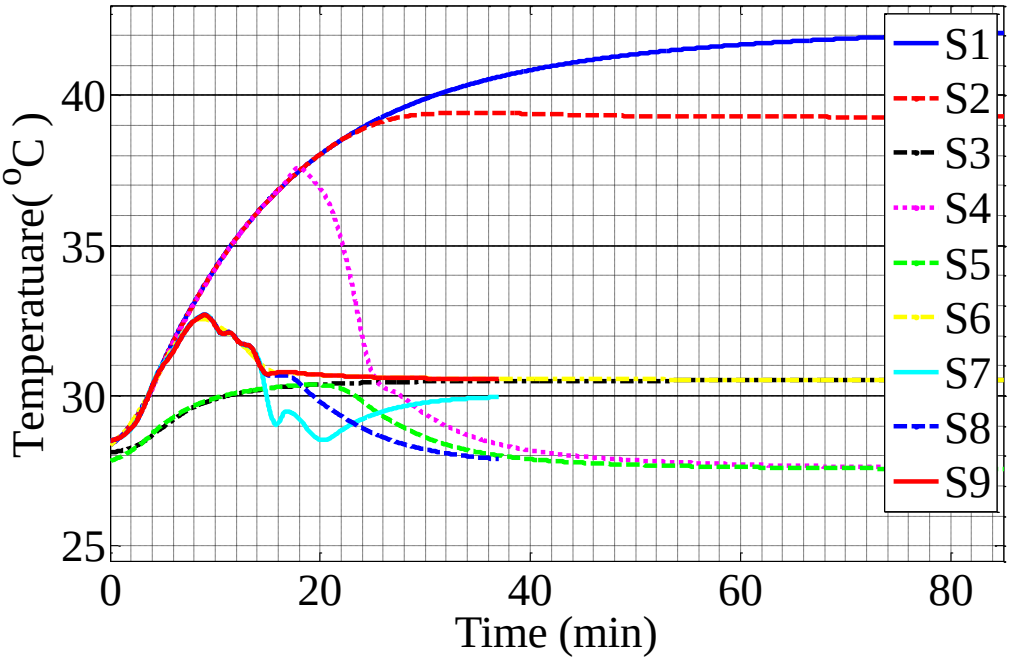

Figure 6.10. Temperature vs. time for different scenarios.

To prevent the overheating caused by the response time required by CRAC systems, pre-cooling is proposed (Le. et al 2011). This part of the study is a collaboration with researchers (Kien Le, Thu D. Nguyen, and Ricardo Bianchini) from the Department of Computer Science here at Rutgers. If the arriving jobs exceed the capacity of current cooling system settings and may cause overheating problem, they will be delayed or sent to other data centers. The front-end can ask the data center to pre-cool (by turning on the chiller early) in preparation for receiving load.

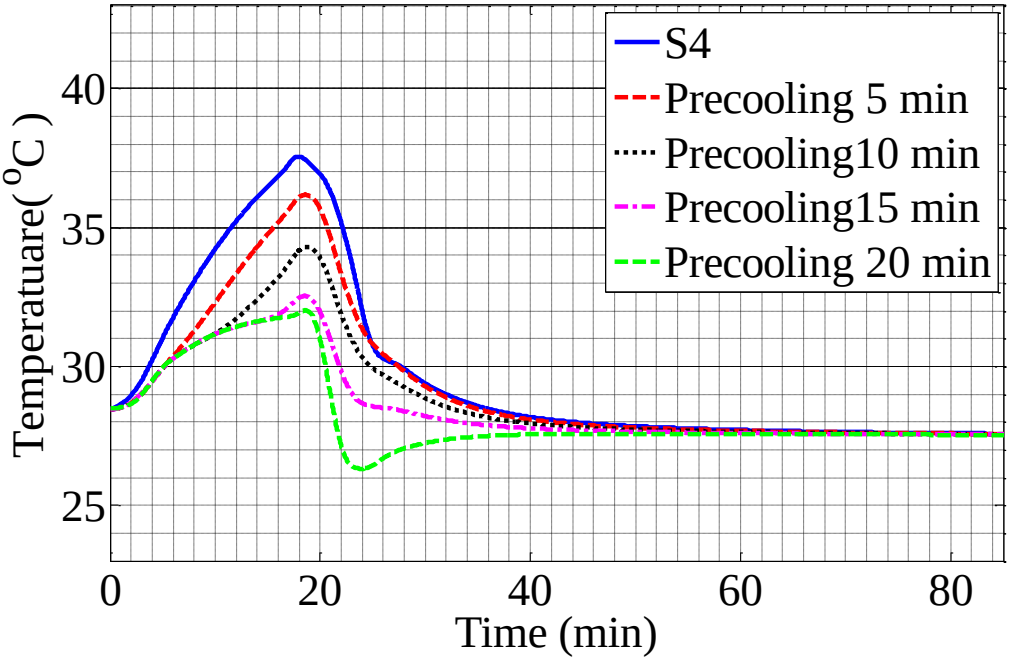

(a) Scenario 4 with pre-cooling by 5 to 20 minutes

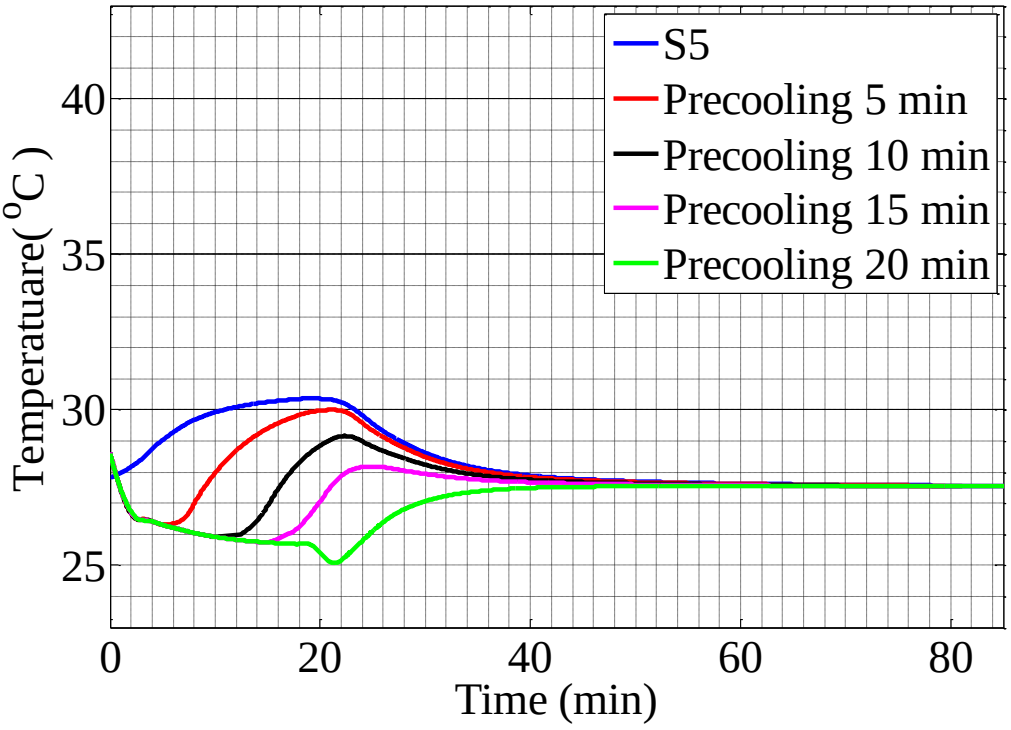

(b) Scenario 5 with pre-cooling by 5 to 20 minutes

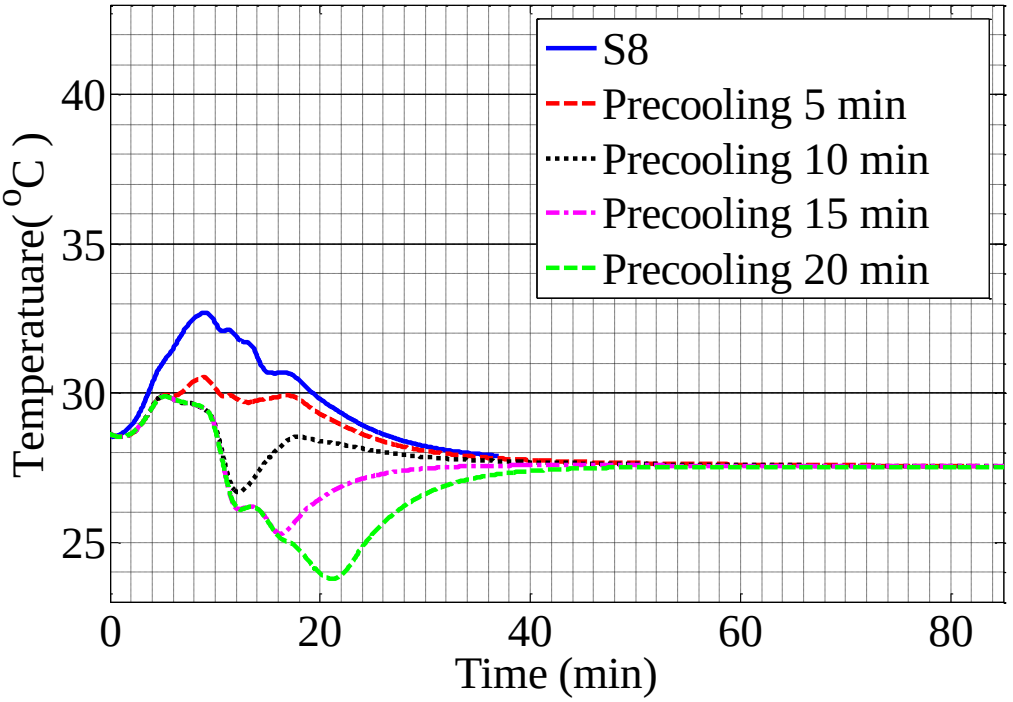

(c) Scenario 8 with pre-cooling by 5 to 20 minutes

Figure 6.11. Temperature in the data center vs. different cooling responses.

The pre-cooling time depends on the cooling scenario setting. As shown in figure 6.12(a), for scenario 4, even with 20 minutes pre-cooling, the temperature will still rise to 32ºC. Scenario 5 (figure 6.11b), which immediately increases the flow rate as the chiller is turned on, only needs to pre-cool for 5 minutes before the load change. For scenario 8(figure 6.11c), if you increase the flow rate gradually and meanwhile pre-cool for 10 minutes or longer, the temperature is controlled under 30ºC. It is unnecessary to pre-cool the data center for 20 minutes for scenario 8.

Chapter 7 Conclusion

This chapter reviews the major conclusions of the dissertation. Electronic cooling problems were investigated at both large scale and micro scale. The main results and contributions of current study are listed below:

i. Comprehensive experimental and numerical study of microchannel heat sink

An experimental and numerical combined approach was applied to study the thermal and fluid performance of microchannel heat sinks. Silicon microchannel heat sinks was designed and fabricated. An experimental test facility was built and the data measurement instruments were calibrated with a temperature measurement uncertainty within ±0.5℃. Multi-microchannel heat sinks of different geometries (straight, bended and branched channels) were studied with varying flow rates and heat fluxes. The components that contribute to the thermal resistance were identified and pressure drop was studied including the inlet and outlet loses, developing flow losses, and frictional flow losses.

Numerical models were built for all heat sink devices experimentally tested and good agreements between numerical and experimental results were discovered with disparity within 4%. Vortices, secondary flow with mixing, and axial temperature gradient enlargement were discovered as the flow changes direction in the bended and branched channels through numerical simulation. Heat transfer is proven to be enhanced with

bended and branched channels, but with the trade-off of a higher pressure loss that requires extra pumping power.

ii. Transient study

The transient heat transfer behavior of the multi-microchannel heat sinks with different configurations (Straight channel, U-shaped channel and serpentine channel) was studied. The experimental results suggested that the U-shaped channel heat sinks response faster and remove heat more quickly compared with the straight channel and serpentine channel heat sinks. The serpentine channel required more time to reach steady state compared with straight channel. As the flow rate increased, the difference between the two configurations became smaller. Varying heat flux had less impact on the response time than varying flow rate. The response time results obtained from this study can be used as one of the parameters to evaluate the thermal performance of heat sinks.

iii. Design and optimization

The optimization problems focused on two different designs: the straight and U-shaped multi-microchannel heat sinks. The multi-objective optimization problems were formulated and studied with and without physical constraints. For each example given in this study, 125 sampling points were investigated. Various responses were generated through parametric modeling of these data points to study the influence of flow rates and geometrical variables to the thermal performances. The Pareto frontiers were found and presented to demonstrate the trade-offs between the multi-objective functions. In the

constrained formulations, the feasible design spaces were narrowed and more conservative optimal solutions were found. The developed strategies are useful not only to understand the fundamental heat transfer and fluid flow characteristics in the multi-microchannel designs, but also to provide quantitative inputs for the processes of design and optimization.

iv. Data center cooling system

A detailed model of raised floor data center cooling system was developed. The cooling power demand as a function of the data center load and outside temperature was obtained with the maximum allowable temperature constraint. Since the energy consumption varies significantly with outside temperature and the data center loads change corresponding to dynamic load migration. The transient cooling effect corresponding to an abrupt, large change in data center loads was investigated. The results suggested that the pre-cooling before load increase is necessary in order to prevent overheating. Different pre-cooling scenarios with different cooling demands were analyzed.

Future work

1. The enhancement in heat transfer due to the combination of different geometries can be investigated. Combine different simple elements, such as L-bend, 90 bends, U-bends Y-shaped channels and straight channels together to form a new heat sink design.

2. Study the enhancement of heat transfer with nano-particles with high conductivity mixed in liquid. Understand the underlying physics of the effectiveness of the presence of nano-particles.

3. Capture the local hot spot in the microchannel heat sink with fluorescence microscope, and improve the thermal uniformity.

APPENDIX

Photo masks with different channel configuration patterns

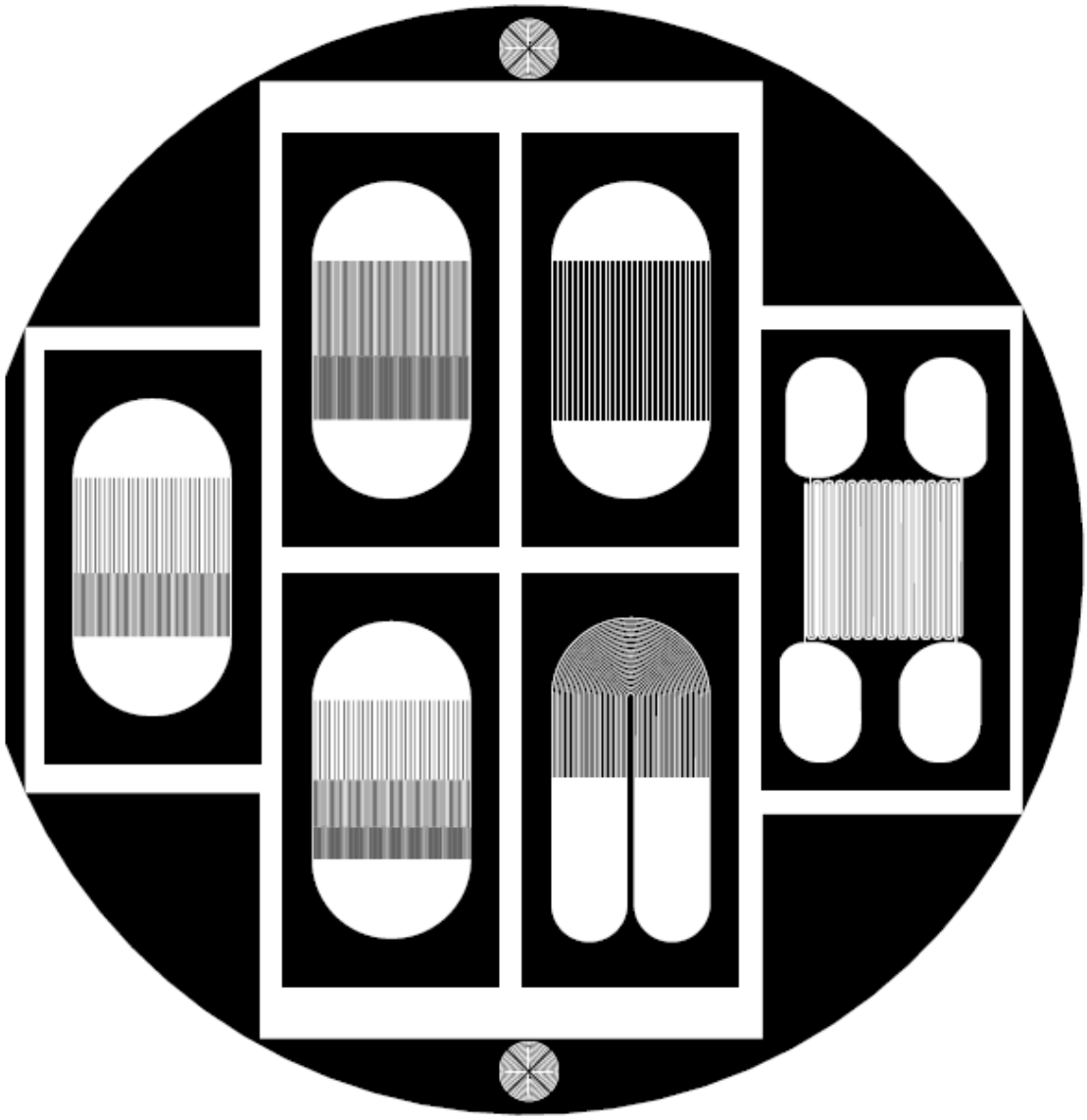

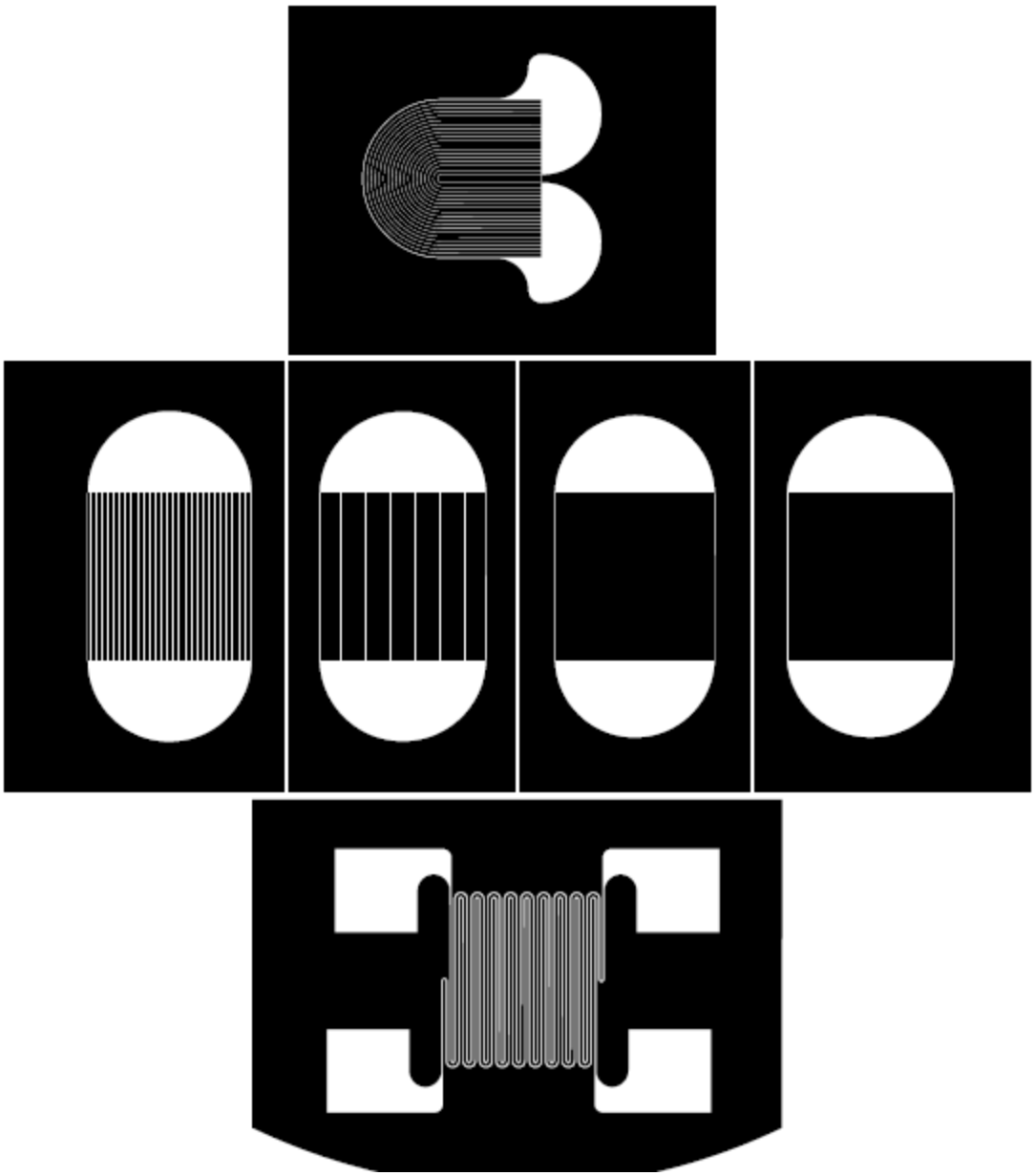

BIBLIOGRAPHY

ASHRAE, 2008, "Environmental Guidelines for Datacom Equipment," American Society of Heating, Refrigeration, and Air-Conditioning Engineers

L. Deb, 2001, "Multi-Objective Optimization Using Evolutionary Algorithms of Wiley-Interscience Series in Systems and Optimization", John Wiley & Sons, LTD, Chichester, England, pp. 50-57.

D. Abts, M. R. Marty, P. M. Wells, P. Klausler, and H. Liu, 2010, "Energy proportional datacenter networks", In ISCA 2010, pp338-347

V.K. Dwivedi, R. Gopal, S. Ahmad, 2000, "Fabrication of very smooth walls and bottoms of silicon microchannels for heat dissipation of semiconductor devices" Microelectronic Journal, Vol 31, pp405-410

A.G. Fedorov and R. Viskanta, 2000, "Three-dimensional Conjugate Heat Transfer in the Microchannel heat sink for electronic packaging", International Journal of Heat and Mass Transfer, Vol. 43, pp. 399-415.

A. J. Ghajar and L. M. Tam, 1995, "Experimental Thermal and Fluid Science", 10, pp 287-297

Guidelines for Evaluating and Expressing The Uncertainty of NIST Measurement Results, 1994, NIST Technical Note 1297.

S. Greenberg, E. Mills and B. Tschudi, etc. 2006, "Best Practices for Data Centers: Lessons Learned from Benchmarking 22 Data Centers", ACEEE Summer Study on Energy Efficiency in Buildings.

T.M. Harms, M.J. Kazmierczak, and F.M. Gerner, 1999, "Developing Convective Heat Transfer in Deep Rectangular Microchannels", International Journal of Heat and Fluid Flow, 210, 149-157.

A. Husain, K.Y. Kim, 2007, “Design optimization of microchannel for micro electronic cooling”, The Fifth International Conference on Nanochannels, Microchannels and Minichannels,. ICNMM2007-30053.

T. Harirchian, S.V. Garimella, 2008, “Microchannel size effects on local flow boiling heat transfer to a dielectric fluid”, International Journal of Heat and Mass Transfer, Vol. 51 pp. 3724-3735.

I.E. Idelchik, 1986, Handbook of Hydraulic Resistance, 2nd ed., Harper & Row, New York

International Technology Roadmap for Semiconductors (2008 update)

Y. Jaluria, 1998 , “Design and Optimization of Thermal System”.

R. C. Joy and E. S. Schlig, 1970, “Thermal Properties of Very Fast Transistors,” IEEE Transactions on Electron Devices, Vol. ED-17, No.8, pp. 586-594

S. G. Kandlikar, 2003, “Microchannel and Minichannel-History, Terminology, Classification and Current Research Needs” Paper No. ICMM 2003-1000 First International Conference on Microchannels and Minichannels 2003, April 24-25, Rochester. NY

K. C., Karki, A. Radmehr,and S. V. Patankar, 2003, “Use of Computational Fluid Dynamics for Calculating Flow Rates Through Perforated Tiles in Raised-Floor Data Centers,” International Journal of Heating, Ventilation, Air-Conditioning, and Refrigeration Research, 9(2):153-166.

P. K. Kundu, and I. M Cohen, 2002: Fluid Mechanics. 2nd ed. Elsevier Academic.

K. Le, J. Zhang, J. Meng, R. Bianchini, T. D. Nguyen, Y. Jaluria, 2011, “Reducing Electricity Cost Through Virtual Machine Placement in High Performance Computing Clouds”, Proceedings of Super Computing (SC11)

J. Li, G. P. Peterson, P. Cheng, 2004, “Three dimensional analysis of heat transfer in a micro-heat sink with single phase flow”. International Journal of Heat and Mass Transfer, 47 4215-4231.

Z. Li, X. Huai, Y. Tao and H. Chen, 2007, “Effects of thermal property variations on the liquid flow and heat transfer in microchannel heat sinks”, Applied. Thermal Engineering. 27 (2007), pp. 2803–2814.

P. T. Lin, H. C. Gea, and Y. Jaluria, 2010, "Systematic Strategy for Modeling and Optimization of Thermal Systems with Design Uncertainties". Frontiers in Heat and Mass Transfer, 1, Paper number 013003.

G.M. Mala, D. Li, C. Werner, H.J. Jacobasch, and Y.B Ning, 1997, “Flow Characteristics of Water through Microchannels Between Two Parallel Plates with Electrokinetic Effects International Journal of Heat and Fluid Flow, 18, 489-496.

G. Maranzan, I. Perry, and D. Maillet, 2004, “Mini-and Micro-channels: Influence of axial conduction in the walls" International Journal of Heat and Mass Transfer, Vol.47, pp. 3993-4004.

NREL, 2010, “Best Practices Guide for Energy-Efficient Data Center Design,” National Renewable Energy Laboratory (NREL), U.S. Department of Energy

I. Papautsky, J. Brazzle, T. Ammel, and A.B. Frazier, 1999, “Laminar Fluid Behavior in Microchannels Using Micropolar Fluid Theory”, Sensors and Actuators, 73, 101-108.

Parker Hannifin Corp., "Data Sheet of Miniature Diaphragm Pumps: LTC Series 650mLPM Free Flow Mini Pumps (liquids)". See also URL http://www.parker.com/ precisionfluidics.

M. Patterson, “The effect of Data Center Temperature on Energy Efficiency”, Thermal and Thermomechanical Phenomena in Electronic Systems, 2008, pp1167-1174.

K. E. Petersen, 1982, “Silicon as a mechanical Material”, Proceedings of the IEEE, Vol. 70. No.5 pp. 420-457

T. Sato, 1967, “Spectral Emissivity of Silicon”, Jpn. J. Appl. Phys. 6. Pp.339-347

R. Schmidt, 2004 “Raised-Floor Data Center: Perforated Tile Flow Rates For various Tile Layouts”, 2004, Inter Society Conference on Thermal Phenomena “.

R. K. Shah, A. L. London, 1978, ‘Laminor Flow Froced Convection in Ducts’, Academic Press, INC

P. Sharath, C. Rao, M.M. Rahman, and H.M Soliman, 2006, “Numerical Simulation of Steady-State Conjugate Heat Transfer in a Circular Microtube inside a Rectangular Substrate”, Numerical Heat Transfer, Part A, Vol.49, pp. 635-654, 2006.

M. E. Steinke, S. G. Kandikar et al, 2006, “Development of An experimental facility for investigating single phase liquid flow in microchannels”, Heat Transfer Engineering, 27 (4):pp. 41-52.

W. Tschudi, P. Sreedharan, T. Xu, D. Coup, P. Roggensack, 2003, “Data Centers and Energy Use” paper No.162 American Council for an Energy-Efficient Economy report.

C.P. Tso, and S.P. Mahulikar, , 1998, “The Use of the Brinkman Number for Single Phase Forced Convective Heat Transfer in Microchannels”, International Journal of Heat and Mass Transfer, 41, 12, 1759-1769.

D. B. Tuckerman, and R.F.W. Pease, 1981, “High Performance Heat Sinking for VLSI, IEEE Electronic Device” Lett. EDL_2 126-129

D.B. Tuckerman, 1984, “Heat-Transfer Microstructures for Integrated Circuits, ” Ph. D. Thesis, Stanford University, Stanford, CA

Y. Wang, P. Jackson, T. Phaneuf, 2009, “Flow structure in a U-shaped Channel”, Journal of Thermophysics and Heat Transfer, Vol.23 no.1 (106-119).

X. J. Wei, Y. K. Joshi, 2004, “Stacked microchannel heat sinks for liquid cooling of microelectronic components”, Journal of Electronic Packaging 126, 60

C. L. Wiginton, C. Dalton, “Incompressible laminar flow in the entrance region of a rectangular duct”. Journal of Applied Mechanics. 37, 854-359

R. Xiong, J. Chung, 2007, “Flow characteristics of water in straight and serpentine micro-channels with miter bends”, Experimental Thermal and Fluid Science 31, 805-812.

L. Zhang, J. Koo, L. Jiang, M. Asheghi, K, Goodson, J. Santiago, T. Kenny, 2002, “Measurements and Modeling of Two-phase Flow in Microchannels With Nearly Constant Heat Flux Boundary Conditions”

H.Y. Zhang, D. Pinjala, T.N. Wong, K.C. Toh and Y.K. Joshi, 2005, “Single-phase liquid cooled microchannel heat sink for electronic packages”, Applied. Thermal Engineering. 25 pp. 1472–1487.

X. Zhang, J. VanGilder, M, Iyengar, R. Schmidt, “Effect of Rack Modeling Detail of the Numerical Results of a Data Center Test Cell”. Thermal and Thermomechanical Phenomena in Electronic Systems, 2008. THERM 200831, pp1183-1190